Real gas effects in ORC turbines

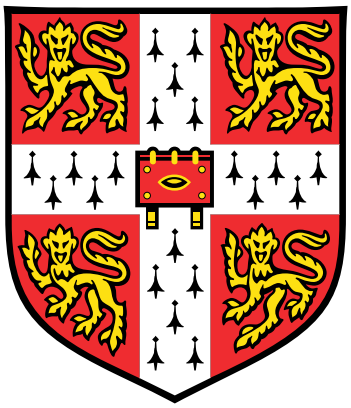

David Baumgärtner

Supervisor: Dr. A. P.S. Wheeler

Whittle Laboratory
Department of Engineering
University of Cambridge

This dissertation is submitted for the degree of of Doctor of Philosophy

Gonville and Caius College August 2020

Declaration

This thesis is the result of my own work and includes nothing which is the outcome of work done in collaboration except as declared in the Preface and specified in the text. It is not substantially the same as any that I have submitted, or, is being concurrently submitted for a degree or diploma or other qualification at the University of Cambridge or any other University or similar institution except as declared in the Preface and specified in the text. I further state that no substantial part of my thesis has already been submitted, or, is being concurrently submitted for any such degree, diploma or other qualification at the University of Cambridge or any other University or similar institution except as declared in the Preface and specified in the text. It does not exceed the prescribed word limit for the relevant Degree Committee'

David Baumgärtner
August 2020

Real gas effects in ORC turbines

David Baumgärtner

Abstract

This thesis aims to study the effects of varying gas properties on turbine performance. Most prominently ORC turbines are operating with a multitude of different working fluids that have very strong variations in gas properties. Moreover, this also applies to conventional steam turbines or first stage HP turbines with very high temperatures, where the gas properties can divert significantly from air at ambient conditions. The isentropic exponent and compressibility factor are commonly used to describe a fluid's gas dynamic behaviour and its diversion form ideal gas conditions.

Though, the effects of these parameters on turbine performance are not well known. This thesis discusses a series of experimental and computational studies to determine the impact of the isentropic exponent and compressibility factor on the flow field within a turbine vane and radial stage. A series of experiments are performed on a newly modified transient wind tunnel, that allows testing of vanes with various working fluids at a range of operating conditions. Detailed wall static pressure measurements of the cascade were obtained, as well as wake measurements in the supersonic flow downstream of the vane. For this thesis, experiments were conducted with argon, air, CO_2 and R134a, which give a range of isentropic exponent from 1.67 to 1.08 and a range in compressibility factor from 0.88 to 1.0.

The experimental results are used to validate the computational approach, that has revealed that over the given range of isentropic exponents, the loss can vary between 20% and 35%, depending on vane exit Mach number. These difference in aerodynamic loss are driven by a change in the mixing loss at the trailing edge loss and a shift in shock loss within the passage. These effects are a strong function of vane exit Mach number whereby they only occur at supersonic speeds and sensitivity is increasing with rising Mach numbers. Moreover, computational analysis on the effect of the compressibility factor has shown that low values of Z have a favourable effect on turbine performance through reduced shock loss and boundary layer loss. Within the given range of compressibility factor, a 10% change in Z results in a 3% change in total loss. Thus, the sensitivity of loss to the isentropic exponent as much higher than for the compressibility factor.

Acknowledgements

First of all, I would like to thank my parents for supporting me throughout my entire educational path, that has led me to conduct this research and submitting this thesis.

Furthermore, I would like to thank my supervisor Andy Wheeler who presented me with the opportunity to do this PhD at the Whittle Laboratory on this very interesting matter. We had some great discussions on the topic, and he always offered good guidance throughout the entire PhD.

Also, I would like to thank John Otter and Carlos Ventura for supporting me with the experiments and many helpful discussions.

Lastly, I would like to thank Luke Arnold, Josh Firman and James Taylor, who were of great help in manufacturing the new test section and probe.

Table of contents

List of figures **xiii**

List of tables **xix**

Nomenclature **xxi**

1 Introduction **1**

1.1 Turbine principles 2

1.2 Gas properties 3

1.2.1 Isentropic exponent 4

1.2.2 Fundamental derivative 6

1.2.3 Compressibility factor 7

1.2.4 Dependence of k and Z on thermodynamic state 8

1.3 Gas dynamics 9

1.4 Real gas performance 12

1.5 Research questions 18

2 Experimental method **21**

2.1 Transient wind tunnel - Ludwieg tube 21

2.2 Test section 23

2.3 Data acquisition 26

2.4 Total pressure measurements in supersonic flow 27

2.5 Increased repeatability via choked afterbody 30

2.6 Run conditions 33

2.7 Summary 34

3 Computational method **35**

3.1 Vane design 35

3.2 Stage design . . . 37
3.3 Solver settings . . . 38
3.4 Meshing . . . 39
3.5 Real gas model . . . 40

4 Experimental validation of computational methods 43
4.1 Wall static pressure . . . 43
4.2 Wake measurements . . . 47
4.3 Summary . . . 50

5 The effect of isentropic exponent k on vane performance 53
5.1 Loss analysis . . . 54
5.1.1 Loss breakdown . . . 56
5.2 The effect of isentropic exponent k on trailing edge loss . . . 58
5.3 A correlation for the effect of isentropic exponent on loss . . . 64
5.4 Vane loss for gas mixture . . . 66
5.5 Summary . . . 67

6 Effect of compressibility factor Z on loss 69
6.1 Matching of gas dynamics for non-polytropic fluids . . . 69
6.2 Validation of matched gas dynamics . . . 74
6.3 Loss analysis of CFD simulations . . . 76
6.4 The effect of real gas behaviour on shock loss . . . 77
6.5 Impact of compressibility factor Z on boundary layer . . . 82
6.6 The effect of real gas behaviour on mixing loss . . . 85
6.7 Summary . . . 89

7 Real gas effects in high-pressure turbine stage 91
7.1 Design of radial turbine with real fluids . . . 91
7.1.1 Stage design parameters . . . 93
7.1.2 Endwall design . . . 94
7.2 Effect of isentropic exponent k on stage loss . . . 96
7.3 Effect of compressibility factor Z on stage loss . . . 106
7.4 Summary . . . 109

8 Conclusions 111
8.1 Future work . . . 113

References 117

Appendix A List of REFPROP fluids 121

List of figures

1.1 Expansion through a turbine on enthalpy-entropy plot 2
1.2 Different categories of gasses 3
1.3 Pressure-density plots along isentropes at a range of stagnation pressures for Pentane (left) and R245fa (right), $T_o/T_c = 1.05$ (Wheeler and Ong (2013)) . 5
1.4 Generalized compressibility chart for various gases (Moran and Shapiro (2014)) 7
1.5 Contours of k and Z for pentane on T-s diagram. Iso-bars are drawn at p_c and 1 atm. 8
1.6 1D effect of k on inviscid gas dynamics 9
1.7 Variation of Prandtl-Meyer function with Mach number for several values of k (Wheeler and Ong (2013)) 11
1.8 2D effect of k on inviscid gas dynamics 11
1.9 LES predicted Mach number contours of air, CO_2 and SF_6 (Galiana et al. (2016)) 12
1.10 Efficiency prediction for an axial turbine stage at optimum specific speed (Macchi and Perdichizzi (1981)) 14
1.11 Efficiency prediction for a radial turbine at optimum specific speed (Perdichizzi and Lozza (1987)) 14
1.12 Correlation obtained between Z and the ratio between real enthalpy change and enthalpy change evaluated from the temperature drop (Manente and Lazzaretto (2012)) 16
1.13 Breakdown of predicted loss contributions to efficiency (Wheeler and Ong (2014)) 17

2.1 Schematic view of the Ludwieg tube 22
2.2 Typical pressure traces showing run times for air and R134a 22
2.3 Baseline vane design 23
2.4 Picture of cascade geometry mounted between elliptic hub and afterbody . . 24

2.5 Cascade geometry showing modification of vane design 25
2.6 Grid of experimental data points that can be used for interpolation of wall static pressure distribution 25
2.7 Schematic view of the test section 26
2.8 Mach number contours showing the blockage introduced by the probe for a circular and wedge design 28
2.9 Schematic view of the wedge-shaped probe 28
2.10 Picture of the wedge-shaped probe 28
2.11 Mach number and velocity angle at half span downstream of cascade from CFD with air 29
2.12 Probe pressure for different velocity angles in free stream form CFD with air 29
2.13 Pressure traces with total pressure probe 30
2.14 Increased resolution in wake region 30
2.15 Contours of axial Mach number for air including the choked afterbody . . . 31
2.16 Choking afterbody design with throat size d 32
2.17 Pressure ratio across the vane for different afterbodies. Data is based on experiments with air. 32

3.1 Nozzle shape determined by MoC based on k and REFPROP (Mach 1.6, Pentane: $T_r = 1.17$ $p_r = 2.97$) 36
3.2 Supersonic vane design with incorporated leading edge 36
3.3 Geometry of an exemplary turbine stage 38
3.4 3D grid independence study 39
3.5 2D Mesh for the transonic vane. Note that only every 2^{nd} mesh line is displayed. 40
3.6 2D Mesh for the supersonic vane. Note that only every 2^{nd} mesh line is displayed. 40
3.7 2D grid independence study 40
3.8 Mesh of stage showing vane and rotor leading edge 41
3.9 Mesh of stage showing detailed view of vane trailing edge and rotor leading edge 41

4.1 Isentropic Mach number distributions for argon, air, CO_2 and R134a (experiment on the left, CFD on the right) 44
4.2 Centre-line Mach number distribution with stream-wise positions at the (a) nozzle exit and (b) suction surface trailing edge (lines: CFD, symbols: experiment) 45

4.3 Isentropic Mach number at the axial position of the trailing edge. Argon and R134a. (lines: CFD, symbols: experiment) 46
4.4 Centre-line Mach number distribution for R134a at $Z = 0.88$ (lines: CFD, symbols: experiment) 47
4.5 Isentropic Mach number at the axial position of the trailing edge for R134a at $Z = 0.88$ (lines: CFD, symbols: experiment) 47
4.6 Mach number contours at mid-span showing the location of the wake traverse 48
4.7 Comparison of wakes extracted from CFD to experimental measurements . 49

5.1 Vane design for transonic and supersonic design space (e.g. argon $k = 1.67$ and R134a $k = 1.08$) 53
5.2 Mach number distribution for argon and R134a with redesigned vanes (e.g. $M = 1.45$) 54
5.3 Expansion process of CO_2 on enthalpy-entropy plot showing the vane loss . 55
5.4 Mixed-out loss coefficient from 2D CFD at $Re = 1.7\text{x}10^6$ 55
5.5 Control volume to define loss coefficient split 57
5.6 Loss breakdown against design Mach number for argon and R134a at $Re = 1.7\text{x}10^6$ 58
5.7 Oblique shock loss variation for supersonic vane at $M_{\text{out}} = 1.5$ at the nozzle centre-line 59
5.8 Control volume for 1D mixing calculation 59
5.9 Trailing edge loss from 1D analysis and 2D CFD 61
5.10 Trailing edge loss from 1D analysis; circles denote base pressure extracted from CFD (Mach 1.30) 61
5.11 Prandtl-Meyer fan at trailing edge with the example of argon and R134a at Mach number of 1.3. The solid line denotes a Mach number of 0.5. 62
5.12 Trailing edge loss plotted against effective base pressure coefficient for several Mach numbers and working fluids 64
5.13 Variation of mixed-out loss coefficient relative to air for different exit Mach numbers 65
5.14 Loss correlation within the *k-M* design space 66
5.15 Isentropic exponent of gas mixture of argon and CO_2 as function of mass fraction of argon 67
5.16 Computed loss for gas mixture 67

6.1 Expansion of Pentane to Mach 1.3 close to critical point and $Z = 0.477$ (p_r = 0.875, T_r = 0.984) 70
6.2 Computed range of variation in α_{poly} with Z for pentane 71
6.3 Contours of α_{poly} for Pentane on T-s diagram 71
6.4 Prandtl-Meyer function for pentane at Mach 1.30 and its derivative (marked in red) 72
6.5 Range of Prandtl-Meyer function and fundamental derivative at Mach 1.30 for different regions of Z (all fluids) 73
6.6 Extent of fluid properties at fixed $Z = 0.6$ (all fluids) 74
6.7 Example Mach number contour with extent of centre-line indicated 75
6.8 Centre-line Mach number for $\alpha_{poly} \approx 0.34$ 75
6.9 Centre-line Mach number for $\alpha_{poly} \approx 0$ 76
6.10 Total loss for matched fluids ($\nu_{M=1.3} = 0.138$, $\Gamma = 0.637$) 77
6.11 Passage, trailing-edge and total loss for different Z 77
6.12 Analytical shock loss calculation 78
6.13 Contours of analytical shock loss for pentane on T-s diagram. Iso-bars are drawn at p_c and 1 atm. 78
6.14 Shock loss plotted against isentropic exponent for different regions of compressibility factor (pentane) 79
6.15 Shock loss plotted against Prandtl-Meyer angle at shock Mach number (pentane) 80
6.16 Shock loss at grid points plotted against Prandtl-Meyer angle at shock Mach number (all fluids) 80
6.17 Effect of Z on ζ_{shock} at different values of ν 81
6.18 Derivative of ζ_{shock} at different values of ν 81
6.19 Mach number contours of pentane showing oblique shock 81
6.20 Boundary layer thickness at suction side and pressure side upstream of the trailing edge 82
6.21 Velocity profiles within the boundary layer at two axial positions for R22 and RC318 83
6.22 Displacement thickness for laminar flow over flat plate for low and high Z . 84
6.23 Momentum thickness for laminar flow over flat plate for low and high Z . . 84
6.24 Energy thickness for laminar flow over flat plate for low and high Z 84
6.25 Loss coefficient for laminar flow over flat plate for low and high Z 84

6.26 Relative change in boundary layer loss between R22 ($Z = 0.75$) and RC318 ($Z = 0.95$) for multiple turbulence models 85
6.27 Contours of analytical mixing loss for pentane on T-s diagram. Iso-bars are drawn at p_c and 1 atm. 86
6.28 Mixing loss at grid points plotted against effective base pressure coefficient (all fluids) 87
6.29 C_{p_b} as function of isentropic base Mach number 88

7.1 Variation in efficiency with speed ratio (λ) (Whitfield and Baines (1990)) . 93
7.2 Variation in speed ratio corresponding to maximum static efficiency with specific speed (Rohlik (1968)) 93
7.3 Variation of endwalls for different isentropic exponents 95
7.4 Variation of η_{ts} with λ for CO_2 ($k = 1.22$) and R134a ($k = 1.07$) 97
7.5 Variation of η_{tt} with λ for CO_2 ($k = 1.22$) and R134a ($k = 1.07$) 97
7.6 Local loss coefficient through the stage for CO_2 ($k = 1.22$) and R134a ($k = 1.07$) 98
7.7 Expansion process of CO_2 on enthalpy-entropy plot showing the vane and rotor loss 99
7.8 Loss coefficients of the stage operating with CO_2 ($k = 1.22$) and R134a ($k = 1.07$) 100
7.9 Mach number contours for CO_2 at instantaneous snapshots 101
7.10 Mach number contours for R134a at instantaneous snapshots 101
7.11 Unsteady vane exit Mach number during one rotor passage for CO_2 and R134a 102
7.12 Mach number and entropy contour for steady vane and time-averaged unsteady vane with CO_2 103
7.13 Contours of loss at the rotor exit plane at $\lambda = 0.7$ for CO_2 and R134a . . . 104
7.14 Change in loss coefficients at $\lambda = 0.7$ for CO_2 and R134a 105
7.15 Change in kinetic energy loss at $\lambda = 0.7$ for CO_2 and R134a 106
7.16 Local loss coefficient through the stage for R22 ($Z = 0.75$) and RC318 ($Z = 0.95$) 106
7.17 Change in loss coefficients at $\lambda = 0.7$ for R22 and RC318 107
7.18 Extrapolated 2D vane loss at corresponding Mach numbers 108
7.19 Contours of loss at the rotor exit plane at $\lambda = 0.7$ for R22 and RC318 . . . 108

8.1 Contours of k and Z on T-s diagram for CO_2 ($M = 1.3$) 115

List of tables

1.1 Typical range of isentropic exponent for different turbine applications . . . 6

2.1 Design parameters of the vane used in the experiments 24
2.2 Standard deviation of experimental data for different afterbodies. Data is based on experiments with air. 32
2.3 Experimental run conditions for each working fluid: set 1 33
2.4 Experimental run conditions for each working fluid: set 2 33

6.1 Fluid properties for validation of gas dynamic matching ($M = 1.3$) 74
6.2 Fluid properties for CFD loss analysis 76

7.1 Input design parameters for the stage meanline design 94
7.2 Inlet conditions for stages with varying k 95
7.3 Inlet conditions for stages with varying Z 96
7.4 Mass flow averaged vane exit Mach numbers at different operating points . 102

A.1 List of fluids in REFPROP by Lemmon et al. (2010) 121
A.2 List of fluids in REFPROP by Lemmon et al. (2010) 122
A.3 List of fluids in REFPROP by Lemmon et al. (2010) 123
A.4 List of fluids in REFPROP by Lemmon et al. (2010) 124

Nomenclature

Latin

A	flow area	[m^2]
A^*	flow area at throat	[m^2]
a	acoustic speed	[m/s]
C_d	dissipation coefficient	[-]
C_f	friction coefficient	[-]
C_{p_b}	base pressure coefficient	[-]
$C_{p_\mathrm{b,eff}}$	effective base pressure coefficient	[-]
c_p	specific heat at constant pressure	[J/kg/K]
c_v	specific heat at constant volume	[J/kg/K]
d	diameter at rotor tip	[m]
H	shape factor	[-]
h	enthalpy	[J/kg]
i	imaginary number	[-]
k	isentropic exponent	[-]
M	Mach number	[-]
M_u	non-dimensional speed	[-]
N_s	specific speed	[-]
$\dot{m}$	mass flow	[kg/s]
p	pressure	[Pa]
R	specific gas constant	[J/kg/K]
r	radial coordinate	[m]
s	entropy	[J/kg/K]

T	temperature	[K]
U	blade tip speed	[m/s]
V	Velocity	[m/s]
$\dot{V}$	volumetric flow	[m^3/s]
v	specific volume	[m^3/kg]
Z	compressibility factor	[-]
z	axial coordinate	[m]

Greek

α_{poly}	polytropic indicator	[-]
Γ	fundamental derivative	[-]
γ	ratio of specific heats	[-]
δ^*	displacement thickness	[m]
ε	stage loss coefficient	[-]
ζ	loss coefficient	[-]
η	isentropic efficiency	[-]
Θ	non-dimensional mass flow	[-]
θ	momentum thickness	[m]
θ^*	energy thickness	[m]
λ	speed ratio	[-]
μ	dynamic viscosity	[kg/m/s]
ν	Prandtl-Meyer function	[-]
ρ	density	[kg/m^3]
σ	standard deviation	[-]
ϕ	flow coefficient	[-]
ψ	stage loading coefficient	[-]
ω	angular velocity	[rad/s]

Subscripts

0	stagnation quantity
b	base region property
burst	property at time of bursting of the diaphragm
c	critical property
E	external to boundary layer, edge of boundary layer
in	inlet property
m	meridional direction
max	maximum achievable Mach number
out	outlet property
ps	pressure side property
r	reduced property
ref	reference property
s	isentropic quantity
ss	suction side property
t	tangential direction
te	trailing edge plane property
ts	total-to-static
tt	total-to-total
x	axial direction

Abbreviations

AR	area ratio
LE	leading edge
MoC	Method-of-Characteristics
ORC	Organic Rankine Cycle
PR	pressure ratio
PS	pressure side

Re	Reynolds number
SS	suction side
TE	trailing edge edge
VH	shape factor
VR	volumetric flow ratio

Chapter 1

Introduction

In recent years, both fossil fuel prices and public environmental awareness in times of climate change have been rising consistently. Both these factors drive a development to persuade alternative energy sources such as renewable energies (e.g. geothermal and solar thermal) and other unused low-quality energy sources. Low-quality or low-temperature sources are for instance the residual heat of gas turbine power plants or an IC engine or even the waste energy of industrial processes.

Generally, in terms of power production, one uses open or closed power cycles where the employed working fluid usually is steam or air. Open gas cycles are the preferred method when one has cheap gas, for instance, and closed steam cycles are traditionally chosen for coal and nuclear energy sources. These systems are dominant for stationary, large scale power production. However, there is a large variety of energy sources where neither steam nor gas cycles offer a technical and economical solution (Macchi and Astolfi (2016)).

While in the past 'low-graded' energy sources might have been ignored or the energy might just have been expelled into the atmosphere, nowadays there is a much bigger motivation to make use of these energies as well. This is where Organic Rankine cycles come into play with their ability to generate useful energy from low-temperature heat sources at various capacities. ORC power systems have undergone rapid growth in recent years and are possibly the most flexible energy conversion technology in terms of capacity and temperature level (Colonna et al. (2015)).

An ORC cycle is an engine based on a thermodynamic Rankine cycle, where the working fluid is an organic compound instead of water. While there exist a whole range of different ORC turbines, the expander of ORC cycles usually consists of a single-stage radial turbine which means they are more compact and less prone to fail and needing maintenance. Hence, they offer a more cost-effective solution compared to a multistage axial turbine. The working

fluids employed in ORC cycles are molecular complex fluids that cannot be regarded as ideal gases. The real gas behaviour plays a vital role in the aerodynamics within the turbine. Typically the inlet condition to the turbine is such that the gases operate within what is called 'the dense gas region' where real gas effects have a profound impact on the gas dynamics (as explained later in the thesis). The impact on the gas dynamics will be universal and thus extend their influence beyond ORC turbines. All turbines that operate with 'real gases' such as supercritical CO_2 or steam turbines will be subject to real gas effects.

1.1 Turbine principles

The aim of this dissertation is to assess how turbine performance is affected by real gas effects. Generally speaking, a turbine extracts work from the fluid through expanding the working fluid to a lower pressure. Figure 1.1 shows such an expansion process of a radial turbine on an enthalpy-entropy plot.

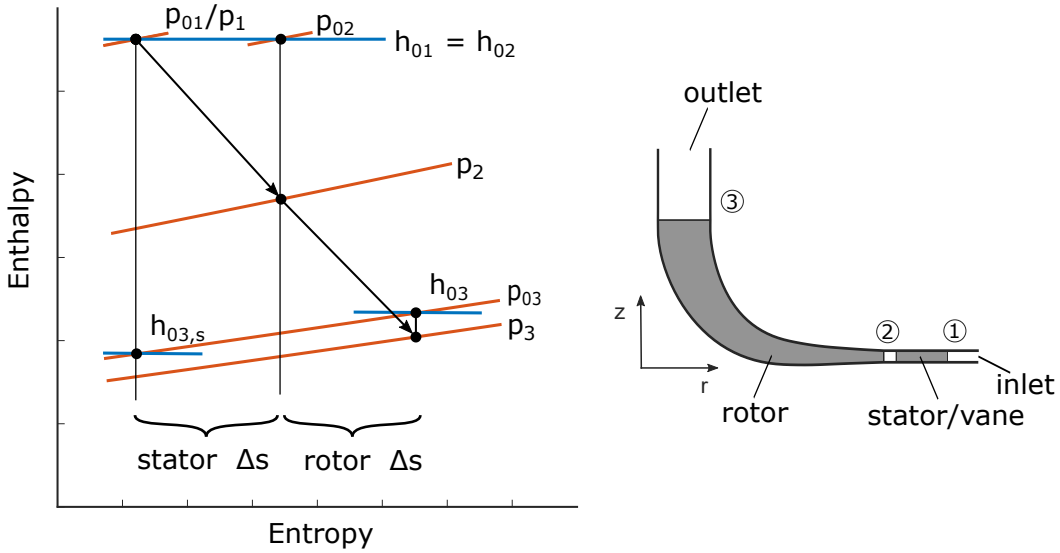

Fig. 1.1 Expansion through a turbine on enthalpy-entropy plot

First, in the stator/vane the flow is expanded from the inlet conditions (p_0, T_0) to a high velocity. For high-pressure radial turbines, as they are commonly used in ORC, the vane consist of a converging-diverging nozzle that will accelerate the flow to high Mach numbers. Such a nozzle will choke the flow at its throat, which means that the throat area A^* will set the mass flow through the turbine. Secondly, within the rotor, the flow is further expanded while extracting work ($\Delta h = h_{01} - h_{03}$) and reducing the velocity of the flow. Both of these expansion processes affect the overall performance of the turbine. The lost work of the

turbine ($h_{03,s} - h_{03}$) is the effect of the loss that is generated in both these processes through a rise in entropy (Δs). For the case of the vane, most of the loss is usually generated through the mixing process at the trailing edge and boundary layer loss within the passage (Denton (1993)). Within the rotor, most of the loss is usually generated through the unsteady interaction with the vane, endwall and secondary flows and mixing at the trailing edge (Wheeler and Ong (2014); Whitfield and Baines (1990)).

This thesis aims to show how the different loss mechanisms are affected by either varying the working fluid of a turbine or only through a change in operating conditions (p_0, T_0). Thus, one needs to define some parameters that will set the gas dynamic behaviour of the fluid. Within this chapter, first, some known parameters are presented that are used to describe real gases. Secondly, the known changes in aerodynamic behaviour due to the previously introduced parameters will be presented.

1.2 Gas properties

In this first section, a series of non-dimensional parameters are introduced that are commonly used to specify gas dynamic behaviour of real fluids. Initially, the author would like to define what is regarded as a real gas/fluid within this thesis and what sets it apart from an ideal or perfect gas.

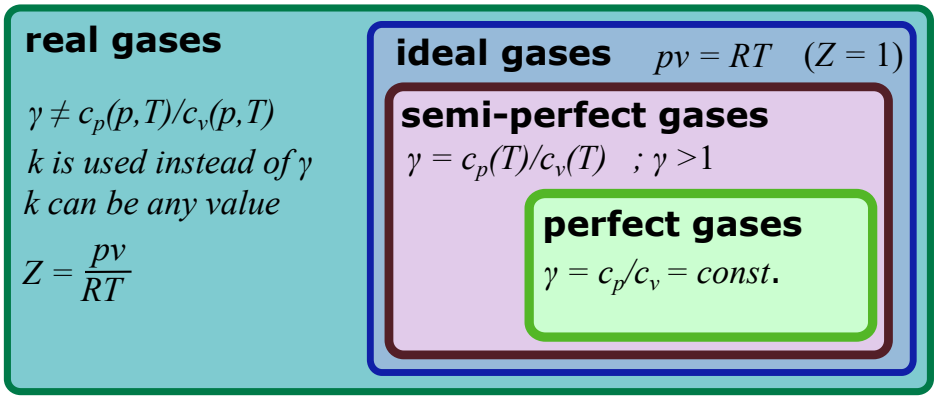

Fig. 1.2 Different categories of gasses

In figure 1.2 different types of gases are shown. It shows that real gases include all the possible gases, ranging from a simple perfect gas to some molecular complex fluid that requires sophisticated equations of state to be modelled correctly.

Ideal gases include all fluids that obey the ideal gas law ($pv = RT$) and thus have a compressibility factor of one. For an ideal gas, the isentropic expansion factor γ is always equal to the ratio of specific heats.

For the case of a perfect gas, γ will be constant across all thermodynamic states, as the heat capacities (c_p, c_v) are both constant across all pressures and temperatures. Hence, when looking at an isentropic expansion process of a perfect gas (an expansion at constant entropy) the following polytropic relation is valid:

$$pv^n = \text{const.} \tag{1.1}$$

where

$$n = \gamma$$

In the case of a semi-perfect gas, both heat capacities are dependent on temperature. Thus, for a semi-perfect gas, γ will vary depending on the thermodynamic state. This means that an isentropic expansion of a semi-perfect gas will depend on the exact location on an enthalpy-entropy space.

Outside the ideal gas region, the compressibility factor Z can be smaller and larger than one, and the heat capacities (c_p, c_v) can also vary with pressure. Furthermore, the isentropic expansion factor γ is not equal to the ratio of specific heats at all times. In such a case the isentropic exponent k represents a better approximation to describe an isentropic expansion of such a fluid.

1.2.1 Isentropic exponent

The isentropic exponent k describes the relative change of density ρ and pressure p over an isentropic expansion.

$$\left(\frac{\partial p}{\partial \rho}\right)_s = k\frac{p}{\rho} \tag{1.2}$$

In the literature (Kouremenos and Kakatsios (1985); Paradissiadis (1987)) this parameter is also called the pressure-volume isentropic exponent, while there exist two more parameters: the pressure-temperature and the temperature-volume isentropic exponent. Fluids for which k is constant across a given expansion are called ‘polytropic’. An expansion of ’non-polytropic’ fluids on the other hand cannot be expressed by such a single parameter. In the case of a (semi-)perfect gas, the value of k is the equivalent to the ratio of specific heats $\frac{c_p}{c_v} = \gamma$. Furthermore, γ will also always be greater than one for all (semi-)perfect gases, while k, on the other hand, can take any value. To compute the isentropic exponent for a specific

expansion, one can look at the logarithms of the density and pressure ratio along such an isentropic expansion and apply linear regression to it (Wheeler and Ong (2013)). As such, the isentropic exponent will vary with the thermodynamic state at the beginning of the expansion (p_0, T_0) as well as the pressure ratio of the expansion. The further a fluid behaves from an ideal gas, the stronger these dependencies get. Figure 1.3 shows exemplary isentropic expansions for Pentane and R245a at different stagnation pressures. Two features can be seen in the figures. First, one can see how the gradient, and thus k, is changing for the different thermodynamic states. Secondly, it shows that the gas dynamics of the expansion can be expressed as a linear approximation. As such, the isentropic exponent represents a universal parameter to describe a fluids gas dynamic behaviour across all categories of gases/fluids.

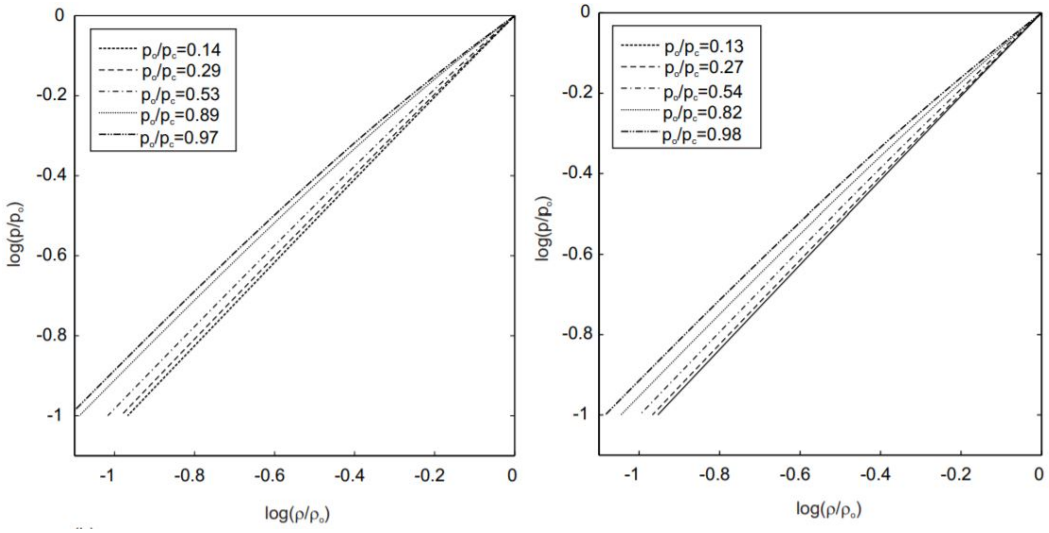

Fig. 1.3 Pressure-density plots along isentropes at a range of stagnation pressures for Pentane (left) and R245fa (right), $T_o/T_c = 1.05$ (Wheeler and Ong (2013))

Across different turbine applications, the isentropic exponent can vary substantially (see table 1.1). The highest values of k are to be found in helium turbines ($k = 1.67$) that are, for instance, employed in high-temperature gas-cooled nuclear reactors (No et al. (2007)). For gas turbines operating with air, the isentropic exponent can drop to 1.26 as the result of high turbine inlet temperatures, combustion and dissociation (Kyprianidis et al. (2011); Saravanamutto et al. (2009)). Lower values of k are found in supercritical CO_2 cycles where the isentropic exponent is around 1.25 (Dostal et al. (2006)) but also more commonly in steam turbines. Here, the isentropic exponent lays between 1.1 and 1.3, especially in the case of reheated turbine stages (Paradissiadis (1987); Rogers and Mayhew (1992)). The lowest values of isentropic exponent are generally found in ORC turbines. These tend to operate

with molecular complex fluids which then leads to values of k as low as 0.9 (Wheeler and Ong (2013)).

Table 1.1 Typical range of isentropic exponent for different turbine applications

	isentropic exponent k
Helium turbines	1.67
Gas turbines	1.26-1.4
Steam turbines	1.11 - 1.28
Supercritical CO_2 turbines	1.25
ORC turbines	0.90-1.04

1.2.2 Fundamental derivative

Another parameter that is used to describe gas dynamic behaviour, especially for dense fluids as they are often used in ORC turbines, is the fundamental derivative Γ. The isentropic exponent is closely related to the fundamental derivative Γ which was introduced by Thompson (1971) and which was meant to account for dense gas behaviour.

$$\Gamma = 1 + \frac{\rho}{a}\left(\frac{\partial a}{\partial \rho}\right)_s \tag{1.3}$$

The fundamental derivative indicates in which way the speed of sound a changes along an isentropic expansion (Thompson (1971)). For most gases, Γ will be larger than one, and thus the speed of sound will decrease as the density does the same. The region where gases fulfil $\Gamma < 1$ is called the dense gas region. For gases at a certain state within the dense gas region, the speed of sound will rise when the density decreases. In practice, along such an expansion the velocity is usually rising at a higher rate than the rate of the dropping speed of sound. Thus, the effective Mach number is still rising.

In some rather rare cases, gases can also enter the region where the fundamental derivative is negative ($\Gamma < 0$), here the classical gas dynamics are inverted. This comprises the existence of rarefaction shocks and compression waves. These gases that operate within this negative Γ region are called Bethe-Zeldovich-Thompson gases. Till today such gases remain theoretical as there is no real experimental proof of this abnormal behaviour in the supersonic region.

Generally, the fundamental derivative can be regarded as a more complex version of the isentropic exponent. In the case of a perfect gas that can be regarded as polytropic, they are

linked through the following relation:

$$\Gamma = \frac{k+1}{2} > 1 \tag{1.4}$$

1.2.3 Compressibility factor

The parameter that is commonly used for gases to characterise their deviation from an ideal gas behaviour is the compressibility factor Z.

$$Z = \frac{p}{\rho RT} \tag{1.5}$$

The compressibility factor describes the ratio of the specific volume of a fluid relative to the volume that one would expect for an ideal gas at the same temperature and pressure. For an ideal gas the compressibility factor is equal to one ($Z = 1$), while for real gases the deviation can be negative ($Z < 1$) or positive ($Z > 1$). The closer a real gas operates to its critical point, the more significant the deviation from an ideal gas behaviour.

For fluids with simple molecular structures, one can use the generalised compressibility chart such as the one in figure 1.4. These charts use the reduced state which describes the position relative to the critical point of a fluid: $T_\mathrm{r} = \frac{T}{T_\mathrm{c}}$ and $p_\mathrm{r} = \frac{p}{p_\mathrm{c}}$ and is based on the principle of corresponding states as first introduced by Van der Waal. The principle states that all fluids, when compared at the same T_r and p_r, have roughly the same compressibility factor.

Figure 1.4 shows the experimental data for a series of fluids, which demonstrates that the principle of corresponding states is a good approximation to determine the compressibility factor Z. Still, for the scope of this thesis, the compressibility factor will be computed by using some equations of state.

1.2.4 Dependence of k and Z on thermodynamic state

In order to compute these gas properties for different fluids, some adequate equations of state are needed. One set of equations that is widely used in literature are the Helmholtz equations which can be found in: Lemmon and Span (2006); Span and Wagner (2003) and Tillner-Roth and Baehr (1994). The REFPROP routines produced by Lemmon et al. (2010) are built based on these equations of state.

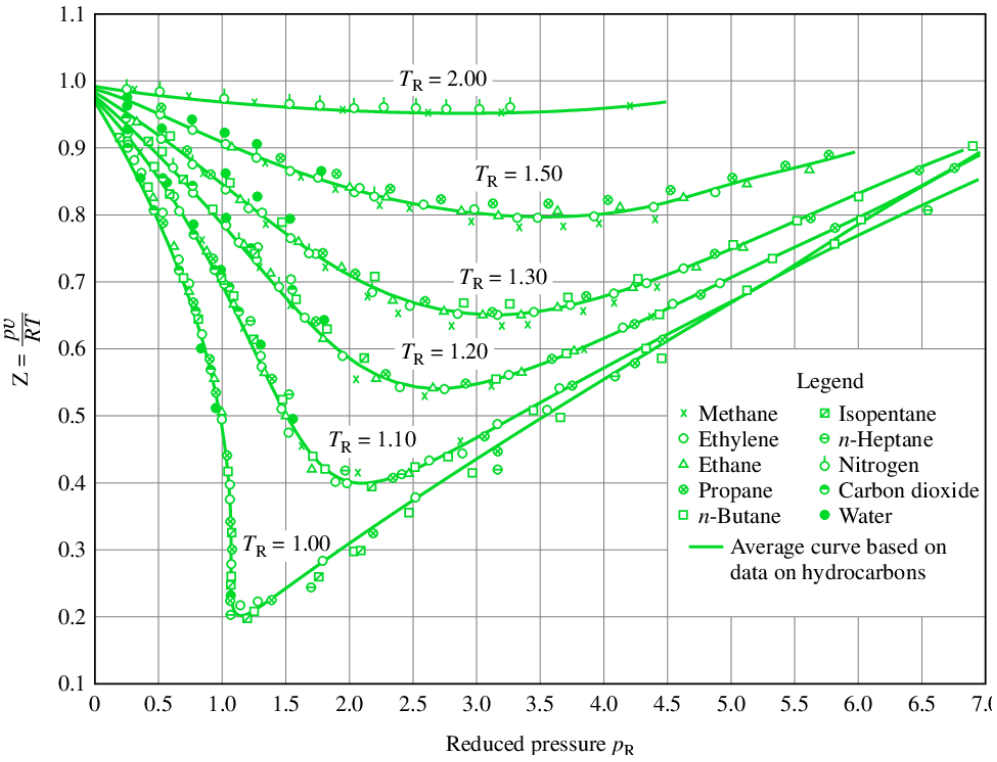

Fig. 1.4 Generalized compressibility chart for various gases (Moran and Shapiro (2014))

Pentane is a typical working fluid for ORC turbines and that is part of the REFPROP library. Figure 1.5 shows, for all feasible inlet conditions (p_0, T_0) on the temperature-entropy diagram, contours of isentropic exponent k and the compressibility factor Z.

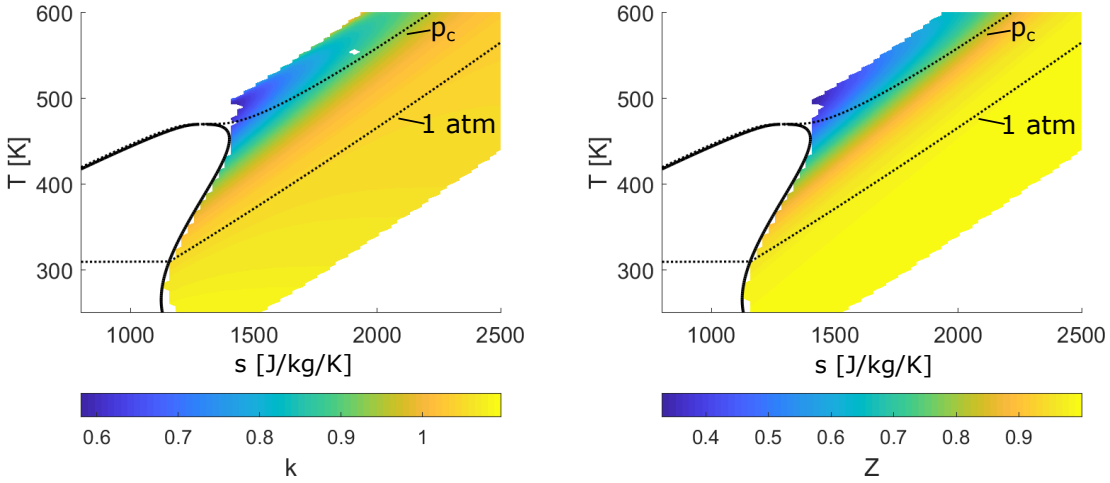

Fig. 1.5 Contours of k and Z for pentane on T-s diagram. Iso-bars are drawn at p_c and 1 atm.

While the compressibility factor is computed locally, the isentropic exponent is computed by regarding an expansion to the design Mach number. Here, the design Mach number is set to 1.30. The limits of feasible inlets are defined by the limits of the REFPROP equations of state as well as the design Mach number. The expansion to the design Mach number cannot go into the saturation dome.

Both the isentropic exponent and the compressibility factor show quite similar behaviour, whereby there is a strong dependency on pressure and weaker temperature dependence. Specifically, both k and Z are reducing for increasing pressures and increasing temperatures. At supercritical pressures ($p > p_c$) the lowest values of isentropic exponent and compressibility factor are to be found. This is in line with the generalised compressibility chart shown in figure 1.4. At atmospheric pressure, and below, Z is approximately 1. Approaching the critical point though, Z reduces and is even dropping below values of 0.5. The isentropic exponent behaves similarly, whereby the sensitivity of k increases when the minimum k at the critical point is approached.

1.3 Gas dynamics

Organic Rankine Cycles are usually designed as single-stage turbines with very high pressure ratios. Hence, these turbines often operate at supersonic Mach numbers which is why it is essential to understand how the gas dynamics are changing between working fluids or when the thermodynamic state of a fluid is changing. The previously discussed isentropic exponent and fundamental derivative affect the gas dynamics. Specifically, k has two known effects on the gas dynamics, a 1D effect and a 2D effect.

First, the 1D effect, for different values of k (or γ) a different area ratio is needed to expand a flow to a specified Mach number. This behaviour is represented in figure 1.6, which shows in a simplified form that for a fixed Mach number, one needs a larger area ratio for a fluid of low isentropic exponent and respectively a smaller area ratio for fluids with a high k. Here, the area ratio is defined as the flow area A at the end of the nozzle, relative to the throat area A^*.

The second effect k has on the inviscid gas dynamics is a two dimensional effect and has its root in the difference in the Prandtl-Meyer function of the fluids. For that reason the link between the Prandtl-Meyer function and isentropic exponent will be further discussed. For polytropic fluids, the Prandtl-Meyer function ν can be directly determined by k. Wheeler

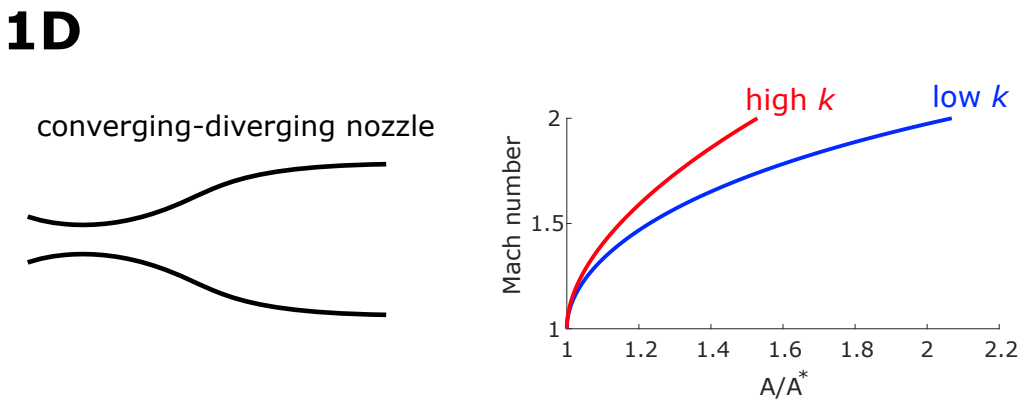

Fig. 1.6 1D effect of k on inviscid gas dynamics

and Ong (2013) have shown that:

$$\nu = \frac{1}{\xi}\tan^{-1}(\xi\beta) - \tan^{-1}\beta \tag{1.6}$$

where

$$\xi = \sqrt{\left(\frac{k-1}{k+1}\right)}$$

and

$$\beta = \sqrt{M^2 - 1}$$

The above equation is valid for values of isentropic exponent larger than one. The equation for the Prandtl-Meyer function for the cases where k is equal to one or smaller can be seen below.

for $k = 1$:

$$\nu = \cot^{-1}\beta + \beta - \frac{\pi}{2} \tag{1.7}$$

for $k < 1$:

$$\nu = \frac{1}{z}\tanh^{-1}(z\beta) - \tan^{-1}\beta \tag{1.8}$$

and

$$z = i\xi$$

The Prandtl-Meyer function for various values of k is shown if figure 1.7. It can be seen that for the case of air ($k = 1.4$) an inviscid turning is not possible beyond a certain turning angle. For lower values of k this maximum turning angle is rising and vice versa. For fluids with $k < 1$, the maximum turning angle becomes infinite, though there is a maximum Mach

number that can be achieved for fluids of $k < 1$. This maximum Mach number M_{max} that can be achieved for those fluids is give by $M_{max} = \sqrt{-2/(k-1)}$.

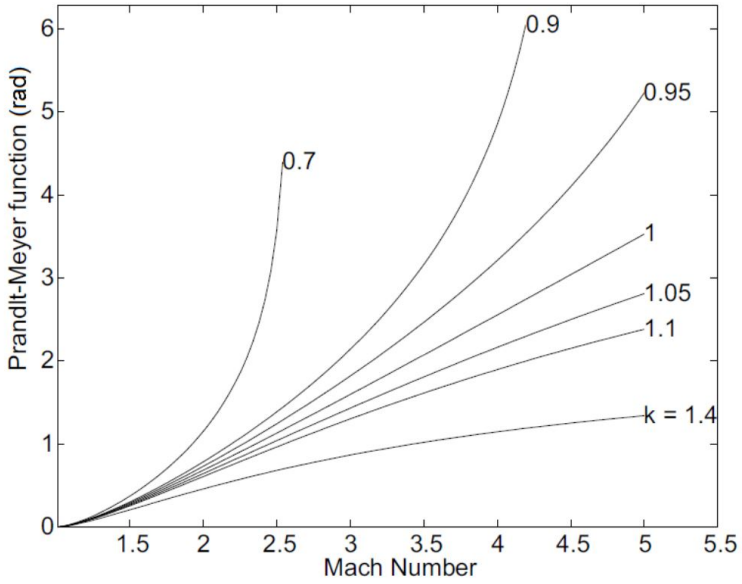

Fig. 1.7 Variation of Prandtl-Meyer function with Mach number for several values of k (Wheeler and Ong (2013))

Figure 1.8 shows again the simplified case of high and low k. It becomes obvious that for a lower value of the isentropic exponent, a larger Prandtl-Meyer turning angle is needed to achieve the same exit Mach number as for a high value of k. Looking at the simplified trailing edge flow pattern, this will mean that for a constant isentropic base Mach number M_b, fluids of low k will achieve a greater turning around the trailing edge.

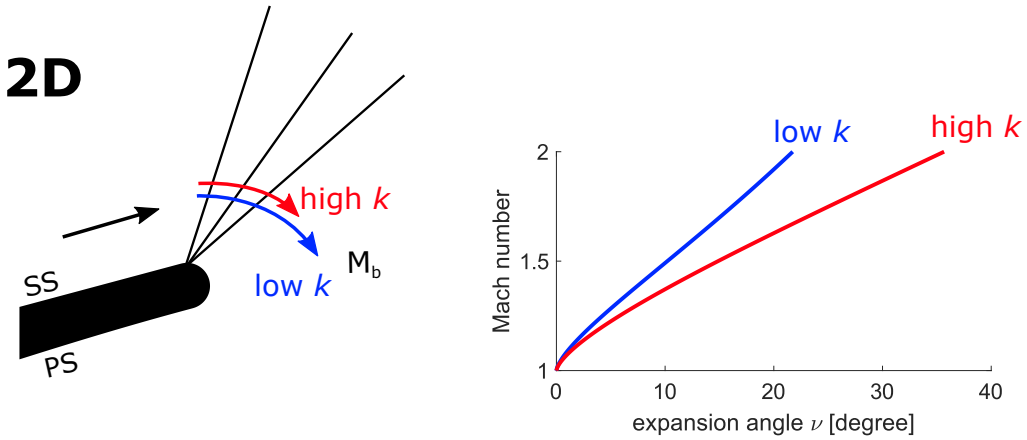

Fig. 1.8 2D effect of k on inviscid gas dynamics

These effects of k on the inviscid gas dynamics have already been shown to some extent in literature. Initially, Wheeler and Ong (2013) have come up with a vane design method for high-pressure ratio radial turbines, as they are often used for ORCs. The diverging section of the nozzle has been designed by a Method-of-Characteristics which accounts for real gas properties. Specifically, the isentropic exponent is computed for the expansion across the vane and then used to calculate the Prandtl-Meyer function on which basis the nozzle is designed. Moreover, within this study, some first vane calculations were performed which indicated that when shock-related losses are dominant, significant differences in terms of vane performance between working fluids can occur (Wheeler and Ong (2013)). The 2D effect of k has been shown by Galiana et al. (2016) and Durá Galiana et al. (2017), who looked at the trailing edge flow for different fluids. It was demonstrated that fluids that operate within the dense-gas region ($\Gamma < 1$ and thus low k) the size of the separated base region at the trailing edge is significantly reduced which is consistent with the increased Prandtl-Meyer turning angle for those fluids.

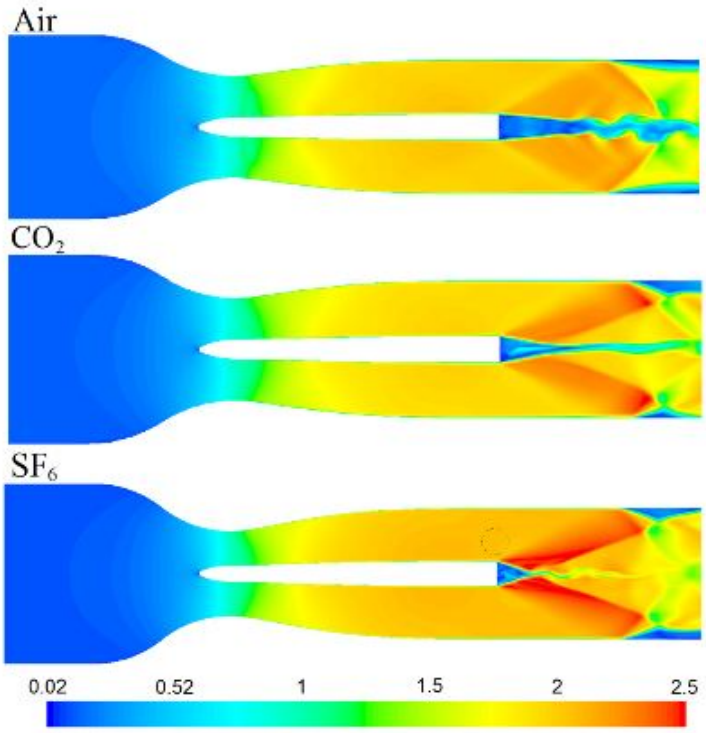

Fig. 1.9 LES predicted Mach number contours of air, CO_2 and SF_6 (Galiana et al. (2016))

Cramer and Crickenberger (1992) have studied inviscid aerodynamics in the dense gas region. For certain dense gases, they have found, that the Mach number can actually decrease

with rising Prandtl-Meyer function. This behaviour is called non-classical gas flow and occurs for $J > 0$. Hereby, J is defined as $J = 1 - \Gamma - M^{-2}$. Effectively in the non-classic gas region, a supersonic expansion would lead to a reduction of the flows Mach number. For a perfect gas, it can be shown that $J < 0$ at all times. The same is true for fluids with $\Gamma > 1$ where $J < 0$ for all pressures and temperatures.

1.4 Real gas performance

Besides the changes in gas dynamics between the fluids, it is essential to know how the performance of the turbine is affected through potential changes in the loss mechanisms. As stated before, the trailing edge contributes significantly to the overall loss within the vane/stator.

The previously mentioned study by Galiana et al. (2016) have shown a reduction in the size of the base region for fluids that operate within the dense-gas region ($\Gamma < 1$ and thus low k). Consequently, Galiana et al. (2016) concluded that inviscid contributions to the trailing edge loss are significantly increased, while viscous contributions to the trailing edge loss are reduced.

One early approach to predict the efficiency of a turbine operating with non-conventional fluids was made by Macchi and Perdichizzi (1981). They looked at predicting the efficiency for axial-flow turbines under those conditions. They argued that for large pressure ratios, the compressibility effects play a significant role. Molecular complex fluids will suffer from efficiency losses if they undergo larger volume variations and therefore introduces volume expansion ratio VR as a parameter that accounts for compressibility effects.

$$\mathrm{VR} = \dot{V}_{\mathrm{out,s}} / \dot{V}_{\mathrm{in}} \tag{1.9}$$

where $\dot{V}$ denotes the volumetric flow at the inlet and outlet respectively.

Besides the expansion ratio VR,Macchi and Perdichizzi (1981) used the shape factor VH which accounts for the actual turbine dimensions as well as the specific speed N_{s} to define the design space of possible turbines.

$$\mathrm{VH} = \sqrt{\dot{V}_{\mathrm{out,s}}} / \Delta h_{\mathrm{s}}^{1/4} \tag{1.10}$$

$$N_{\mathrm{s}} = \omega (2\pi/3600) \sqrt{\dot{V}_{\mathrm{out,s}} / \Delta h_{\mathrm{s}}^{3/4}} \tag{1.11}$$

where Δh_{s} denotes the isentropic enthalpy change within the turbine.

Based on the given parameters, a performance map of is shown in figure 1.10, which shows the expected efficiency assuming the specific speed is at its optimal value. The presented performance map has been obtained by employing a design optimisation based on several loss correlations. Overall it shows that lower values of volumetric flow ratio achieve higher turbine efficiencies.

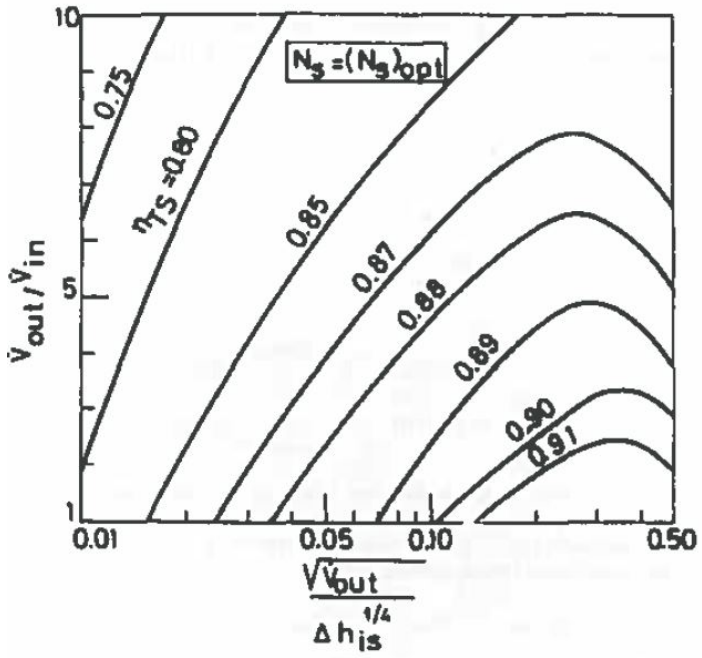

Fig. 1.10 Efficiency prediction for an axial turbine stage at optimum specific speed (Macchi and Perdichizzi (1981))

Based on the previously presented work by Macchi and Perdichizzi (1981), an adaption has been made to obtain some design criteria and efficiency predictions for radial machines as well (Perdichizzi and Lozza (1987)). Similar to the axial turbines, they use three different parameters to predict efficiency. Again they choose a volume expansion ratio VR instead of a pressure ratio to extend the validity of their design criteria to working fluids with different thermodynamic behaviour. The resulting performance map is shown in figure 1.11.

Again it shows that the predicted efficiency drops for high values of VR. Perdichizzi and Lozza (1987) state that the reason for this lays with the relatively small blade height at the stator and the rotor inlet. This is the result of the very low volume flow rate relative to the volume flow rate at the exit. They further argue that compressibility, compared to the previously studied axial turbines, does not produce dramatic losses in the various turbine designs. Instead, the rise in loss is due to the smaller blade heights of the vane.

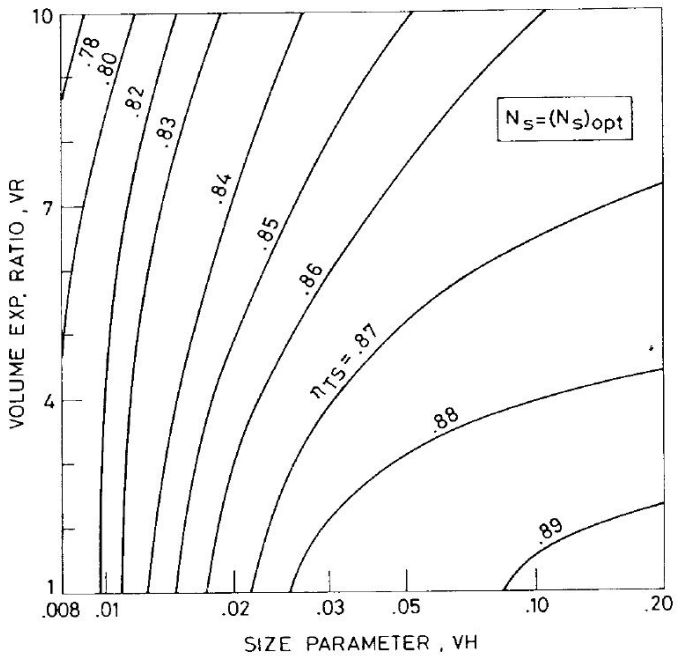

Fig. 1.11 Efficiency prediction for a radial turbine at optimum specific speed (Perdichizzi and Lozza (1987))

Both studies by Macchi and Perdichizzi include the thermodynamic properties of the working fluid in the initial design process of the turbomachine, which defines the geometry and blade angles at the inlet and exit of the turbine.

In the last years, a lot of the research has tended to focus on cycle optimisation of ORC by including real gas thermodynamics. Thereby efficiency prediction methods for axial and radial turbines have been included in the ORC cycle performance. While previously the turbine efficiency was assumed to be constant in the initial ORC cycle optimisation, more recent studies included the previously defined loss correlations for the volumetric expansion ratio VR and shape factor VH (see figure 1.10 and 1.11) as performance predictors within the initial cycle optimisation (Stijepovic et al. (2012) and Lazzaretto and Manente (2014)).

The latter of the two studies points out that the VR and VH both depend on the fluid properties, which need to be considered for both the cycle and the turbine performance prediction. Therefore, including the VR-VH efficiency correlation in the initial cycle optimisation, accounts for the various fluid properties at each step of the design process of an ORC system. While Lazzaretto and Manente (2014) argue that their initial predictions for the overall performance of the designed ORC system is much closer to reality with their

new inclusion, they acknowledge the fact that the loss correlation is only based on older computations and thus experimental data is needed to validate and update those charts.

In the study by Stijepovic et al. (2012), the volumetric flow ratio VR is expressed in terms of the compressibility factor Z, which defines the relationship between pressure, density and temperature for a real gas at a specific state.

$$\mathrm{VR} = \frac{\dot{V}_{\mathrm{out}}}{\dot{V}_{\mathrm{in}}} = \frac{\rho_{\mathrm{in}}}{\rho_{\mathrm{out}}} = \frac{Z_{\mathrm{out}}}{Z_{\mathrm{in}}} \cdot \frac{T_{\mathrm{out}}}{T_{\mathrm{in}}} \cdot \frac{p_{\mathrm{in}}}{p_{\mathrm{out}}} \tag{1.12}$$

Based on the finding by Macchi and Perdichizzi (1981) that have shown that lower values of VR tend to lead to higher turbine efficiency, Stijepovic et al. (2012) state that fluids with higher values of the compressibility factor at the turbine inlet are preferred for higher turbine efficiency.

The compressibility factor is also used by Manente and Lazzaretto (2012) to correctly compute the isentropic enthalpy change in the expansion process of an ORC system and thus the maximum net work output. The change in specific enthalpy between the inlet and outlet can be calculated as follows:

$$\Delta h = \int_{\mathrm{in}}^{\mathrm{out}} c_{\mathrm{p}} \mathrm{d}T - \int_{\mathrm{in}}^{\mathrm{out}} \left[\frac{RT^2}{p} \left(\frac{\partial Z}{\partial T} \right) \right] \mathrm{d}p \tag{1.13}$$

The first term of the real enthalpy drop is linked with the temperature drop $h_{\Delta T}$, and the second term is connected with the reduction in pressure. For four exemplary ORC turbines with different working fluids, the real enthalpy drop is computed and plotted as a ratio to the enthalpy drop linked to temperature against compressibility factor. The results in figure 1.12 shows that different fluids collapses on one line ($f(Z)$) and hence the real enthalpy change of an expansion interval can be approximated as: $\Delta h \approx c_{\mathrm{p,in}}(T_{\mathrm{in}} - T_{\mathrm{out}}) f(Z)$. Moreover, the results indicate that the theoretical work output is reduced for working fluids of low Z.

A study conducted by Zhang et al. (2017) analyses how a dense gas as a working fluids affects turbine performance. Therefore they compared the performance of an ORC turbine operating with either R245fa as working fluid or air. Based on their computational analysis, they conclude that the specific ORC turbine with R245fa will be subject to a 3-4% drop in efficiency compared to a similar turbine that is operating with air. The single biggest driver for this difference in performance is the increased rotor passage separation vortex for R245fa.

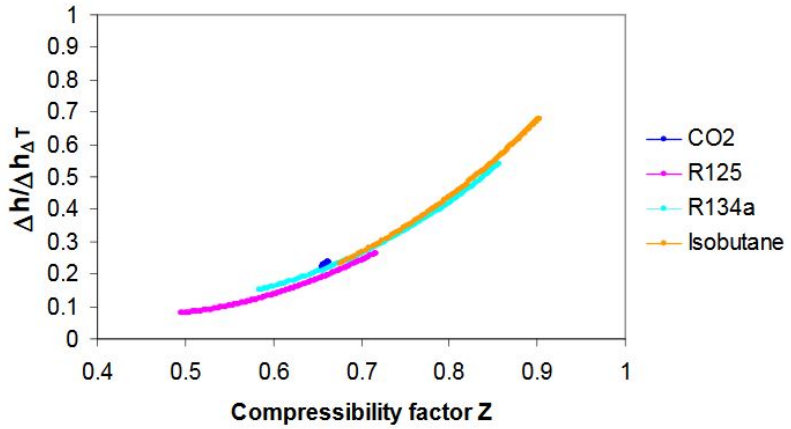

Fig. 1.12 Correlation obtained between Z and the ratio between real enthalpy change and enthalpy change evaluated from the temperature drop (Manente and Lazzaretto (2012))

Another computational study has been done by Wheeler and Ong (2014), who looked at the unsteady flow field of a typical ORC radial turbine. Instead of comparing the performance between working fluids, the focus of this study was to identify the dominant loss mechanisms in ORC turbines that operate high pressure rations/high Mach numbers. One of the key findings of that study, shown in figure 1.13, was that the vane is the most significant contributor to the overall loss of such a stage. This is primarily driven by the high mixing loss downstream of the trailing edge. Other loss mechanisms in the vane are shock losses and endwall losses. The split of the loss in the rotor shows that the mixing loss is less significant in this part of the turbine. Besides shock and endwall losses, the unsteady interaction between the rotor and stator/vane play an important role. Furthermore, the overall rotor loss can be reduced if the endwalls are designed in such a way that the flow is subsonic in the relative frame of the rotor (ROTOR 2).

The study by Sciacovelli and Cinnella (2014) focused on a transcritical axial multistage ORC turbine, by comparing working fluids that operate at sub- and supercritical inlet conditions. It was found that there is no noticeable change in the viscous losses between the different fluids (R134a, R245fa and CO_2). The differences in efficiency that were observed in this study are based on differences in shock loss. These differences were explained by weaker shock strengths for the supercritical fluids, which are subject to higher dense gas effects and thus are expanded to lower Mach numbers within the turbine stages.

Rinaldi et al. (2016) have conducted an unsteady computational study of a highly supersonic ORC turbine, whereby they focused on the unsteady interaction between the stator

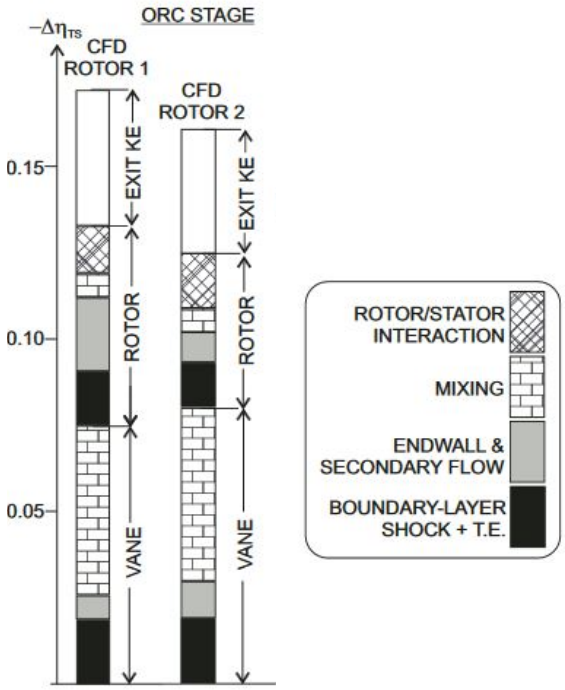

Fig. 1.13 Breakdown of predicted loss contributions to efficiency (Wheeler and Ong (2014))

and rotor. There are strong shocks coming off the trailing edge of the stator, which lead to a highly unsteady loading on the rotor blades. Their analysis showed that the unsteady loading does not increase the loss significantly (1.4% of overall loss). Overall they came to a conclusion that the biggest reductions of efficiency are generated in the boundary layer, at the vane and blade trailing edge and to a large degree through flow separations on the suction side of the rotor blades caused by oblique shocks. Furthermore, they highlighted the importance of using adequate equations of state when computing more complex fluids as the thermodynamic properties vary substantially within the stage.

The overall perception in the literature is that low values of Z are to be avoided to achieve the best performance. Similarly, there is a perception that operating a turbine stage in the dense gas region will lead to a drop in efficiency.

1.5 Research questions

The literature review has revealed that most performance analyses are based on loss correlation obtained for air without experimental validation or physical understanding of how the gas dynamics might change for different fluids. This is due to the general lack of detailed

experimental data of high Mach number flow of fluids of varying thermodynamic properties. Furthermore, many of the past approaches expressed changes in efficiency as a function of the volumetric expansion ratio. Still, they did not state how performance is affected by changes to the fluid properties (k or Z), which are known at the beginning of the turbine design process. Based on the previous section, the following research questions are proposed:

- How do gas properties (k, Γ, Z) affect turbine aerodynamics?
- What is the impact on loss?
- Which loss mechanisms are most affected by these gas properties?
- How can this be accounted for in future turbine design?

In order to answer the proposed research questions, the first objective has been to obtain detailed experimental data for high Mach number flow of various fluids. Such experimental validation was needed to give credibility to the computational analysis that followed. In order to isolate any effects that k, Γ or Z might have on the aerodynamics/performance of the turbine, it was needed to find a set of design parameters that ensures similarity of the loading of the blades across different fluids. Thereupon a series of simulations have been conducted ranging from steady 2D vane calculations to unsteady 3D stage calculations. Additionally, multiple analytical loss analyses have been undertaken to get a thorough understanding of the impact of k and Z on turbine performance.

The structure of the thesis is as follows:

The following chapter will describe the experimental methodology. The Ludwieg tube that has been used for the experiments is explained as well as the measurements techniques that were used to obtain the experimental data.

The computational methodology is discussed in chapter three. This also includes the design of the vanes and stages as well as the mesh and solver setting of the CFD.

The fourth chapter will show the experimental results, which are then used to validate the computational method described in the previous section. Results include detailed wall static measurements as well as wake measurements.

The effect of the isentropic exponent k on vane loss is discussed in the fifth chapter. To that end, turbine loss is analysed across a range of operating Mach numbers and isentropic exponent.

In the sixth chapter, the design space is further increased by looking at changes due to compressibility factor. For this purpose, all available fluids within the REFPROP database are considered. The analysis is based on analytical loss models and CFD.

The seventh results chapter will look at the full turbine stage. The changes in design for different working fluids are presented as well as the changes in loss for different values of k and Z are discussed.

Chapter 2

Experimental method

2.1 Transient wind tunnel - Ludwieg tube

The experiments within the scope of this thesis have been conducted with a transient wind tunnel: the Ludwieg tube. A transient wind tunnel was chosen for its capability to vary the working fluid and test-geometry independently. There are no auxiliary components that need to be changed in order to change the test setup. Working fluids can be changed by directly connecting a different gas bottle to the system, and the test geometry can be exchanged individually as well. A Ludwieg tube is also a closed system which allows for various working fluids to be used without the risk of exposing them to the ambient atmosphere. This ability becomes important once one conducts experiments with refrigerants like R134a, which impose a tremendous environmental hazard if they are vented into the atmosphere. The Ludwieg tube has previously been used to study the supersonic trailing edge flow that can be found downstream of a flat plate (Durá Galiana et al. (2017); Galiana et al. (2016)). Since then the facility has been recommissioned, a new working section has been designed to include an annular cascade and new measurements techniques. In the context of this thesis, four different working fluids were tested: argon, air, CO_2 and R134a.

A schematic view of the test rig can be seen in figure 2.1. On the right side is a dump tank and on the left side is a charge tube. The test section is placed in between the two of them, with a Mylar diaphragm sealing off the tube between the dump tank and the test section. A vacuum pump will be used to create a vacuum in the reservoir tank, and the charge tube will be filled with the desired working gas out of a gas cylinder which leads to a pressure difference at the diaphragm. Once the desired pressure is reached in the charge tube, the bursting mechanism can be activated. The bursting mechanism consists of a pneumatically activated cylinder with a piercer at its end.

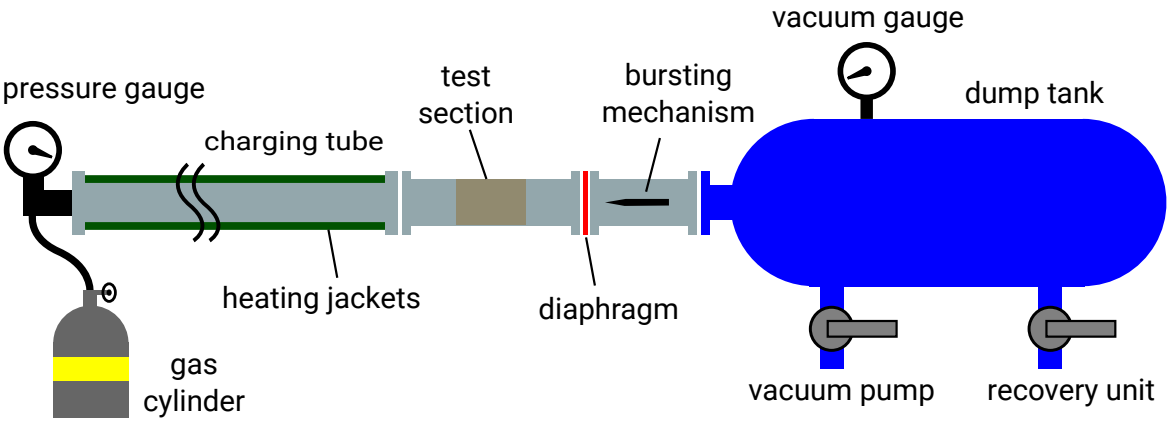

Fig. 2.1 Schematic view of the Ludwieg tube

As the diaphragm bursts, a shock wave will travel into the reservoir tank, and an expansion wave will travel down the charge tube till it is reflected at its end. During the time until the wave arrives back at the test section, the test section sees quasi-steady flow conditions. This time takes about 32 ms and 64 ms with working fluids of air and R134a respectively (see figure 2.2).

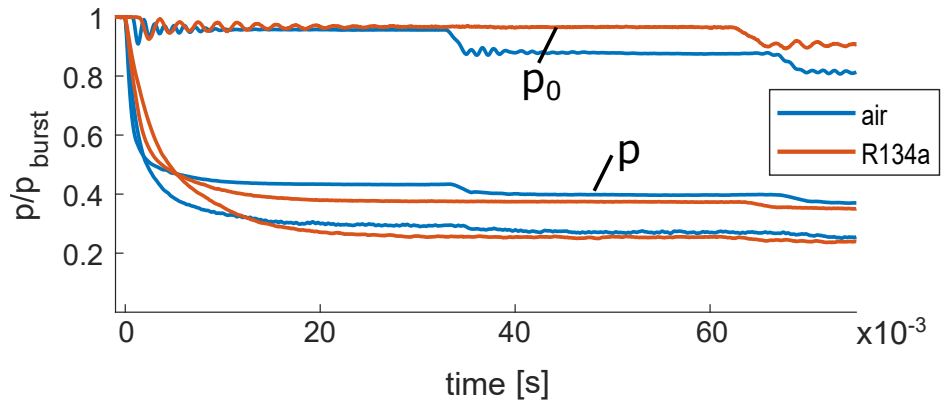

Fig. 2.2 Typical pressure traces showing run times for air and R134a

In terms of technical details, the charge tube measures 5.70 m in length and has a diameter of 50 mm. The test section itself is 0.40 m long, and the dump tank holds 150 litres. The diaphragm used for the current set of experiments is made of Mylar and has a thickness between 100 μm and 190 μm, depending on the pressure in the charge tube.

A new bursting mechanism was designed to improve the flexibility and accuracy of consecutive experiments. The bursting mechanism consists of a pneumatically activated cylinder with a piercer at its end and is located downstream of the diaphragm. This allows the use of thicker diaphragms that can be burst manually once the desired pressure is achieved,

as opposed to choosing a specific thickness that will burst at approximately the desired inlet pressure.

Heating jackets are installed around the charge tube, which allows heating the working fluid to a desired initial temperature while the charge tube is pressurised. As the rig is designed to operate with CO_2 as one possible working fluid, pre-heating is particularly important. This heating is to prevent the CO_2 from entering the two-phase-region while expanding within the vane. Thus, the initial temperature of the CO_2 will be increased to about 130 °C/400 K. Besides CO_2 the charge tube was also heated for the use of R134a.

2.2 Test section

A new test section was designed to analyse the flow through an annular cascade. The blade design for the cascade was based on the design method developed by Wheeler and Ong (2013) and is thus geometrically similar to a stator vane found in a typical ORC stage (Wheeler and Ong (2014)). Their vane design consisted of a circular leading edge, a converging-diverging nozzle, polynomial suction surface and a circular trailing edge (see figure 2.3).

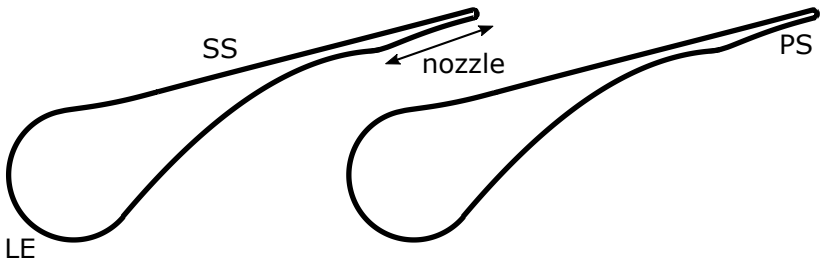

Fig. 2.3 Baseline vane design

Their design of the nozzle uses a new Method-of-Characteristics that includes dense gas effects. To that end, they adapted the original CHAR1 code by Horton, to include their proposed definition of the Prandtl-Meyer function (equations 1.6, 1.7, 1.8). The code uses Hall's series solution as initialisation and then continues with the MoC (Hall (1962)). The method uses the isentropic exponent k as introduced before, whereby k is computed by applying linear regression in the log-log space of the expansion that occurs within the nozzle. The isentropic exponent is then assumed to be constant throughout the entire expansion and is used to compute the Prandtl-Meyer function on which basis the nozzle shape is defined.

A summary of the design parameters of the vane used for the experiments of this thesis can be seen in table 2.1.

Table 2.1 Design parameters of the vane used in the experiments

Design Parameters	
Mach number	1.45
Isentropic exponent	1.4
Inlet flow angle	0°
Exit flow angle	75°

While the original design by Wheeler and Ong (2013) was for a radial stator vane, the design was transformed into an annular cascade to reduce the complexity of the test section and to ensure periodicity. The cascade was formed of eight blades with a hub diameter of 30 mm and a shroud diameter 40 mm which leaves a span of 5 mm for the vane itself. The cascade is mounted between an elliptic hub and an afterbody (see figure 2.4).

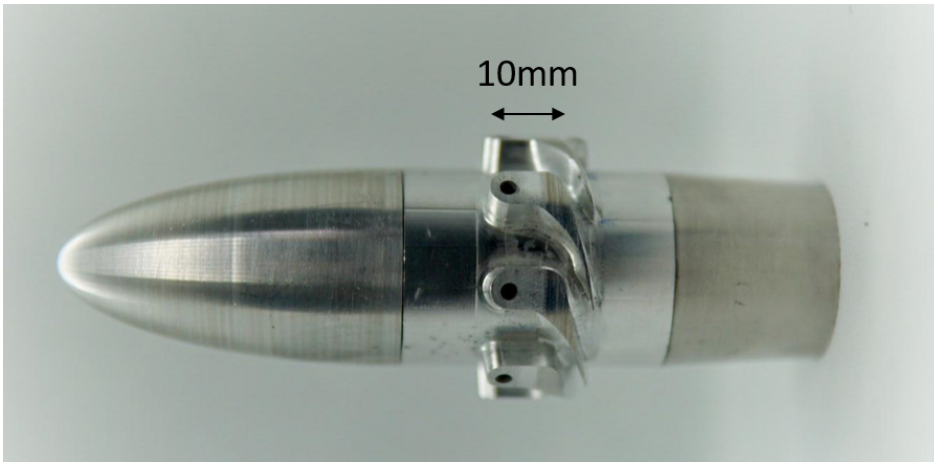

Fig. 2.4 Picture of cascade geometry mounted between elliptic hub and afterbody

The expansion of the working fluid throughout the vane was measured by placing eight pressure tappings along the centre line of the vane. The first pressure tapping is located just upstream of the throat, and the last pressure tapping is located at 12% of the chord length downstream of the trailing edge (figure 2.5). Under the assumption of identical flow through each of the passages, the actual measurements were spread out over multiple passages due to space limitations. Each pressure tapping has a diameter of 0.5 mm.

In order to increase the density of the experimental data points on the shroud of the cascade, the test section was designed in such a way that the outer casing with the pressure tappings could be rotated circumferentially relative to the cascade. This rotation of the casing can be done in increments of 2°. Figure 2.6 shows the grid of the available data points after

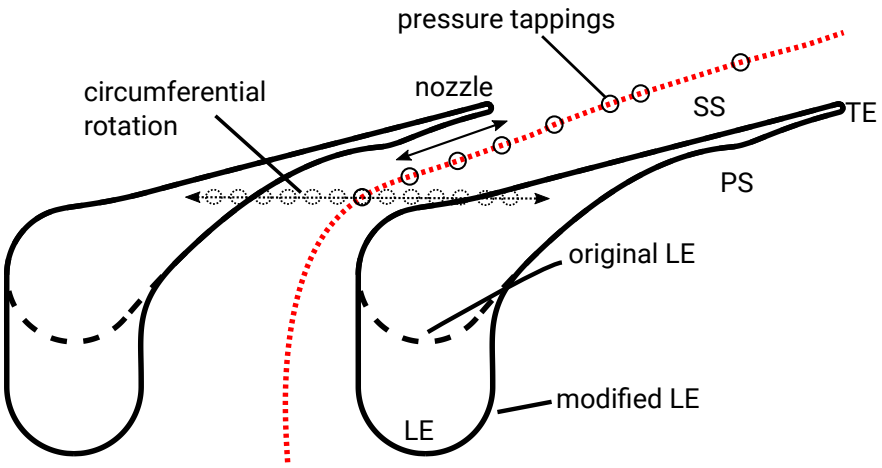

Fig. 2.5 Cascade geometry showing modification of vane design

a full sweep of measurements. The possible circumferential positions range from 0°to 46°, providing one additional data point to ensure periodicity.

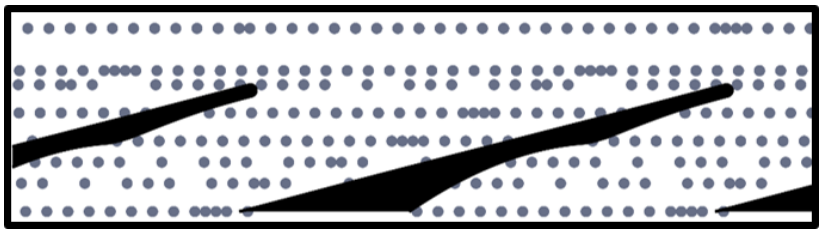

Fig. 2.6 Grid of experimental data points that can be used for interpolation of wall static pressure distribution

The leading edge of the vane had to be modified to allow for this rotation of the casing while the cascade still needed to be fixed to the non-rotating part of the test section. The cascade is held in place by dowel pins that are positioned at the centre of the circular leading edge. The leading edge was extended upstream by 5 mm to increase the space between mounting point and measurement area (see figure 2.5). As this modification is located within the subsonic region of the vane, upstream of the choked throat, this modification had no impact on the flow within the nozzle.

Figure 2.7 shows a schematic view of the entire test section. As mentioned before the cascade is geometrically fixed to the casing shown in green on the left. The middle casing, drawn in dark blue, can be rotated. To enable this relative movement of the casing, while maintaining a seal to of the test section, brass bearings and rotating seals were employed.

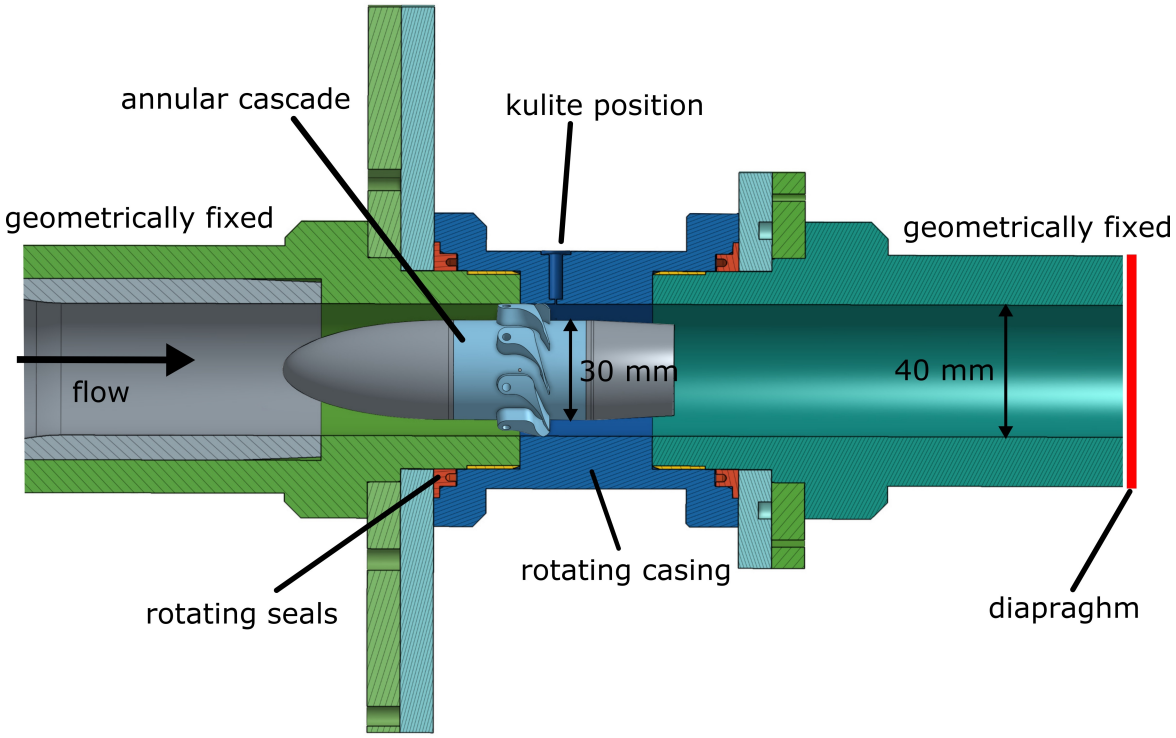

Fig. 2.7 Schematic view of the test section

2.3 Data acquisition

The data acquisition for the experimental setup consists of high-frequency pressure transducers to measure total and static pressures and thermocouples to measure the temperature at the inlet of the test section. The acquisition was performed using National Instruments (NI) hardware and a developed MATLAB code.

Pressure probes

The pressure measurements were done with Kulite pressure transducers, connected to a 'USB-6356 X-series DAQ' data acquisition system which, allowed to measure at 100 kHz. In between an analogue amplifier was used with a gain of 100.

The pressure transducers have been calibrated with a high precision modular pressure controller (GE PACE5000). The error of this calibration device is listed as 0.01% of the full-scale output of 10 bar. All pressure transducers are calibrated in incremental steps of 0.5 bar for a range from atmospheric pressure to 12 bar.

Temperature probes

As stated earlier, it is crucial to heat CO_2 when it is employed as a working gas within the Ludwieg tube to avoid any two-phase flow. In order to record the temperature that the test section sees during a run, hypodermic needles probes by OMEGA are used. Four thermocouples are placed along the length of the charge tube and just upstream of the test section. The sensitivity of the used thermocouple is rated at approximately 0.03 s, and the corresponding data acquisition hardware had a maximum sampling frequency of 100 Hz. Thus with a run time of 30 ms, one can only measure a pre-run temperature before the diaphragm has burst. During the initial expansion, there is no significant change in total temperature, as there is no work being done. Hence, the obtained temperature can be used as a boundary condition for a CFD simulation which is then compared to the experimental data.

2.4 Total pressure measurements in supersonic flow

Besides the wall static pressure measurements, an additional probe was designed to measure the wake profile at mid-span in the supersonic region downstream of the vane. Introducing a probe into the flow meant that one had to deal with blockage effects. In a first iteration of the design, a circular probe was investigated. While this design was easy to manufacture, it came with the cost of a high degree of interaction with the flow in the free stream. Figure 2.8 shows Mach number contours from a two-dimensional CFD solution including the probe. It reveals that by placing the circular probe in the flow, the shock-boundary layer interaction is amplified causing a much bigger shear-layer bubble. Repeating the same CFD with a wedge-shaped probe, showed that the disturbance of the flow could be reduced significantly with such a probe. Such wedge-shaped probes are the preferred method when measuring stagnation pressure in supersonic speeds (e.g.Ainsworth et al. (2000),Sieverding et al. (2000)). Besides reducing the blockage, the wedge-shaped design also had higher structural integrity compared to the cylindrical design. The final probe consisted of a pitot probe embedded within a 30° wedge (see figures 2.9 and 2.10). The hypodermic tubing, which was parallel to the flow had an outside diameter of 0.4 mm and inside diameter of 0.2 mm. For reference, the trailing edge thickness of the vane was 0.25 mm. These probe dimensions were chosen, as they represent the smallest sizes could be manufactured in-house. To reduce the temporal response of the probe, the Kulite pressure transducer that was used for this probe was located as close to stagnation point as possible by glueing it in the centre of the rotating probe. In

order to assure that the probe can be rotated around its own axis from the outside, as for the rotating casing of the test section, some custom rotating seals were employed.

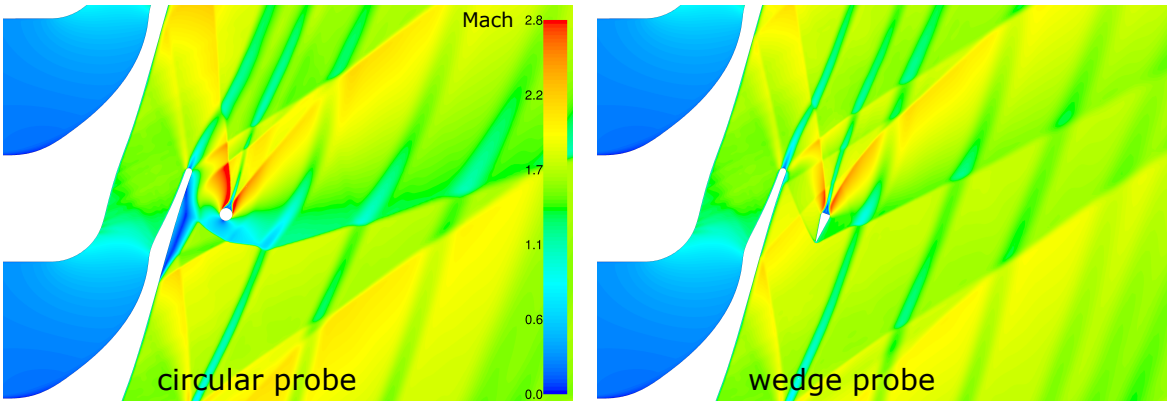

Fig. 2.8 Mach number contours showing the blockage introduced by the probe for a circular and wedge design

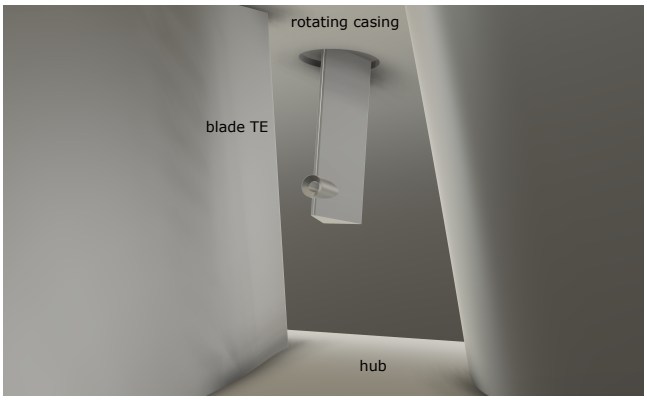

Fig. 2.9 Schematic view of the wedge-shaped probe

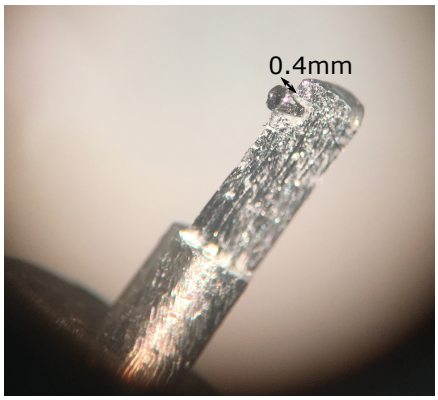

Fig. 2.10 Picture of the wedge-shaped probe

Making use of the rotational casing the probe could be used to obtain a wake profile. In order to reduce the number of consecutive runs of the experiment, the wake profile was only recorded at one angular position of the probe, the free stream velocity angle. This velocity angle was obtained by positioning the wedge in the free stream of the vane and to rotate the probe around its own axis to find the angle of maximum pressure. CFD simulations have shown that the variation of the velocity angle along the circumferential measurement positions is within $\pm$ 5°(see figure 2.11). At the same time, it was shown that the sensitivity of the probe within this region is less than 1% of the measured total pressure (see figure 2.12). Hence, the approach of measuring the wake with a fixed angle of the wedge will be very closed to the actual total pressure.

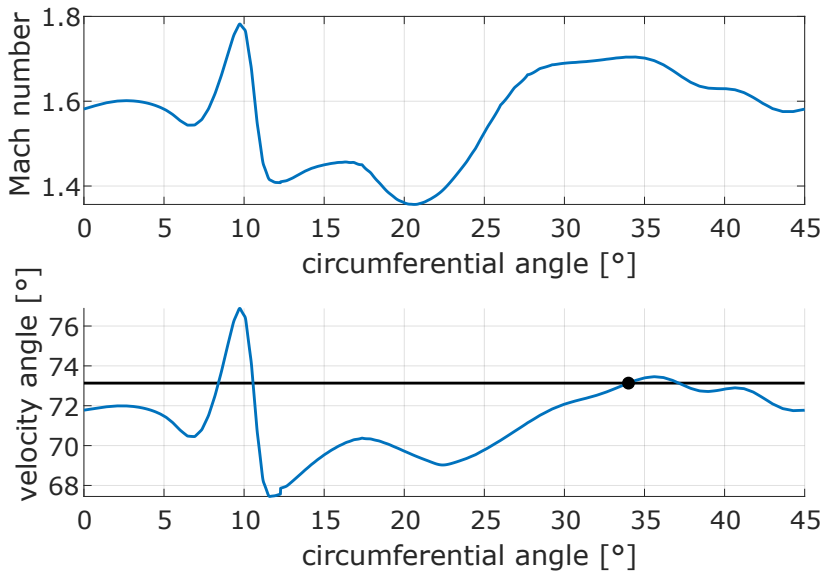

Fig. 2.11 Mach number and velocity angle at half span downstream of cascade from CFD with air

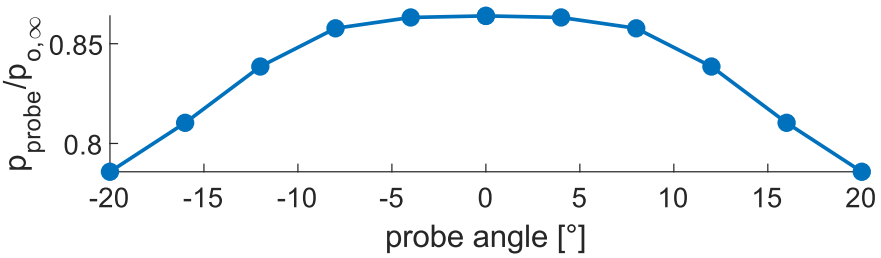

Fig. 2.12 Probe pressure for different velocity angles in free stream form CFD with air

At this point, it has to be noted that the probe is measuring the stagnation pressure within the supersonic region of the flow field. Thus, a bow-shock is formed upstream of the probe, and the probe measures a total pressure that is subject to a shock loss. This shock loss is dependent on the Mach number and the thermodynamic properties of the measured fluid. In the experimental setup, only the static pressure at the casing of the vane is measured. Therefore, the exact static pressure at the probe location at mid-span and thus the pre-shock Mach number remains unknown.

Figure 2.13 shows exemplary pressure traces of a run with air that included the total pressure probe. It shows that by locating the pressure transducer within the centre of the probe, the temporal response of the total pressure probe is much lower the run time.

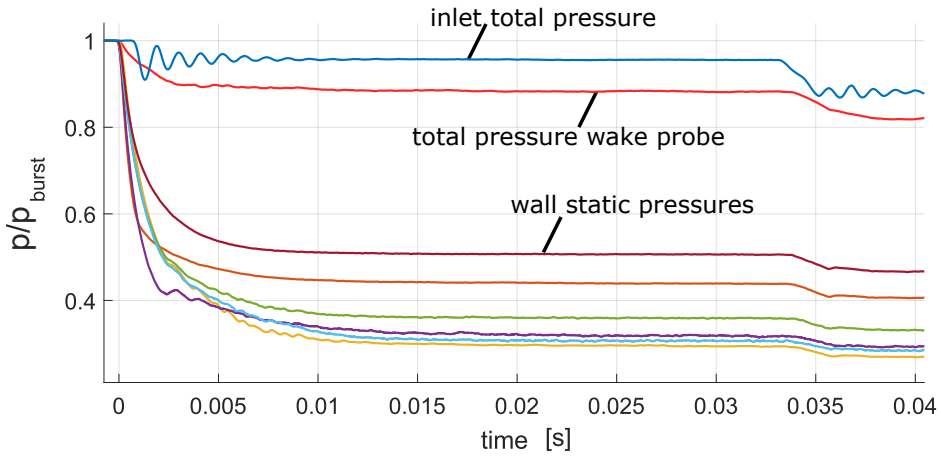

Fig. 2.13 Pressure traces with total pressure probe

For the purpose of the wake measurements, the test section was additionally modified such that it could to realise 1° rotational increments in the region of the wake, to increase the resolution of the wake measurements.

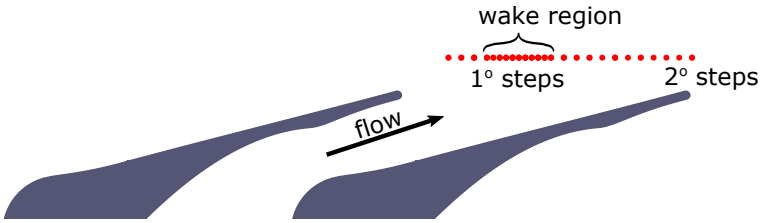

Fig. 2.14 Increased resolution in wake region

2.5 Increased repeatability via choked afterbody

There are two important quality characteristics for experiments with a transient wind tunnel: quasi-steady flow conditions during the run and run-to-run repeatability.

As seen in figure 2.13, the cascade will see quasi-steady flow conditions after the diaphragm has burst. The pressure is extracted as a mean value of a window of data points. Ideally, the standard deviation of those data points is as little as possible. To that end, the exact position in time of the sampling window (≈ 400 data points) is optimised to minimise the standard deviation of the included data points.

The second quality characteristic is the run-to-run repeatability. This is particularly important for the rotating casing, which assumes the flow to be constant between multiple consecutive runs. This quality can be measured by computing the standard deviation of the

extracted pressures at one angular position over a series of runs. This repeatability is set by the consistency of the pressure ratio across the cascade. The original design of the cascade used a tapered afterbody (see figure 2.7), which caused the flow to separate at some point downstream of the cascade. The position of the separation at the afterbody subsequently sets the pressure ratio that is achieved over the cascade. The introduction of the total pressure probe introduced another element to the flow that might impact the position of separation and thus, the pressure ratio.

In order to increase the quality of the experimental setup, a new kind of afterbody was designed: a choking afterbody. The throat (see figure 2.16) will accelerate the flow to sonic conditions in an axial direction and thus fix the pressure ratio across the cascade. Hence, this style of afterbody enables to directly control the pressure ratio across the cascade. Furthermore, the choked flow should improve the steadiness of the pressure ratio during a run as well.

Figure 2.15 shows contours of the axial Mach number on a meridional plane obtained form a CFD simulation with air. As the velocity angle of the flow is relatively high at 75°, the axial Mach number is only ≈ 0.6 at the exit of the vane, the afterbody then chokes the flow as expected, and downstream of the throat the flow reaches a supersonic velocity in the axial direction as well.

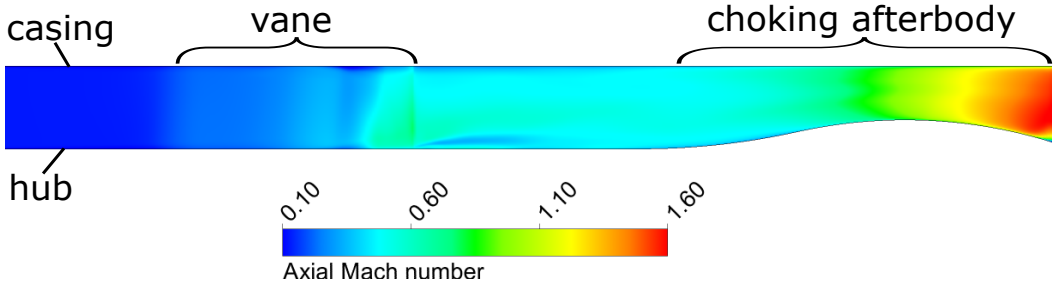

Fig. 2.15 Contours of axial Mach number for air including the choked afterbody

Multiple afterbodies were machined with different throat sizes. Figure 2.17 shows how the pressure ratio across the vane, operating with air, is impacted by a change in throat diameter d. The pressure ratio is defined as the ratio between inlet stagnation pressure and the static pressure that is the furthest downstream of the cascade. This relationship between PR and d is itself a function of the isentropic exponent. Thus, a specific afterbody was manufactured for each fluid to maintain a constant pressure ratio across all tested fluids.

To show the improvement of the quality of the runs, the standard deviation of the experimental data was compared between the tapered afterbody and the choking one. The computed standard deviation is shown relative to the local pressure and based on five

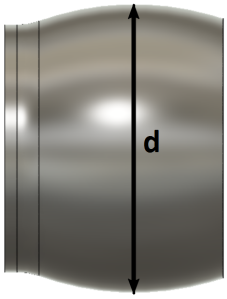

Fig. 2.16 Choking afterbody design with throat size d

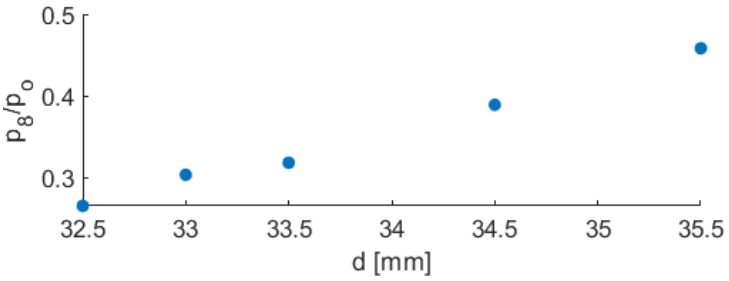

Fig. 2.17 Pressure ratio across the vane for different afterbodies. Data is based on experiments with air.

consecutive runs. The results in table 2.2 reveal that the new design of the afterbody does indeed lower the standard deviation of the experimental data. Both the run-to-run standard deviation and the standard deviation of one single run are reduced.

$$\sigma_1 = \frac{S(p_8(t_{\text{window}}))}{\mu(p_8(t_{\text{window}}))} \tag{2.1}$$

$$\overline{\sigma}_{\text{during run}} = \mu(\sigma_{1:\text{ run 1-5}}) \tag{2.2}$$

$$\sigma_{\text{run-to-run}} = \frac{S(p_{8(\text{run 1-5})})}{\mu(p_{8(\text{run 1-5})})} \tag{2.3}$$

where

S = standard deviation

μ = mean value

p_8 = wall static pressure downstream of the vane

Table 2.2 Standard deviation of experimental data for different afterbodies. Data is based on experiments with air.

	tapered afterbody	choked afterbody
$\sigma_{\text{run-to-run}}$	2.46%	0.5736%
$\overline{\sigma}_{\text{during run}}$	0.567%	0.201%

2.6 Run conditions

The experiments that were conducted in the framework of this thesis were split into two different sets. The first set was done with the tapered afterbody, while the second set used the new choking afterbodies. The experiments were conducted with four different fluids: argon, air, CO_2 and R134a, which represent a variation of isentropic exponent form 1.08 to 1.67. This corresponds to a range in fundamental derivative Γ of 1.02 to 1.35.

Table 2.3 Experimental run conditions for each working fluid: set 1

	p_0 [bar]	T_0 [K]	Re	k	Γ	Z	PR
Argon	12	300	2.7x10^6	1.67	1.35	1.0	4.66
Air	12	300	2.2x10^6	1.40	1.21	1.0	4.75
CO_2	12	400	2.0x10^6	1.27	1.11	0.98	5.10
R134a	5.6	400	1.3x10^6	1.08	1.02	0.96	4.79

During the first set of experiments (table 2.3) the heating jackets were used for the operation with CO_2 and R134a and were set to 130 °C/400 K. The runs with air and argon were conducted at room temperature. The inlet stagnation pressure that was achieved for the fluids was 12 bar, only the refrigerant was run at a lower pressure. For R134a, 5.6 bar represents the equilibrium pressure at ambient temperature, which allowed for the gas to be filled in directly from the bottle.

Table 2.4 Experimental run conditions for each working fluid: set 2

	p_0 [bar]	T_0 [K]	Re	k	Γ	Z	PR
Air	8.2	293	1.6x10^6	1.40	1.21	1.0	4.75
CO_2	8.2	400	1.4x10^6	1.27	1.11	0.98	const
R134a	5.0	293	1.6x10^6	1.07	1.02	0.88	const

For the second set of experiments, which used the new afterbody and the total pressure probe, only three fluids were tested. The summary of the inlet conditions can be seen in table 2.4. For this set, the pressure ratio across all fluids was kept constant by using an adequate afterbody for each fluid. Also, the ambient temperature and hence the inlet temperature for the refrigerant was 20 °C/293 K which achieved a lower compressibility factor Z.

For all experiments with R134a, the entire tunnel was flushed with nitrogen and then reduced to a pressure of 2 Torr before filling the tunnel with R134a. After each run, a Yellow Jacket XLT2-AP recovery unit was used to recover the refrigerant from the Ludwieg tube.

This was mandatory in order to comply with F-gas regulations. As a result, obtaining each measurement for R134a took around 4 hours, compared to air for which a run could be completed in 15 minutes. The Reynolds numbers *Re*, computed with the blade exit conditions and the chord of the blade lay in the region between 1-3x10^6 for the experiments, which is within the range of similar industrial applications

2.7 Summary

A transient wind tunnel has been recommissioned whereby the test section has been fundamentally redesigned. From the original flat plate experiment, the setup has been modified to test an annular cascade with the ability to easily vary the test geometry.

Through the use of a rotating casing, which embodies the pressure transducers, detailed wall static measurements can be recorded over many consecutive runs. Additionally, a wedge-shaped probe has been designed to measure total pressure in the supersonic flow downstream of the vane. Making use of the new rotating casing, wake profiles can now be recorded.

A new bursting mechanism and a new style of afterbody were designed to improve the reliability and quality of the experiments. This allowed precise control of the pressure ratio across the cascade.

Chapter 3

Computational method

The computational research that was carried out for this thesis was dedicated to the determination of how real gas effects influence the aerodynamics and thus the performance within an ORC turbine. This chapter explains in detail the employed computational methods such as solver settings, thermodynamic modelling, meshing and chosen turbulence model as well as the design of the geometries.

The work was split into two parts, whereby the computational approach was first compared against the experimental results. Secondly, the validated computational method was used to do a detailed analysis on how the previously discussed real gas parameters (k, Γ and Z) impact the gas dynamics within the stage. The analysis will be conducted on 2D rectilinear cascade geometries, whereby the design Mach numbers will range from subsonic to supersonic exit velocities. This will be followed by unsteady simulations of entire turbine stages operating with a variety of working fluids to determine how the previously analysed effects within the vane affect the overall performance of the stage.

3.1 Vane design

As previously stated, the design of the vanes was based on the method developed by Wheeler and Ong (2013). This method uses the isentropic exponent k, whereby k is computed based on the expansion that occurs within the nozzle. The isentropic exponent is then assumed to be constant throughout the entire expansion and is used to compute the Prandtl-Meyer function on which basis the nozzle shape is defined. While for most inlet conditions (p_0, T_0), it is a valid approach to assume that the expansion behaves polytropic (constant k), this might not always be the case. To this end, in their paper, Wheeler and Ong (2013) further introduce

a correction factor for the computation of the Prandtl-Meyer function in case the expansion is occurring close to the critical point.

For the purpose of this thesis, the MoC has been further adopted to be applicable to non-polytropic fluids as well. It was adapted in such a way, that the design code uses the REFPROP routines directly and computes the Prandtl-Meyer function without using any approximation along the way. Figure 3.1 shows some nozzle shapes for Pentane computed with both methods. The contour plots of the inviscid Mach number show that by directly using the Prandtl-Meyer function instead of an averaged isentropic exponent, gives the correct Mach number at the nozzle exit.

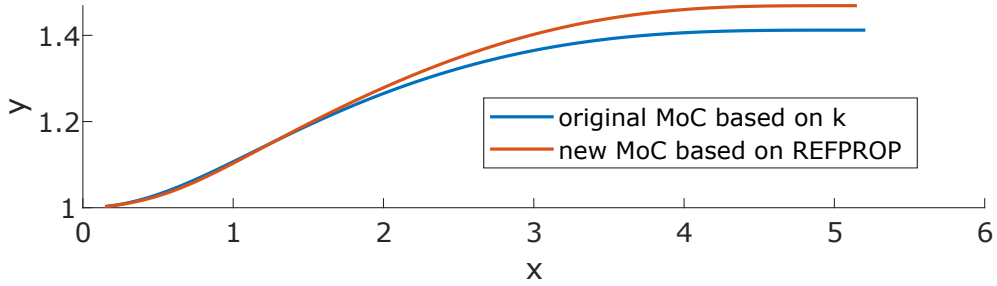

Fig. 3.1 Nozzle shape determined by MoC based on k and REFPROP (Mach 1.6, Pentane: $T_\mathrm{r} = 1.17$ $p_\mathrm{r} = 2.97$)

To assess the real gas effects across multiple Mach numbers including subsonic flow conditions, an additional transonic blade was analysed. The transonic blade considered in this thesis was based on the blade design by the von Karman Institute (Arts et al. (1990)).

To achieve a smooth transition between the subsonic and supersonic geometries, the two different designs were combined. This meant that the supersonic profile, which was based on the design method of Wheeler and Ong (2013) used the same leading-edge as the subsonic/transonic vane (figure 3.2). The latter was taken from the von Karman cascade vane cascade geometry (Arts et al. (1990)). Across all blades, the trailing edge to pitch ratio was set to be constant at 3%. As there is a considerable difference in pressure to either side of the trailing edge, a certain thickness is needed for structural reasons.

3.2 Stage design

Besides the vane calculations, the flow in a full radial stage was analysed as well. The basis of the stage design was the Multall design system developed by Denton (2017). Multall is an open-source turbomachinery design tool published by Denton, which consists of three parts:

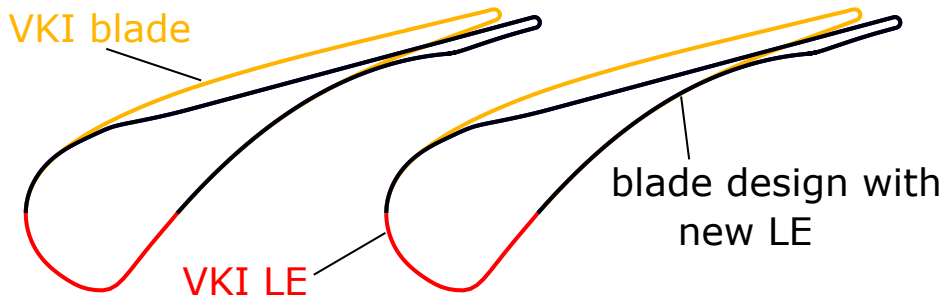

Fig. 3.2 Supersonic vane design with incorporated leading edge

Meangen, Stagen and the 3D CFD solver Multall. While Multall is a CFD solver that can be used to compute performance parameters of the designed stages, Meangen is the initial meanline design tool which is then used as an input to Stagen, which generates the blade profiles.

For the purpose of this thesis, the meanline solver, Meangen, was used in combination with Stagen to generate the blade profiles. To that end, the meanline solver was adapted to include the REFPROP routines throughout all calculations.

Meangen is originally set up to work with a minimum of input variables and provides the user with a 1D solution of the stage. For the design undertaken in this thesis, the meridional coordinates of the mid-span stream surface and the meridional velocity ratio along that curve were provided as input. Furthermore one had to specify the location of the leading and trailing edges, velocity angles at the inlet and outlet of the stator and rotor, rotational speed, guessed efficiency and the inlet conditions (p_0, T_0). On that basis, Meangen would compute the density at each position through the stage, which subsequently is used together with the mass flow to compute the annulus area.

In order to define the blade geometries for the stages that are analysed in this thesis, the vane design by Wheeler and Ong (2013) was combined with the rotor blade design of Stagen by Denton (2017). The variation of the velocity triangles along the span was computed by assuming a free vortex design (rV_θ = constant). The blade design tool was provided with the following input variables: thickness of leading and trailing edge, maximum thickness and point of maximum thickness. Furthermore, the tool was set up to give an almost constant thickness with rounded leading and trailing edges as there are typical for radial machines. In order to reduce the computational cost of the stage calculations, the number of blades in the rotor and the vane were set to be the same (19), and only one passage was meshed.

The aim of the stage design was to provide a feasible design which incorporates the proper equations fo state throughout the design process. Hence it was not intended to find the optimal design for a specific operating point. The design tool could be used to compare

the performance of radial turbines operating with different working fluids at the same non-dimensional parameters. An exemplary stage that was designed with this method can be seen in figure 3.3.

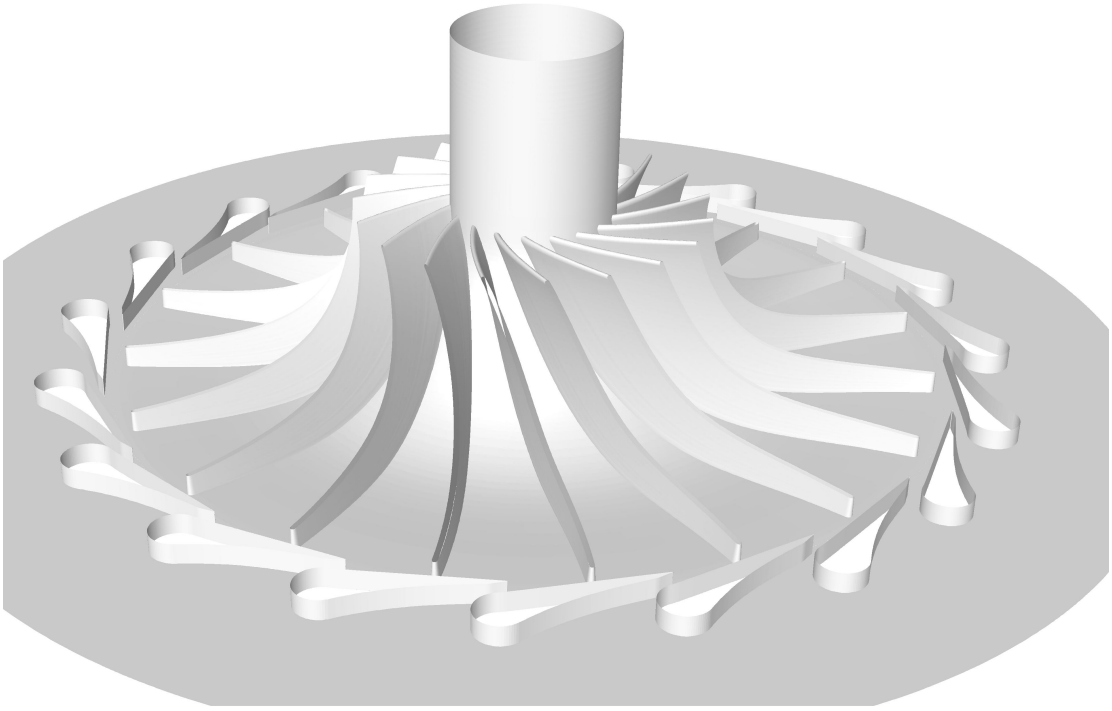

Fig. 3.3 Geometry of an exemplary turbine stage

3.3 Solver settings

All computational simulations were performed in the form of Reynolds Averaged Navier-Stokes (RANS) simulations. The simulations were executed in FLUENT v17.0 (2015) using the density-based implicit solver. In terms of turbulence modelling, the one-equation Spalart-Allmaras model was chosen, as this setting has proven to be in good agreement with comparable experimental data, as shown by Galiana et al. (2016). The wall distance of the first grid point was set in such a way that it yields a y^+ of approximately 30. This meant that wall functions were employed. The difference in loss compared to a simulation performed with a mesh of $y^+ = 1$ and without using any wall functions was found to be less than 0.5%.

Concerning the boundary conditions, the vane inlet was defined as pressure inlet, where the stagnation pressure, temperature and turbulent intensity were defined. The turbulent intensity was set to 5% throughout all computations undertaken in this thesis. The outlet of the domain was set as a pressure outlet such that reflections of pressure waves were prevented. In FLUENT this is achieved through the setting 'strong averaging' on the outlet boundary. For the full stage calculations, the interface of the vane and rotor was set as a sliding mesh interface. As the blade count for the vane and rotor was both 19, only one blade passage was simulated with periodic boundary conditions to either side. At all times the walls were modelled as adiabatic no-slip walls.

The unsteady simulations were performed using a dual-time-stepping algorithm with second-order accuracy. The outer physical time step Δt was set to approximately as many outer time steps per rotor passage as there are cells in the theta direction on the sliding interface ($\approx 250\Delta t/\text{passage}$), as proposed in the FLUENT handbook (Fluent (2016)).

3.4 Meshing

All meshes in this project were created as fully structured multi-block meshes of a single passage with periodic boundary conditions on each side. Specifically, the meshes of the vane (3D and 2D), as well as the rotor meshes used for the unsteady stage calculations, were created with ANSYS Turbogrid.

In terms of overall mesh size for the vane alone calculations, the 3D mesh had $4\text{x}10^6$ elements with $6\text{x}10^4$ on the blade-to-blade plane. Figure 3.4 shows the results of the mesh sensitivity study for the 3D vane mesh, showing that for the chosen mesh the loss is reduced by about 0.11% compared to the $8\text{x}10^6$ elements mesh. The loss is computed as the mixed-out loss at the outlet of the domain (5.1).

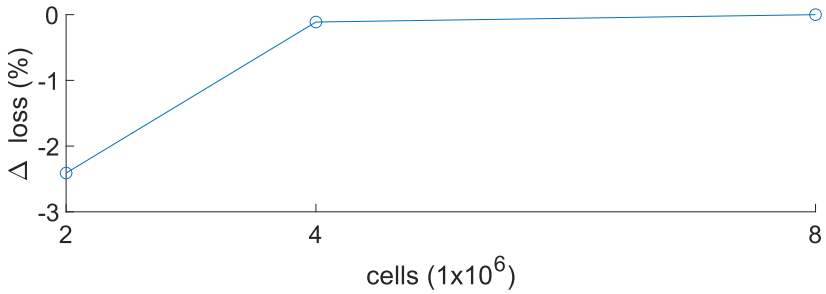

Fig. 3.4 3D grid independence study

The 2D meshes for the vane calculations had 1x10^5 elements, for which an exemplary mesh can be seen if figures 3.5 and 3.6, used for the transonic and supersonic vanes. The results of the mesh sensitivity study for the 2D vane mesh can be seen in figure 3.7, showing that the loss is reduced by about 0.5% for the chosen mesh compared to the mesh with the highest resolution within this sensitivity study.

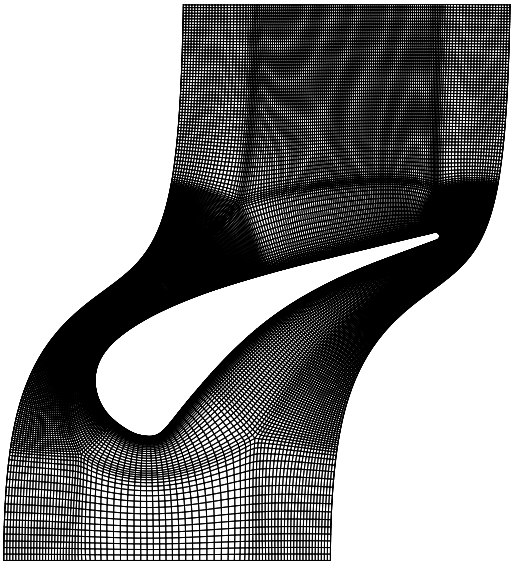

Fig. 3.5 2D Mesh for the transonic vane. Note that only every 2nd mesh line is displayed.

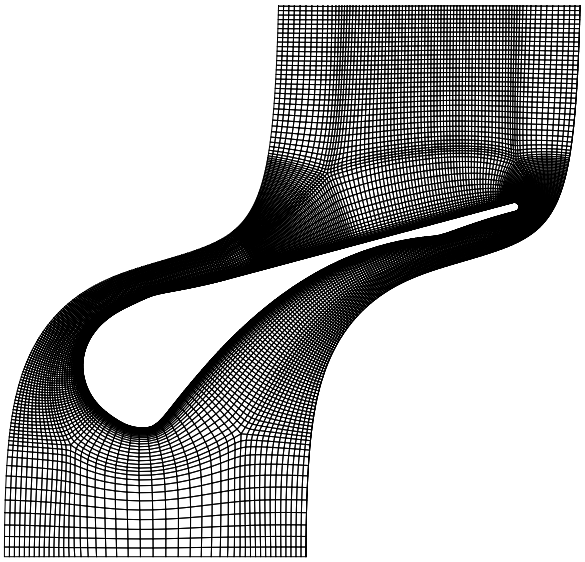

Fig. 3.6 2D Mesh for the supersonic vane. Note that only every 2nd mesh line is displayed.

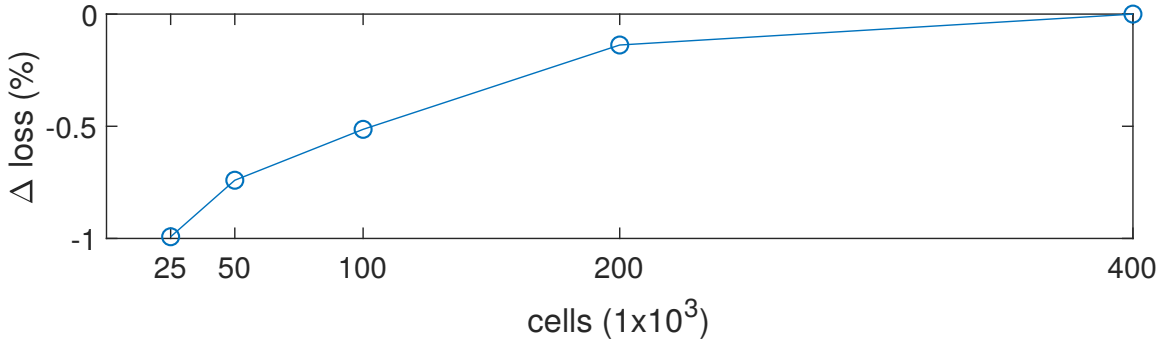

Fig. 3.7 2D grid independence study

Figure 3.8 and 3.9 show the final mesh of the full stage and a more detailed view of the region of the sliding interface, where one can see the meshing of the trailing edge and leading edge. In total, a single passage mesh consisting of vane and rotor has about 4x10^6 cells, whereby there were 60 cells in the span-wise direction.

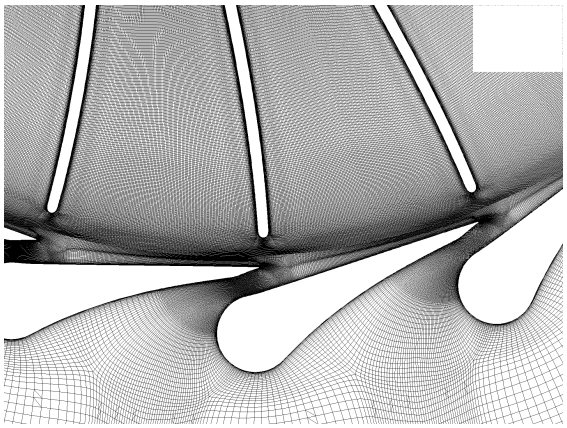

Fig. 3.8 Mesh of stage showing vane and rotor leading edge

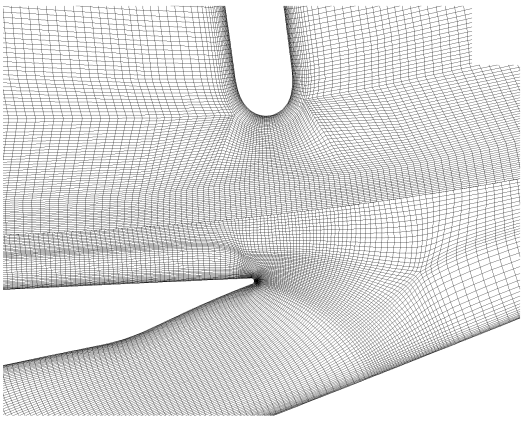

Fig. 3.9 Mesh of stage showing detailed view of vane trailing edge and rotor leading edge

3.5 Real gas model

As the purpose of this thesis is to see how k, Γ and Z impact the aerodynamics of turbines, it is vital to accurately compute the thermodynamic properties of the fluids at all times.

Within the context of this project, all real gas properties are computed with REFPROP, as both ANSYS FLUENT and Matlab have the ability to access the routines directly. To reduce the computational cost of the CFD, high-resolution look-up tables of the properties of each fluid were generated within ANSYS FLUENT. The dimensions of the look-up tables on the pressure-temperature plane were set to 2000x2000. This resolution was significantly higher than the minimum resolution needed to achieve the same results as without the look-up tables.

Chapter 4

Experimental validation of computational methods

Within this chapter, the experimental results are presented. First, the wall static pressure measurements taken for the first set of experiments with argon, air, CO_2 and R134a (table 2.3) are presented. Second, the results of the second set of experiments are discussed which include the wake measurements for air, CO_2 and R134a (table 2.4).

4.1 Wall static pressure

The pressures are taken over multiple consecutive runs while changing the circumferential position of the pressure measurements. The scattered data is then interpolated to obtain the contour plots of isentropic Mach number (see figure 4.1). Detailed experimental data of various fluids within a transonic cascade have previously not been available, especially with fluids like R134a. Therefore, besides analysing the differences between the measured flow fields, it is of particular interest to see if these differences in the gas dynamics are correctly predicted with the chosen computational method. Validating the selected computational method will give the confidence to proceed with a detailed analysis of how the real gas parameters impact performance.

Looking at Mach number contours of the first set of experiments, one can see two differences between the working fluids. First of all, the Mach number obtained within the nozzle is slightly increasing with rising k. This can easily be explained by the previously stated 1D effect that k has on the aerodynamics, saying that lower values of k will need a bigger area change to expands to the same Mach number. In the case of the experiment, the geometry was constant for all four fluids that were analysed. Thus, one can expect a

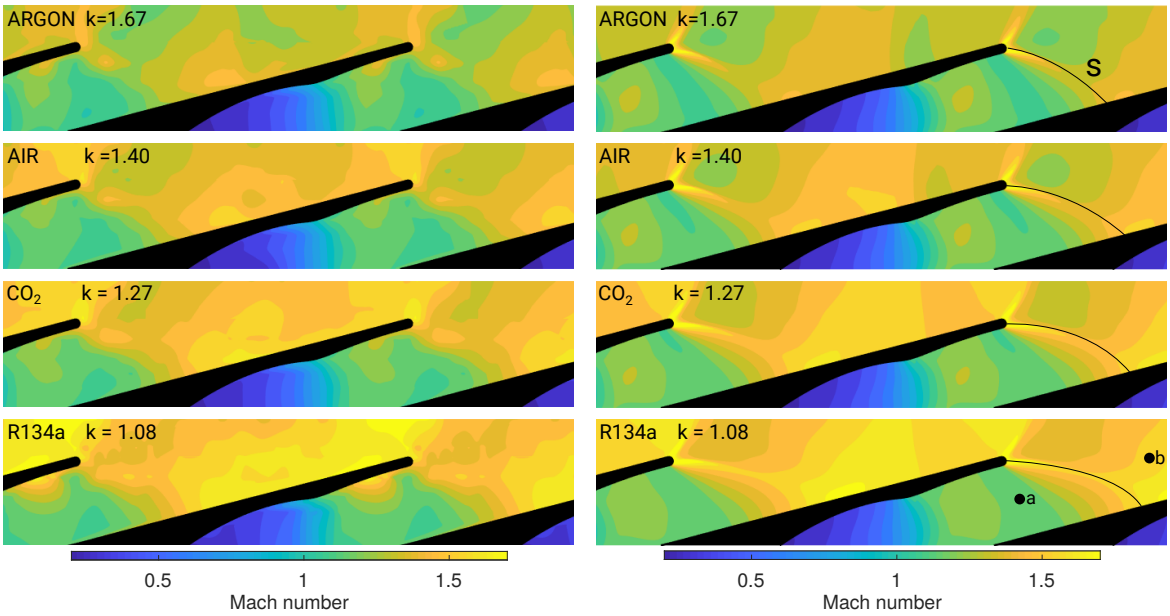

Fig. 4.1 Isentropic Mach number distributions for argon, air, CO_2 and R134a (experiment on the left, CFD on the right)

higher Mach number at the nozzle exit for argon ($k = 1.67$) and lower Mach number for R134a ($k = 1.10$). The second difference between the four working fluids that can be noticed in figure 4.1 is the difference in the suction side Mach number. The differences between the gases are significantly more prominent than the previous effect. As the value of k was reduced from 1.67 to 1.08 (i.e. between argon and R134a), the results indicate an increase of Mach number at the suction surface side of the trailing edge (see figure 4.1). This is in agreement with the work of Galiana et al. (2016) which demonstrated that lower values of k led to a higher supersonic turning due to an increased Prandtl-Meyer function, which is the previously discussed 2D effect of k on turbine aerodynamics.

To see if the CFD correctly predicts these effects, the same contour plots of isentropic Mach number are extracted from the CFD simulation done with the same fluids and same inlet conditions. Looking at those contours (see figure 4.1) it appears as the predictions of the CFD are in line with the experimental findings. The shift of the shock position with k (labelled S) is predicted as well as the greater expansion along the suction side of the vane for lower values of the isentropic exponent.

Another way of highlighting the impact of the isentropic exponent on the aerodynamics and at the same time to highlight the agreement between computational and experimental data is to look at the centre-line Mach number distribution (see figure 4.2). The figure shows that in the diverging section of the nozzle, upstream of 'a', the flow is initially accelerated in

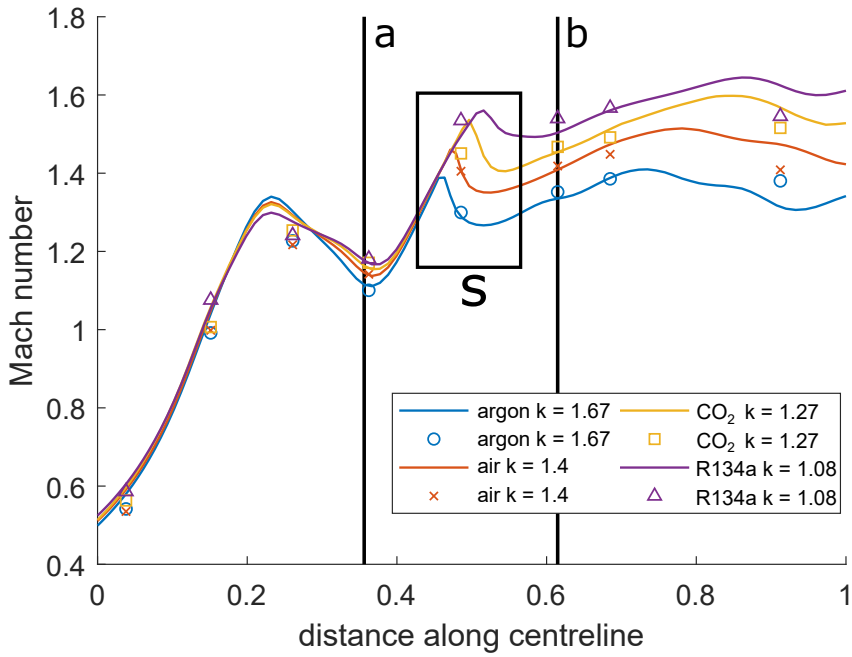

Fig. 4.2 Centre-line Mach number distribution with stream-wise positions at the (a) nozzle exit and (b) suction surface trailing edge (lines: CFD, symbols: experiment)

an almost identical pattern for all four fluids. Furthermore, the peak isentropic Mach number, which is reached at a distance of around 50% on the centre-line (labelled S), is reduced as the isentropic exponent is increased. Both the computational and experimental results show good agreements of this trend as well as for the flow downstream of the compression wave (labelled 'b').

One area of the flow that is always of particular interest is the trailing edge region. The base pressure, according to the work of Denton and Xu (1990), is directly linked to the trailing edge loss. To that end, the pressure along the circumferential position of the trailing edge is extracted from the experimental data. Figure 4.3 shows the isentropic Mach number along that circumferential line for the case of argon and R134a, the solid lines are the predictions of the CFD, and the dots represent the experimental data points. As with the contour plots, it appears that the CFD is correctly predicting the base pressure for the fluids tested here.

The experimental results of the first set of experiments showed good agreement with the CFD predictions. This gives confidence in the computational approach when variations in isentropic exponent k are analysed. In order to further validate the computational method for fluids of varying compressibility factor Z, a second set of experiments was conducted. At the point in time, when the experiments were conducted, the ambient temperature was

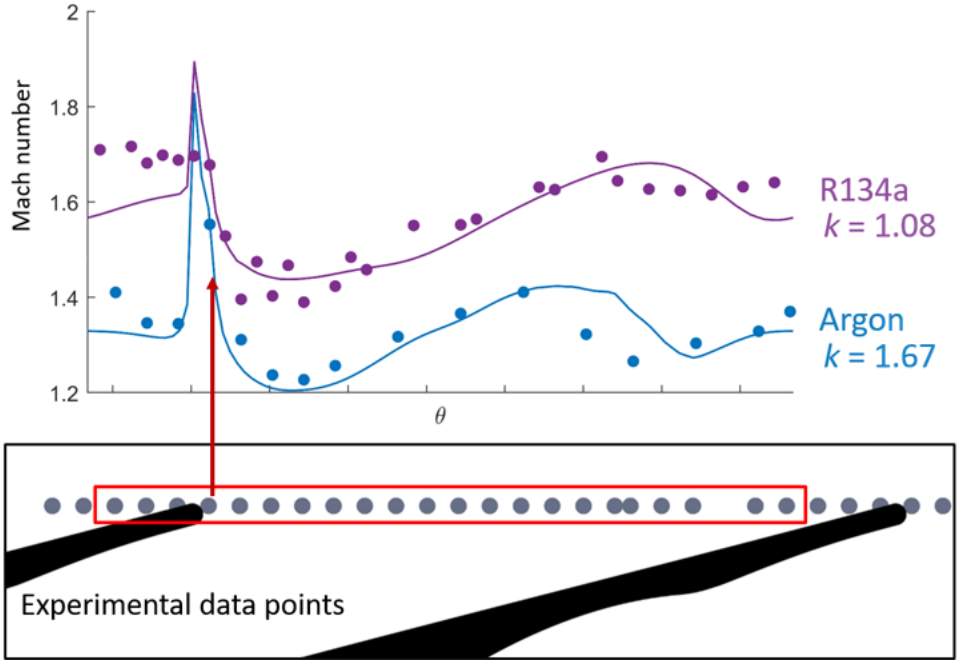

Fig. 4.3 Isentropic Mach number at the axial position of the trailing edge. Argon and R134a. (lines: CFD, symbols: experiment)

at 20°or 293K. This change in inlet temperature led to a reduction in compressibility factor of R134a. The new lower compressibility factor was $Z = 0.88$ compared to $Z = 0.96$ at the warmer conditions of the first set of experiments.

Figure 4.4 shows the experimental data along the centre-line in comparison to the CFD predictions. It shows that there is a good agreement between the CFD and the experimental data. The peak between the nozzle and the trailing edge plane is the result of the expansion fan that forms on the pressure side of the trailing edge and the consecutive compression shock. In this region, the predictions of the CFD match the experimental data very well, which gives confidence that the CFD correctly predicts the flow around the trailing edge.

Again the isentropic Mach number is extracted at the axial position of the trailing edge as shown in figure 4.5. As with the centre-line, there is a good agreement between the experiment and the CFD predictions. To the left side of the trailing edge, the CFD predicts a slightly lower isentropic Mach number. This discrepancy is most likely the result of CFD's inability to correctly predict the shock-boundary layer interaction along the suction side of the blade. This is expected due to the employed wall functions and will be further discussed in the following section.

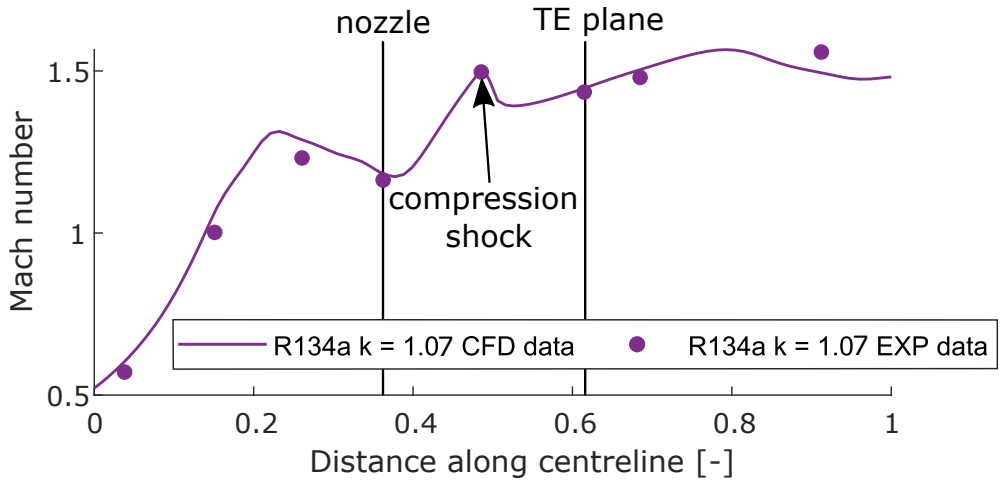

Fig. 4.4 Centre-line Mach number distribution for R134a at $Z = 0.88$ (lines: CFD, symbols: experiment)

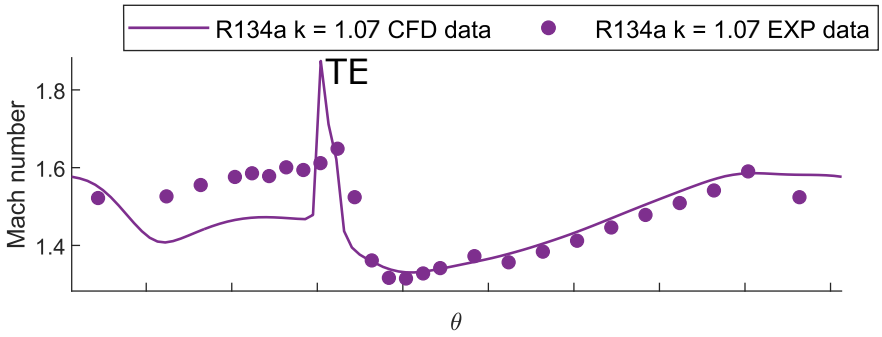

Fig. 4.5 Isentropic Mach number at the axial position of the trailing edge for R134a at $Z = 0.88$ (lines: CFD, symbols: experiment)

4.2 Wake measurements

In the second set of experiments, an additional total pressure wedge probe was used to perform wake measurements downstream of the trailing edge. As stated before, the trailing edge region is of particular interest, which is why the wake measurements will be of high interest.

While the actual wake traverse was conducted with a fixed yaw angle of the probe, prior to each traverse, a free stream calibration was done for each fluid. This was done by rotating the probe until the total pressure reading was maximised, thus ensuring the probe was aligned with the flow.

As the total pressure probe is measuring within the supersonic region of the flow, a bow shock will form upstream of it. Therefore, the probe will measure stagnation pressure that is subject to some shock loss. As the Mach number upstream of the probe is not measured,

correcting the measured stagnation pressure becomes challenging. As a result, one cannot make a direct comparison between the three fluids, as the shock loss will be different for all three fluids.

While it is difficult to make any conclusion based on the comparison of the raw pressure measurements, one can compare them to CFD simulations to see if there are relevant differences between the fluids that the experiment can pick up. The location of the traverse relative to the vane is shown on the contour plot of Mach number for the example of air (see figure 4.6). The traverse of the probe passes through three locations of particular interest.

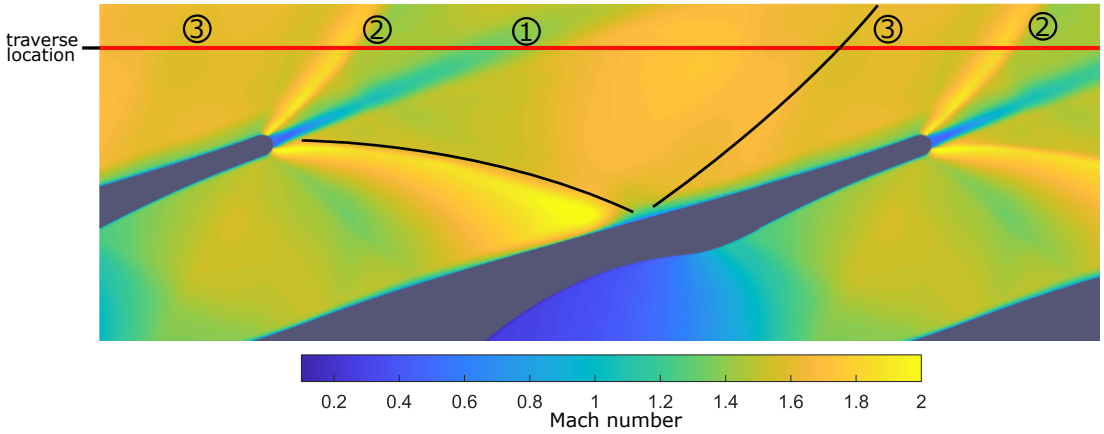

Fig. 4.6 Mach number contours at mid-span showing the location of the wake traverse

The first position (1) is the wake itself, the second position (2) is the oblique shock that forms on the suction side of the trailing edge and the third position (3) is the reflection of the oblique shock that forms on the pressure side of the trailing edge.

The CFD solutions do allow to extract the Mach number at the position of the probe, which can be used together with the REFPROP equations of state to compute the theoretical post-shock flow properties (see the middle of figure 4.7). This remains an approximation, as the probe is not located in a uniform flow field but rather in a complex 3D flow field where a bow shock is formed.

An additional challenge of the wake traverse was the small scale of the cascade and thus the small scale of the flow features such as the wake. In order to highlight the changes in the flow properties in the close proximity to the centre of the face of the probe, the minimum and maximum values around this point were extracted from the CFD. This was done by extracting the min/max values on a sphere around this point with a radius of 0.2 mm, equal to the inside diameter of the hypodermic tube parallel to the flow (see figure 2.10). The extent of the flow properties is shown as the shaded area in figure 4.7.

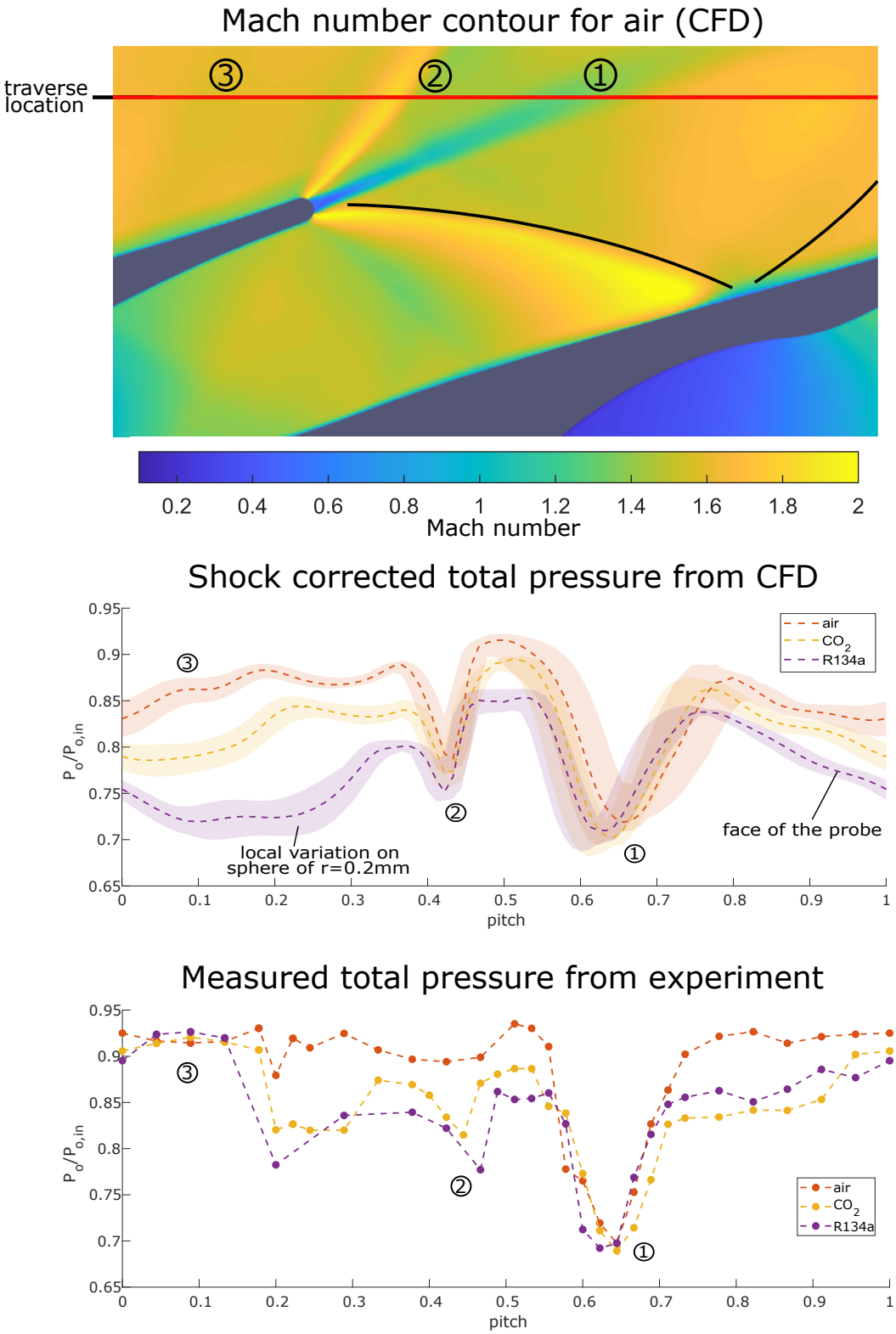

Fig. 4.7 Comparison of wakes extracted from CFD to experimental measurements

The wake profile for the three fluids, with the measured stagnation pressure, are shown on the bottom of figure 4.7. For all three fluids, the probe is able to pick up the wake downstream of the cascade with about ten measurements (1° increments) inside the wake. At the centre of the wake, the measured total pressure reads about 0.69 $p_{0,in}$. Looking at the free stream, air shows the highest measured total pressure between the three measured fluids. There are two possible reasons for this. Either a different Mach number in the free stream leads to higher shock losses and/or higher shock loss due to k at the same Mach number (this will be discussed in more detail in the following chapter). The detailed wall static measurements for the different fluids did reveal that the unguided expansion for R134a (low k) is higher, and one can observe higher Mach numbers. Hence, one can expect the Mach number at the mid-span to behave similarly.

Looking at the shock corrected computational results at the location of the wake traverse (see the middle of figure 4.7) shows a good agreement with the experimental data in the region of the wake. Especially the trend of the depth and the width of the wakes are in good agreement between the CFD and the experiment.

Also, the dip to the left side of the wake (position (2)) shows the same trend in the CFD solution as the experimental findings. This dip is the result of the expansion fan and compression that forms on the suction side of the trailing edge. At this point, the probe sees a higher Mach number and thus a stronger bow shock is formed. The observed dip in measured pressure is increasing for lower values of k due to more substantial shock losses.

At the same time, there are also differences between the results of the CFD and the measured data. This is the case for the free stream (position (3)). One likely reason for this discrepancy between CFD and experimental data is that the CFD is not able to correctly predict the shock boundary layer interaction at the position where the pressure side shock is reflected of the suction side of the neighbouring blade, which then sets the size of the shear layer bubble, which in turn affects the Mach number in the free stream. This is to be expected as the simulations were set up to employ wall functions.

4.3 Summary

Comparing the experimental measurements to the predictions of the applied computational method has shown that the CFD is able to capture the salient effects of the isentropic exponent k on the gas dynamics within the vane. The detailed wall static measurements show a reduced Mach number within nozzle for the fluid of low k, while the Mach number along the suction side of the vane is increasing with low values of k. There is also a good agreement between

the CFD and the experimental data on the trailing edge plane, which is particularly important for correctly predicting the loss. An additional case of reduced compressibility factor Z also shows good agreement with the experimental findings.

Additional wake measurements were undertaken for air, CO_2 and R134a. Again the CFD is good agreement with the experimental findings, especially right in the wake region. Some discrepancies between the CFD and the experimental data were observed in the free-stream, as the CFD (using wall functions) is not able to correctly predict the shock boundary layer interaction.

The current run conditions do not yet allow to compare any differences in loss, as one has to design a blade for each fluid to match the loading independent of k. Based on this validation, one can now assess the impact k has on the loss at matched operating conditions, as discussed next.

Chapter 5

The effect of isentropic exponent k on vane performance

This chapter aims to assess how the performance of a turbine is affected by the isentropic exponent. The previous chapter showed the variation of the supersonic flow field for different working fluids, while the geometry remained fixed. In order to make a fair comparison of the overall loss that is observed at the vane exit, the vane design has to be adapted to each fluid in such a way that one achieves a uniform exit Mach number across all fluids. Therefore, a series of vanes has been designed, whereby the diverging nozzle section was designed to produce the desired Mach number for a specific isentropic exponent. The exit Mach numbers ranged from subsonic conditions up to Mach 1.80. For the example of argon ($k = 1.67$) and R134a ($k = 1.08$) some blade geometries are shown in figure 5.1.

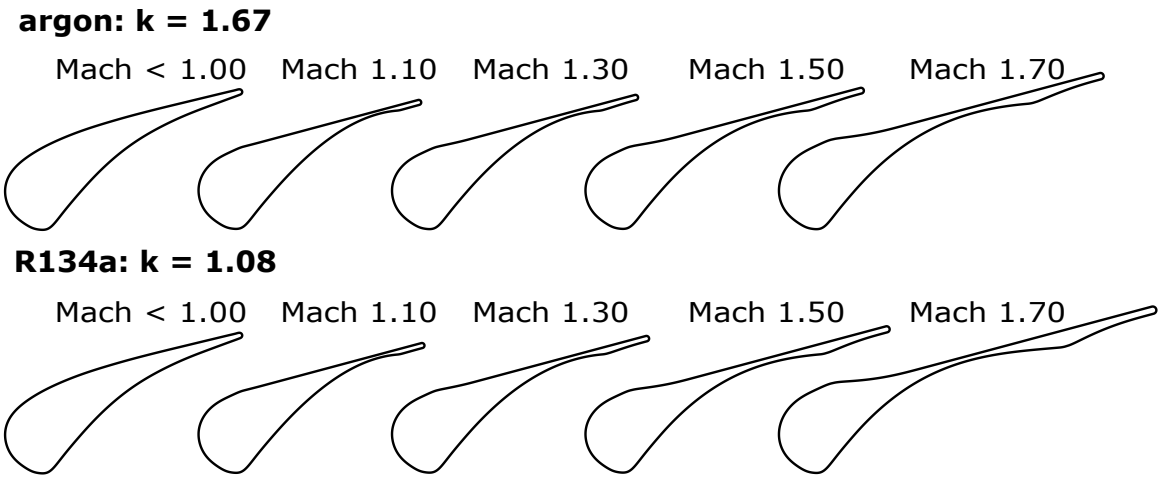

Fig. 5.1 Vane design for transonic and supersonic design space (e.g. argon $k = 1.67$ and R134a $k = 1.08$)

One can see, especially for the higher Mach numbers, that the length of the nozzle is increasing for the case of lower k. Some exemplary Mach number distributions for argon and R134a are shown in figure 5.2, confirming that the adaptive blade design is indeed capable of producing similar Mach number distributions for different fluids.

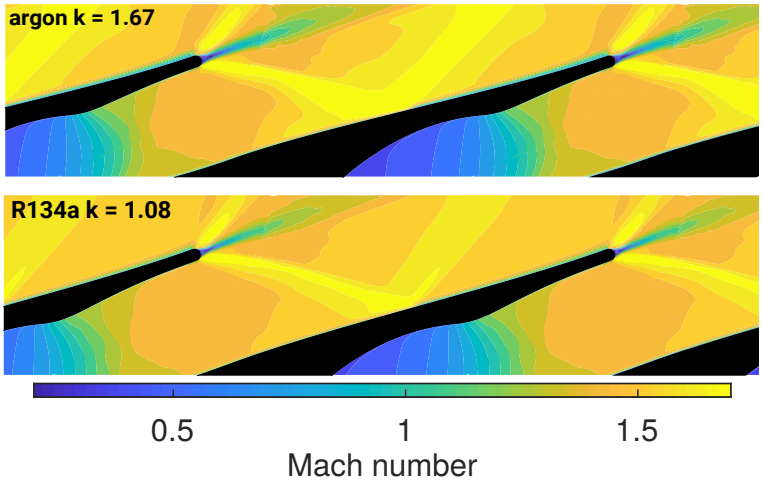

Fig. 5.2 Mach number distribution for argon and R134a with redesigned vanes (e.g. $M = 1.45$)

While for the supersonic Mach numbers, there were different vanes for every increment of Mach 0.1, all the subsonic cases were simulated with one fixed blade geometry. For all blade geometries, a range of different operating conditions was analysed, whereby the pressure ratio across the vane was varied. This meant that each vane would operate in a range of different exit Mach numbers in the proximity of its design Mach number ($\pm$ Mach 0.1). The transonic vane was the exception as this was operated over a larger range (Mach 0.3-1.1). At the same time, the inlet total pressure was adapted in such a way that the Reynolds number at the vane exit was constant across all cases ($1.7\text{x}10^6$). This meant that any effects that Reynolds number might have on loss were to be ignored.

5.1 Loss analysis

To compute the total loss coefficient of the vane, the local difference between enthalpy and isentropic enthalpy was used:

$$\zeta_{\text{out}} = \frac{h_2 - h_{2\text{s}}}{h_0 - h_{2\text{s}}} \tag{5.1}$$

where h_{s} represents the enthalpy that one would obtain if the fluid was to be expanded isentropically to the final pressure p_2. This final pressure p_2 as well as the enthalpy h_2 at the outlet were obtained by computing the mixed-out state at the outlet plane. The mixed-out

state was computed as a constant area mixing calculation that conserves mass omentum and energy. An exemplary expansion process for CO_2 is shown in figure 5.3, with the highlighted vane loss.

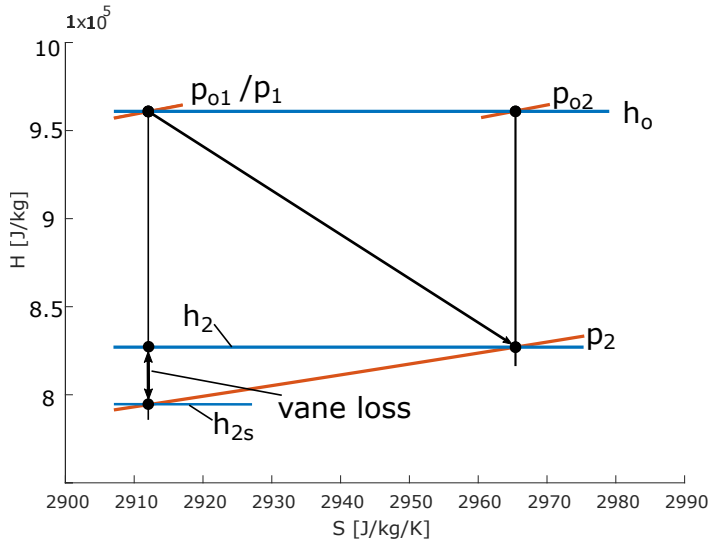

Fig. 5.3 Expansion process of CO_2 on enthalpy-entropy plot showing the vane loss

The resulting total loss for the four different working fluids can be seen in figure 5.4, showing the mixed-out loss over a range of Mach numbers.

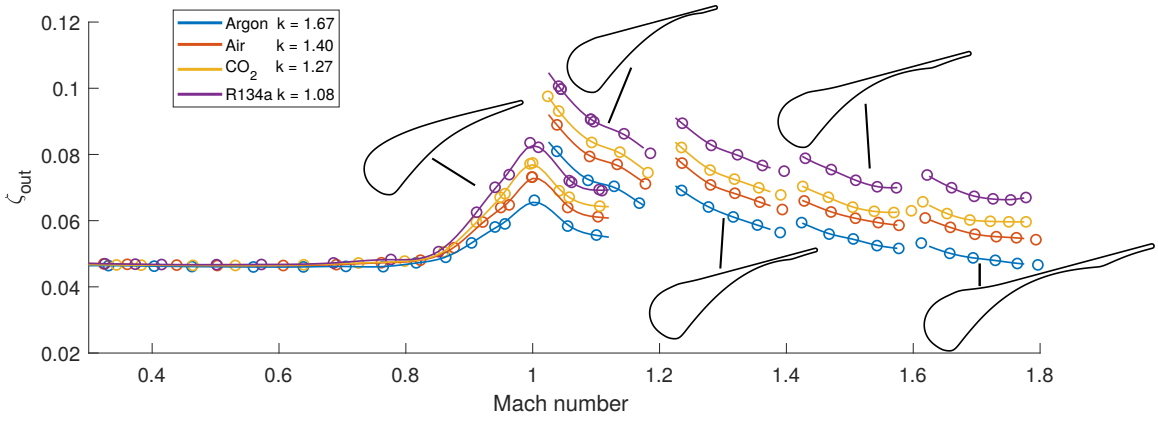

Fig. 5.4 Mixed-out loss coefficient from 2D CFD at $Re = 1.7\text{x}10^6$

First, looking at the loss for the transonic blade, there is no difference in total loss as long as the exit Mach number remains lower than 0.8. This behaviour is to be expected as for low Mach numbers, the effects of compressibility within the cascade are reduced as well. For exit Mach numbers greater than 0.8, this is not the case any more. Here, the loss ζ_{out}, scales both with the isentropic exponent and with exit Mach number. Specifically, low values of k

lead to higher total losses. To give an example, at Mach 1.0 at the vane exit, ζ_{out} deviates by +13% and -9% relative to the case of air for R134a and argon respectively. These sonic exit conditions are also the operating point of the transonic vane with the highest overall losses, which can be explained by the formation of a normal shock on the suction side of the blade. At higher pressure ratios that yield exit Mach numbers beyond sonic conditions, an oblique shock is formed at the trailing edge, which results in slightly lower losses than the normal shock. The harmful effect of this shock structure on ζ_{out} is higher for fluids with lower values of k.

Secondly, looking at all the supersonic blades, one can observe the same dependency of total loss on k, meaning that while for higher k loss is reduced and for low values of k, loss is increased. Again to give an example, at a design exit Mach number of 1.3, the mixed-out loss for R134a ($k = 1.08$) is 16.5% greater than that of air. For argon ($k = 1.67$), at the same vane exit Mach number ζ_{out} shows a 10.5% reduction compared to the air case.

For every individual vane with a specific design Mach number, the total loss is decreasing with operating Mach number rising beyond their design Mach number. This behaviour can be explained by looking at the shock structure at the trailing edge. If a vane operates at a lower pressure ratio and thus lower Mach number than its design Mach number, the shock at the trailing edge becomes less oblique, which causes a higher shock loss. For pressure ratios higher than the design PR, the opposite is the case. Here the shock becomes more oblique, which reduces the Mach number normal to the shock and thus the shock losses that are occurring. Even at these off-design operating conditions, the overall loss remains highly dependent on k.

In conclusion, it can be said that for any turbine operating at a Mach number beyond 0.8, the effect k has on the total loss, has to be considered at all times. The origin of the differences in loss at those high exit Mach numbers will be subject of the following sections.

5.1.1 Loss breakdown

The preceding section showed in detail how the overall loss varies for different fluids across different Mach numbers. This section aims to identify the flow physics that are responsible for the difference in loss due to k. Therefore, a control volume has been designed that divided the overall loss into two sections: passage loss upstream of the trailing edge and mixing loss that occurs downstream of the trailing edge. The chosen control volume is shown in figure 5.5 and it was defined in such a way that the separated base region and the shocks at the trailing edge were part of the downstream volume.

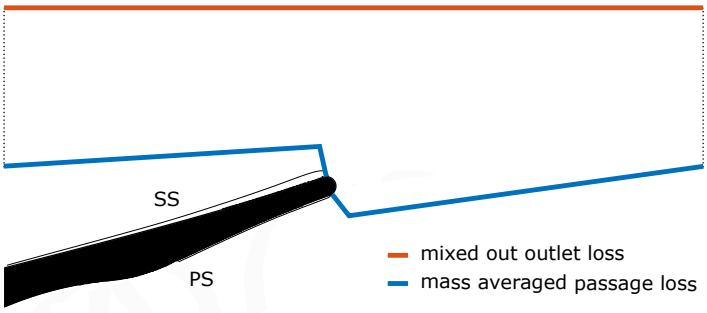

Fig. 5.5 Control volume to define loss coefficient split

The mass flow average properties at the trailing edge plane were computed by integration of along the blue line in figure 5.5, which were then used to compute the passage loss coefficient that is defined as the loss at the outlet (equation 5.1).

The loss coefficient associated with the trailing edge (ζ_{te}) was defined as the difference between the mixed-out loss at the outlet (ζ_{out}) and $\zeta_{passage}$.

$$\zeta_{te} = \zeta_{out} - \zeta_{passage} \tag{5.2}$$

This breakdown of the loss was conducted for argon and R134a, for which the results can be seen in figure 5.6. Here, for the supersonic vanes, the loss coefficients were only regarded at their respective design Mach numbers. For Mach numbers higher than 0.8 the trailing edge loss increases rapidly till in peaks around sonic conditions. The passage loss, on the other hand, remains relatively constant across the entire Mach number range. Again it can be noted that the magnitude of the trailing edge loss is higher for R134a with the lower value of k. Similarly, the passage loss is also higher for the fluid of low k. To give an example, at a Mach number of 1.5 the difference in the loss coefficient is 27% for $\zeta_{passage}$ and 38% for ζ_{te} for the fluids with $k = 1.67$ and $k = 1.08$.

There are two flow features in the passage that can lead to the observed difference: viscous losses of the boundary layer and shock losses. In order to quantify the differences in shock loss, a local shock loss coefficient was extracted from the centre-line of the nozzle. The shock loss coefficient was defined similarly to equation 5.1, where h_2 was based on the pressure downstream of the shock and h_{2s} assumes an isentropic pressure rise across the shock. For an exit Mach number of 1.5, figure 5.7 shows the rise in entropy across the oblique shock that arises in the free stream of the vane. For R134a, this shock loss coefficient is 25% higher than the shock loss that occurs for air. The passage loss for R134a at the same exit Mach number (shown in figure 5.6) is 15% higher than the one of air. Hence, once can

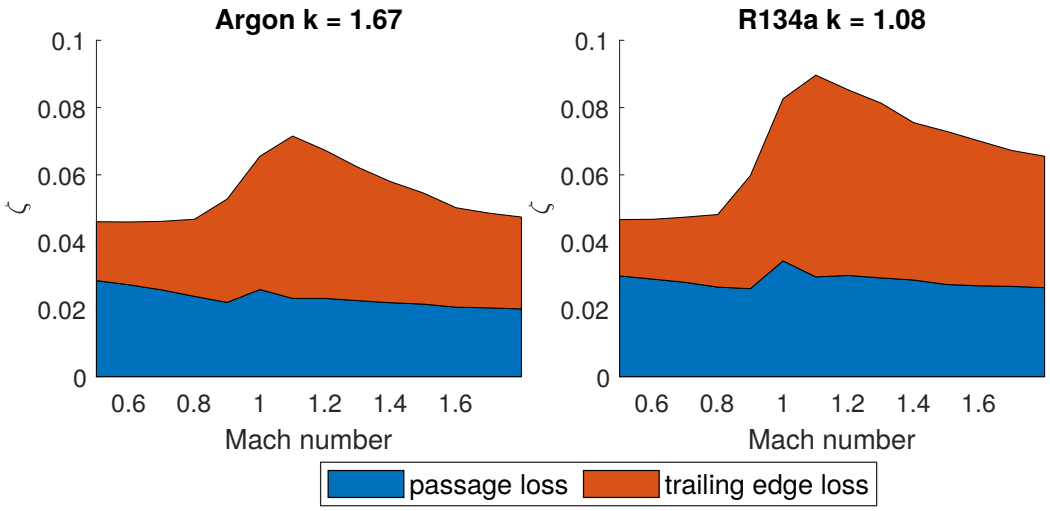

Fig. 5.6 Loss breakdown against design Mach number for argon and R134a at $Re = 1.7\text{x}10^6$

make the assumption that this difference in passage loss coefficient is primarily driven by changes in shock loss which are a function of the isentropic exponent.

Staff (1953) proposed a relation that can be used to compute the entropy increase over a normal shock. This relation can be used to derive the shock loss coefficient for a perfect gas (5.3).

$$\left(\frac{T\Delta s}{\frac{1}{2}V^2}\right)_{\text{shock}} \approx \frac{2}{3}\cdot\frac{1}{(k+1)^2}\cdot\frac{(M_1-1)^3}{M_2^2} \tag{5.3}$$

To apply the above equation to an oblique shock, one has to use Mach numbers (M_1 and M_2) normal to the shock front. Under the assumption of a theoretically fixed drop of Mach number for all values of isentropic exponent, the equation simplifies to $\zeta_{\text{shock}} \propto \frac{1}{(k+1)^2}$. This reduced relationship is plotted as a dotted line in figure 5.7. The overall trend by this simplified analysis of greater shock losses for reduced values of k is in broad agreement with the loss coefficient that was extracted from the CFD cases. The results have indicated the difference in passage loss for different k has mainly driven by the difference is shock loss due to k. Looking at the overall loss of the vane though, the passage loss only represents a fraction of about 38%. Hence, the trailing edge loss is the much bigger contributor to the overall loss, which will be subject of the discussion in the following section.

5.2 The effect of isentropic exponent k on trailing edge loss

The previous segments showed that the predominant loss mechanism for supersonic turbine vanes happens downstream of the trailing edge. To additionally examine this loss mechanism,

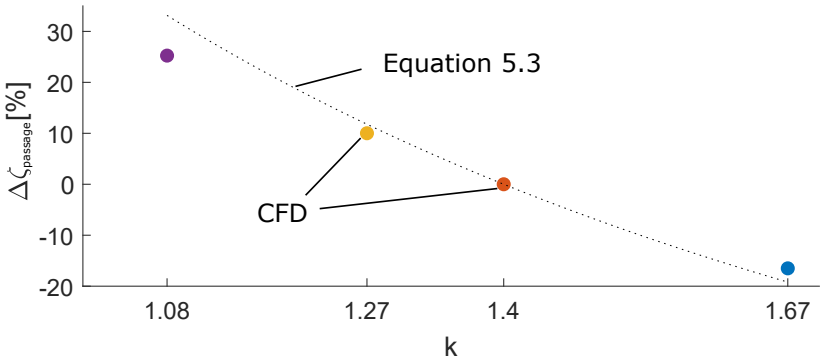

Fig. 5.7 Oblique shock loss variation for supersonic vane at $M_{out} = 1.5$ at the nozzle centre-line

this section contains a detailed examination of the trailing edge losses. To that end, a 1D trailing edge loss model will be used to give an estimate on how the isentropic exponent influences the trailing edge loss. This analytical model is based on the approach of Denton and Xu (1990) and employs conservation of mass, momentum and energy under the assumption of isentropic and choked flow. The investigation introduced by Denton & Xu was conducted for air. Furthermore, this approach has been used by Durá Galiana et al. (2017) to examine the trailing edge losses of real gas flows downstream of a vane trailing edge. Therefore the proper equations of state by REFPROP were used. The 1D analysis that follows is using a very similar approach based on the previously studied fluids and geometries.

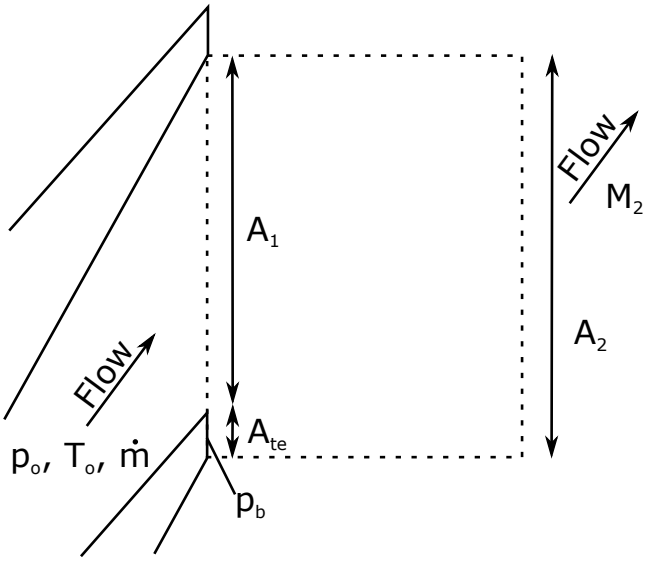

Fig. 5.8 Control volume for 1D mixing calculation

The control volume above (figure 5.8) is used to compute the trailing edge loss. At the inlet of the domain the flow is assumed to be uniform, defined by the total pressure p_0, total temperature T_0 and mass flow at a certain velocity angle. Additionally, the base pressure p_b of the trailing edge, as well as the trailing edge blockage A_te, are defined. At the outlet domain, one has to define the flow area A_2 and the mixed-out Mach number at the outflow.

It is assumed that there is no tangential loading at the trailing edge. Hence, for the following mixing calculation a constant tangential velocity is assumed throughout the control volume ($V_\mathrm{t} = V_\mathrm{t1} = V_\mathrm{t2}$). This yields the following set of equations for conservation of mass, momentum and energy:

$$\rho_1 V_\mathrm{x1} A_1 = \rho_2 V_\mathrm{x2} A_2 \tag{5.4}$$

$$A_1(\rho_1 V_\mathrm{x1}^2 + p_1) + p_\mathrm{b} A_\mathrm{te} = A_2(\rho_2 V_\mathrm{x2}^2 + p_2) \tag{5.5}$$

$$h_0 = h_1 + \frac{1}{2}V_\mathrm{x1}^2 + \frac{1}{2}V_\mathrm{t}^2 = h_2 + \frac{1}{2}V_\mathrm{x2}^2 + \frac{1}{2}V_\mathrm{t}^2 \tag{5.6}$$

Solving these equations, while using the REFPROP routines as equations of state, yields the uniform mixed-out state that will develop downstream of the trailing edge. The loss coefficient of the trailing edge loss is defined similar to the outlet mix (equation 5.1):

$$\zeta_\mathrm{te} = \frac{h_2 - h_{2\mathrm{s}}}{h_0 - h_{2\mathrm{s}}} \tag{5.7}$$

To see how this simplified 1D loss compares against the trailing edge loss of the CFD, the base pressure and trailing edge blockage were extracted from the CFD. The trailing edge blockage was obtained by using the mass-weighted averaged density and axial velocity at the trailing edge plane and applying conservation of mass. The different loss coefficients obtained through the 1D model and the CFD are shown in figure 5.9. While the magnitude of the loss is differing between the two different approaches, the 1D loss model is able to capture quite well the relative change in loss between the various fluids due to k.

For the purpose of this analysis, the described 1D model was solved for an array of possible combinations between base pressure p_b and trailing edge blockage A_te. In a subsequent step, lines of constant trailing edge blockage were extracted from the contour maps of loss. A_te was kept constant for each fluid at the extracted value from the CFD simulation yielding the change in trailing edge loss with base pressure for each fluid. The extracted lines of loss for a vane exit Mach number of 1.3 can be seen in figure 5.10. Additionally, the base pressure form the CFD simulations were extracted for the four fluids and are shown as circles in the same plot. The base pressure represents the average pressure on the trailing edge within

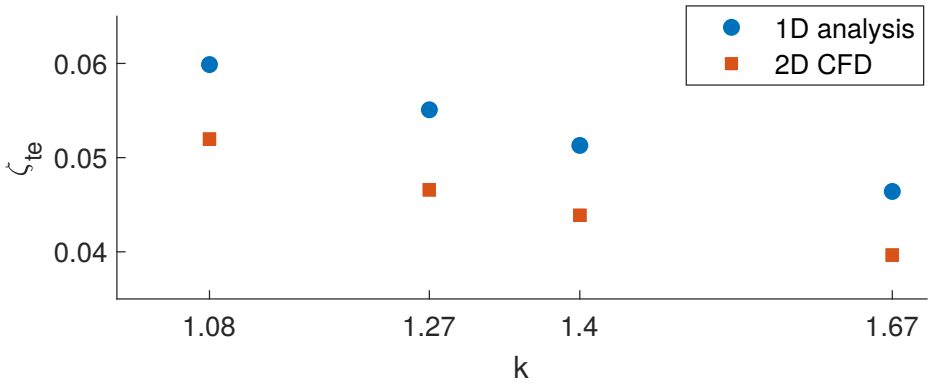

Fig. 5.9 Trailing edge loss from 1D analysis and 2D CFD

the base region. First of all the figure shows that the base pressure is a strong function of k, whereby the base pressure is increased for fluids of low k. Secondly, even with this shift in base pressure, the fluids with smaller isentropic exponent show a more significant trailing edge loss than the fluids of high k.

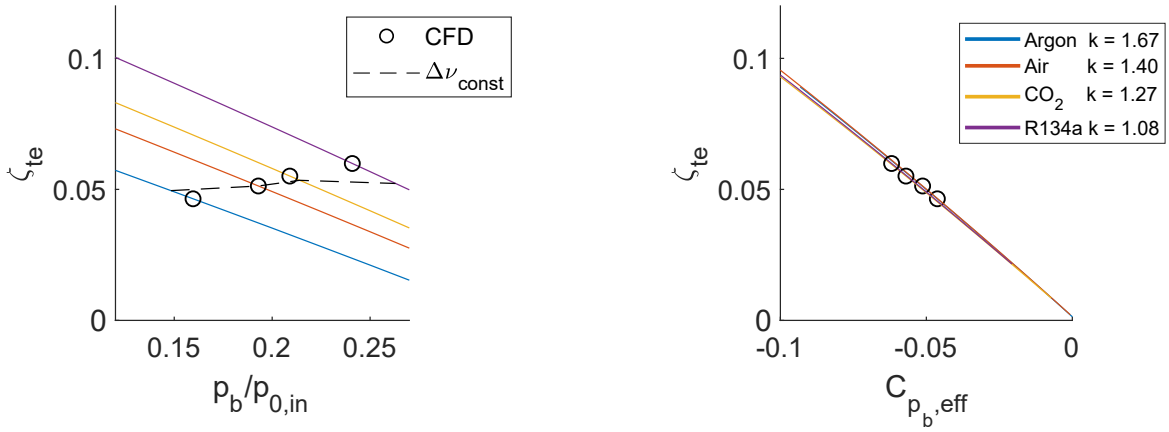

Fig. 5.10 Trailing edge loss from 1D analysis; circles denote base pressure extracted from CFD (Mach 1.30)

To see where these differences in base pressure originate, one has to look at the flow structure around the trailing edge. A simplified schematic view of such a flow structure is shown in figure 5.11. Recalling the 2D effect that k has on the gas dynamics of a fluid, the turning angle around the trailing edge is increased for fluids of lower k. This results in a reduction of the base region, as it can be seen for the example of argon and R134a in Mach number distributions in figure 5.11. These findings are in agreement with the previous studies on trailing edge flow by Galiana et al. (2016).

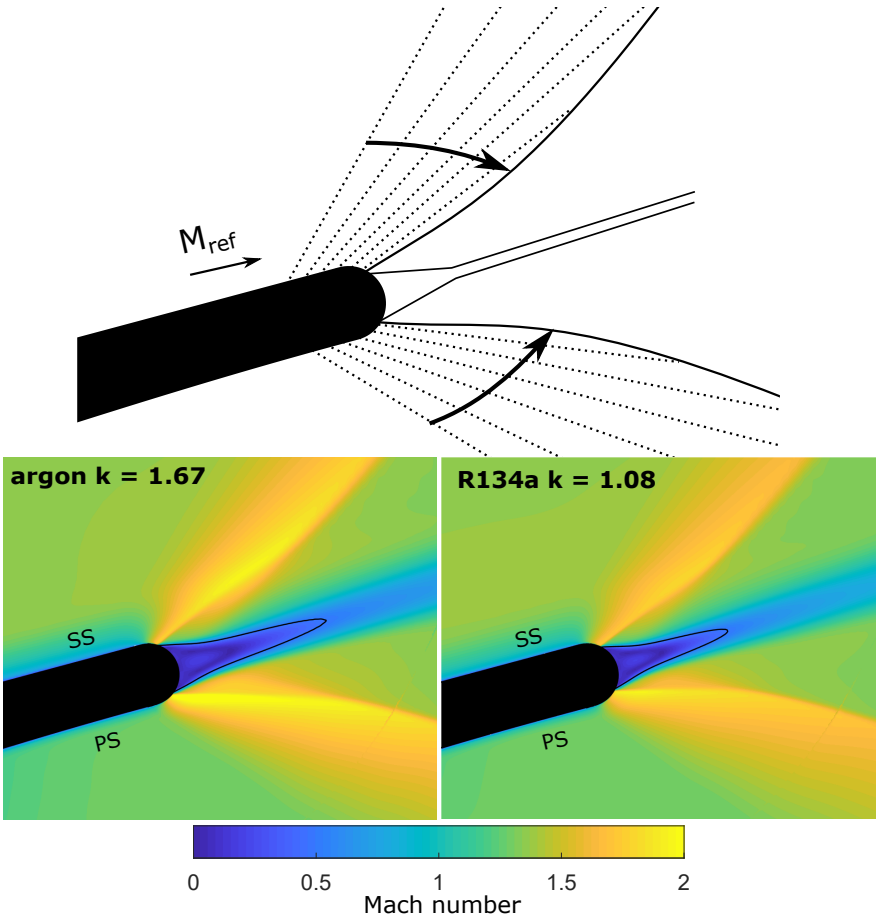

Fig. 5.11 Prandtl-Meyer fan at trailing edge with the example of argon and R134a at Mach number of 1.3. The solid line denotes a Mach number of 0.5.

In a next step the effect of the different turning angles on trailing edge loss is isolated. To that end the Prandtl-Meyer turning was extracted for the case of air and analytically applied to the other fluids. The Prandtl-Meyer turning around the trailing edge is defined as:

$$\Delta\nu = \nu(M_\mathrm{b}) - \nu(M_\mathrm{ref}) \tag{5.8}$$

where M_b is the isentropic Mach number based on the base pressure and ν is the Prandtl-Meyer function. For the case of air, the CFD showed a $\Delta\nu = 7.5°$. Applying this same $\Delta\nu$ to the other fluids, one can compute the theoretical M_b at a constant turning for all fluids of different k. Based on these computed values of M_b, the base pressure is computed, a dashed line of constant $\Delta\nu$ is drawn on top of the left plot of figure 5.10. This reveals that by fixing the turning around the trailing edge, the relative difference in trailing edge loss with k would be reduced significantly compared to the case of variable turning around the trailing edge.

Specifically, the difference in trailing edge loss is 5% between $k = 1.08$ and $k = 1.67$ while without the fixed turning the same fluids shown a difference of 29% in trailing edge loss. This means that the variation of the Prandtl-Meyer function with k is the primary driver of the loss associated with the trailing edge. Thus, on the basis of this analysis, it can be concluded that the change in trailing edge loss is mainly driven by the inviscid gas dynamics and principles of conservation.

Denton (1993) has introduced the following base pressure coefficient:

$$C_{p_\mathrm{b}} = \frac{p_\mathrm{b} - p_\mathrm{ref}}{\frac{1}{2}\rho_\mathrm{ref} \cdot V_\mathrm{ref}^2} \tag{5.9}$$

He states that the trailing edge loss, due to mixing, is equal to the given coefficient C_{p_b} times the ratio of trailing edge thickness A_te to pitch A_2. This given coefficient can be further adapted for compressible fluids:

$$C_{p_\mathrm{b},\mathrm{eff}} = \left(\frac{p_\mathrm{b}}{p_\mathrm{ref}} - 1\right) \cdot \frac{1}{k} \cdot \frac{2}{M_\mathrm{ref}^2} \cdot \frac{A_\mathrm{te}}{A_2} \tag{5.10}$$

This adaption is only valid for fluids that can be regarded as perfect gases and compressibility factor of one as it is the case for the fluids subject to this current analysis.

Figure 5.10 has a second plot on the right side, which shows for all four fluids, the trailing edge loss as a function of this effective base pressure coefficient $C_{p_\mathrm{b},\mathrm{eff}}$. Quite remarkably, the different lines of loss are collapsing onto one single line for the different fluids. This suggests that the observed differences in trailing edge loss are largely driven by changes to this effective base pressure coefficient. To that end, this base pressure coefficient is extracted for all the different Mach numbers that were previously regarded (see figure 5.12). As before, the base pressure and trailing edge blockage are extracted from the CFD simulations and then used in the analytical 1D loss model to compute the plotted loss. All data points are collapsing on one single line, strengthening the argument that ζ_te is indeed driven by $C_{p_\mathrm{b},\mathrm{eff}}$ to a large extent. Two conclusions can be made upon these findings. First of all, the given equation for $C_{p_\mathrm{b},\mathrm{eff}}$ (eq.5.10) captures all the relevant physics of the mixing process that is occurring downstream of the trailing edge. Secondly, as long as a turbine designer matches $C_{p_\mathrm{b},\mathrm{eff}}$, there are no differences in trailing edge loss to expected, independent of the working fluid.

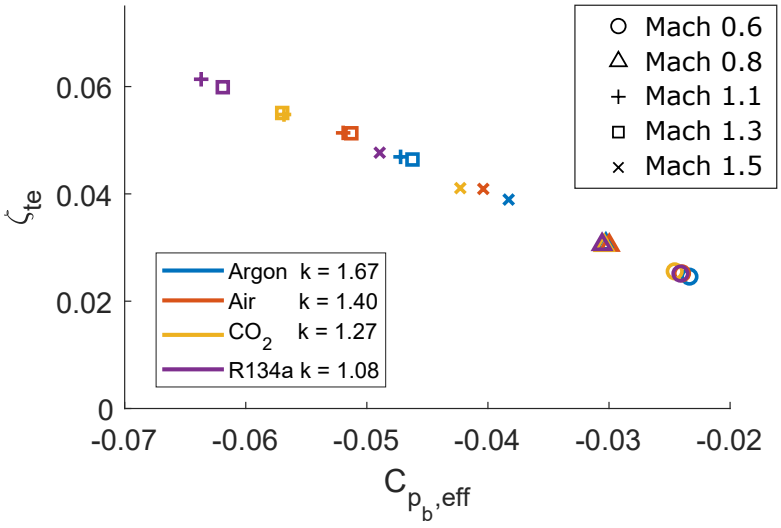

Fig. 5.12 Trailing edge loss plotted against effective base pressure coefficient for several Mach numbers and working fluids

5.3 A correlation for the effect of isentropic exponent on loss

In order to be able to include these findings in future turbine design, a correlation for the effect of k on loss was derived. Therefore, in figure 5.13, the total loss of different fluids is shown as relative loss to the loss of air ($k = 1.4$) at the same Mach number. Approaching transonic flow conditions, the sensitivity of loss to k is a strong function of the Mach number. The loss in this region is varying by 20% - 35% for the considered difference in k of this study. This sensitivity is further increased for rising Mach numbers.

Such a variation in loss with k as observed in these cases, cannot be neglected in turbine design, as most loss correlations that are currently used in the design process are based on experiments with air as working fluid. The application of such loss coefficient to working fluids with $k \neq 1.4$ is questionable. In order to provide a correction factor for fluids of varying isentropic exponent the following relation has been obtained:

$$\frac{\zeta_{\text{out}}}{\zeta_{\text{out}}^{\text{air}}} = 1.0 \qquad \text{for } M < 0.8 \tag{5.11}$$

$$\frac{\zeta_{\text{out}}}{\zeta_{\text{out}}^{\text{air}}} = a(k) \cdot (M + 0.25) + 1.0 \qquad \text{for } M > 1.0 \tag{5.12}$$

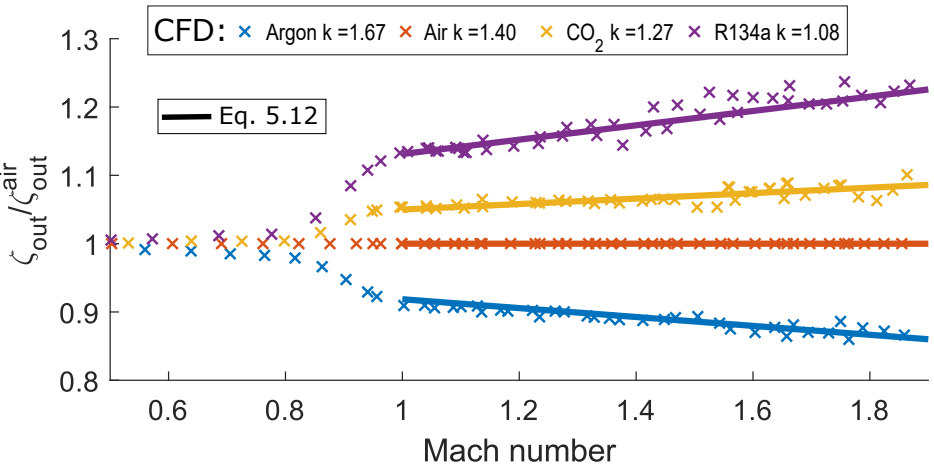

Fig. 5.13 Variation of mixed-out loss coefficient relative to air for different exit Mach numbers

with

$$a(k) = 0.1014k^3 - 0.2728k^2 - 0.122k + 0.4272 \tag{5.13}$$

This linear function of Mach number is plotted as solid line in figure 5.13 and it appears that this approximation is in good agreement with the relative change in loss that was extracted from the supersonic CFD cases. The gradient of this function is defined as $a(k)$, which itself is a monotonic non-linear function of k. For low values of isentropic exponent ($k < 1.4$) $a(k)$ yields a positive gradient and for high values of isentropic exponent ($k > 1.4$) $a(k)$ yields a negative gradient.

In Chapter 1, the variation of isentropic exponent across typical turbine applications has been presented (table 1.1). At the same time, the operating Mach numbers for these machines are varying as well. These exemplary operating points are plotted on the k-M design space in figure 5.14. Additionally, the contours of constant relative loss are shown for the entire design space. This highlights the universal application of the derived correlation for all kind of turbines and the importance of isentropic exponent on loss.

To give some more specific examples on how one could apply this correlation, consider the case of a first-stage HP turbine vane of an aero-engine operating with sonic conditions. In such a case, the high temperatures downstream of the combustion chamber together with some dissociation might result in $k \approx 1.26$, which would lead to a 5.4% variation of loss relative to operating with $k = 1.4$. In the future, high work turbines with exit Mach numbers of 1.2 are possible. For such turbines, the losses would rise to +6.3% relative to $k = 1.4$. The sensitivity of loss to k will be even higher for vanes operating at much higher Mach number,

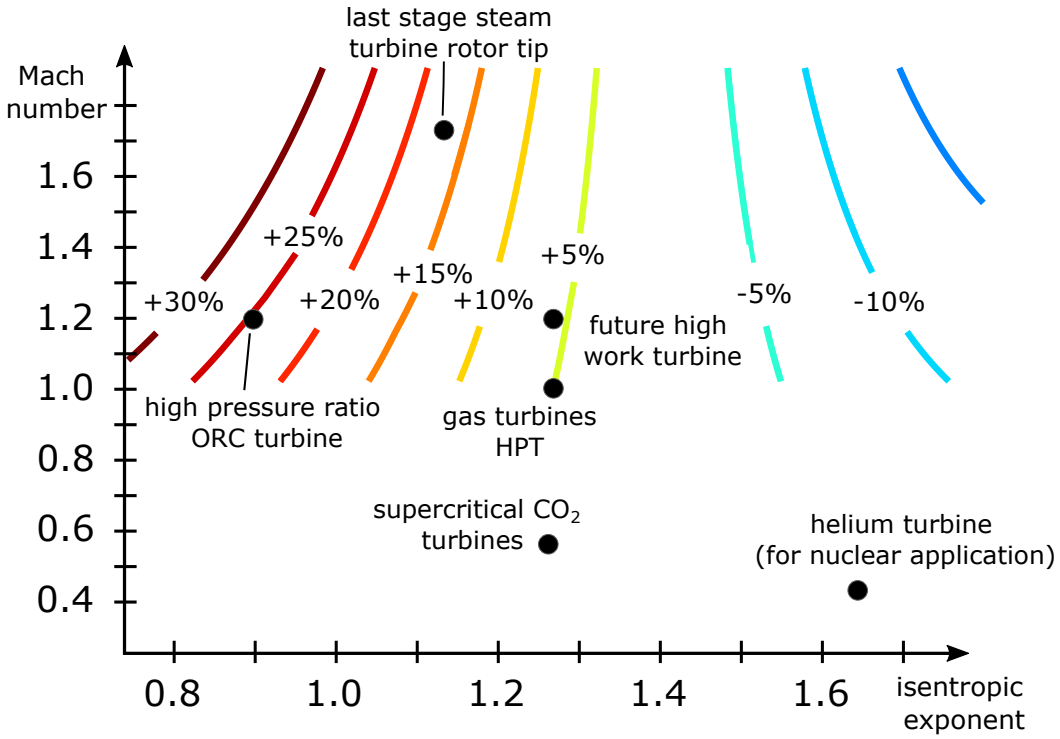

Fig. 5.14 Loss correlation within the k-M design space

such as last stage steam turbines or some types of high-pressure ORC turbines. An ORC turbine operating with pentane, could have an isentropic exponent of 0.9 or even lower in some cases. Assuming an exit Mach number of 1.2, this would lead to an increase of loss relative to air by 24.7%.

5.4 Vane loss for gas mixture

With the intention to further validate that the vane loss is primarily influenced by k, a gas mixture between argon and CO_2 is used to replicate a value of $k = 1.4$, same as air. Figure 5.15 shows the isentropic exponent that one obtains by mixing argon and CO_2 at different molar fractions. Interestingly k does not scale linearly with the molar fraction but initially stays closer to the low value of k for mixtures with a small portion of argon. For the purpose of matching the loss of air, a molar mass fraction of 0.5/0.5 was chosen.

The same set of 2D vane computations, at two different Mach numbers, was performed with this gas mixture using the same geometry as for air. The results of these computations can be seen in figure 5.16, and it becomes evident that the loss behaves in the same way as for air. This proves that the isentropic exponent is indeed the key driver for the difference

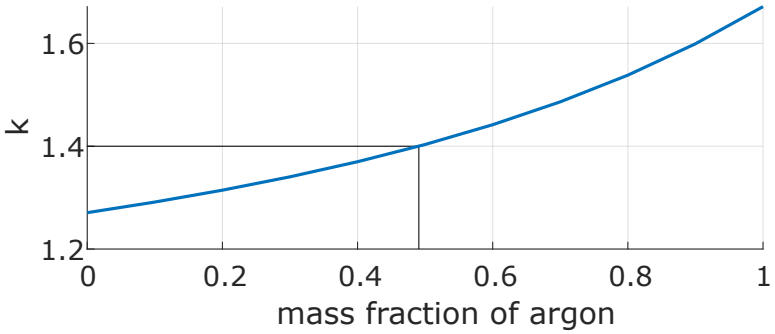

Fig. 5.15 Isentropic exponent of gas mixture of argon and CO_2 as function of mass fraction of argon

in the loss that was previously observed for blades operating at transonic conditions. More importantly, the results open up the possibility to use certain gas mixtures or even design new fluids for a particular turbine application to minimise losses due to k.

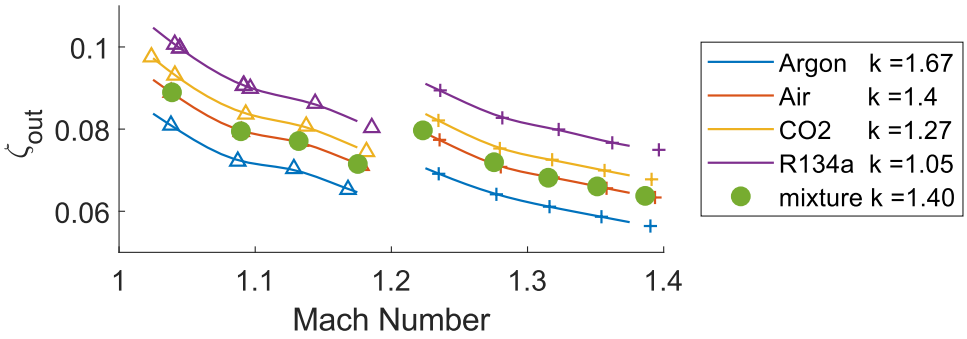

Fig. 5.16 Computed loss for gas mixture

5.5 Summary

It was shown that for vanes operating with exit Mach numbers above 0.9, loss is highly dependent on the isentropic exponent. Variations of 20-35% in the loss coefficient were observed over the range of conditions tested, whereby lower values of k lead to higher losses. The sensitivity of loss to k is increasing as vane exit Mach numbers are increased. Equation 5.12 provides a physics-based low-order model to account for this in design.

Aerodynamically speaking, the mechanisms responsible for the sensitivity of loss to k are a combination of shock loss within the blade passage and mixing loss downstream of the blade trailing edge. As these aerodynamic mechanisms are inviscid in nature, the effect of

the isentropic exponent will be applicable to all turbomachinery. As a consequence, turbines that are operating with low isentropic exponent and high Mach numbers will inevitably be more sensitive to geometrical tolerances (such as trailing edge thickness).

Chapter 6

Effect of compressibility factor Z on loss

So far, only the effect of k on turbine loss has been analysed. Furthermore, the cases that have previously been looked at, all lay in the region where the compressibility factor was around $Z \approx 1$, and the fluids were generally polytropic. Within this chapter, the design space is extended to include inlet conditions where Z ranges from $Z = 0.6 - 1.0$. This aims to answer the question of how Z affects loss.

Pentane is such a fluid which is often operated at low values of Z and which is also a common fluid for ORC turbines. Recalling figure 1.5, both the isentropic exponent k and the compressibility factor Z show quite similar behaviour on a temperature-entropy (T-s) diagram. Due to the similar behaviour of both properties k and Z, it is crucial to properly decouple Z from k and all other non-dimensional parameters. Only if the gas dynamics are matched between fluids through the similarity of all other non-dimensional parameters while varying Z, one can isolate the effects of Z.

6.1 Matching of gas dynamics for non-polytropic fluids

A polytropic fluid is one which obeys the polytropic relationship for an isentropic process:

$$\log(p/p_0) = k \log(\rho/\rho_0) \tag{6.1}$$

In a non-polytopic case one can fit a second-order approximation to the expansion process. This approximation yields α_{poly} and $\tilde{k}$ as coefficients:

$$\log(p/p_0) = \alpha_{\text{poly}} \log^2(\rho/\rho_0) + \tilde{k} \log(\rho/\rho_0) \tag{6.2}$$

If an expansion is occurring in a polytropic manner, $\alpha_{\text{poly}} = 0$ and $\tilde{k}$ will be equivalent to the previously defined isentropic exponent k. Hence, α_{poly} is a indicator of how polytropic or non-polytropic a fluid is behaving across a certain isentropic expansion.

Figure 6.1 shows an example pressure-density isentrope for pentane close to the critical point. The figure also shows both a linear (polytropic) approximation (equation 6.1) and a second-order approximation according to equation 6.2. The figure shows that at these conditions, the second-order approximation replicates the correct non-polytropic behaviour of the gas.

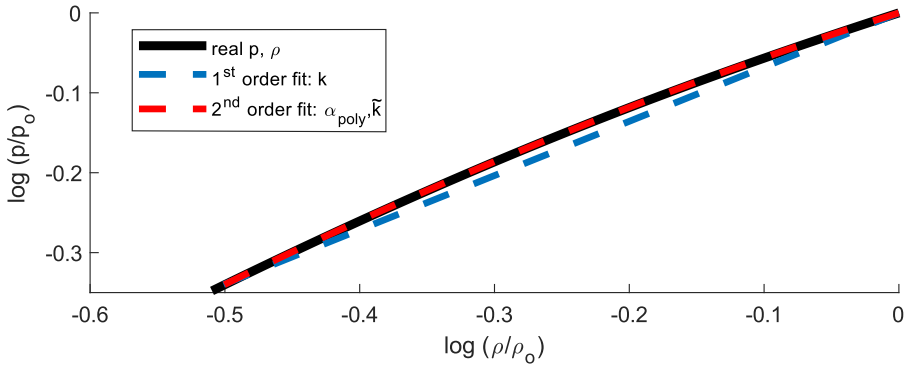

Fig. 6.1 Expansion of Pentane to Mach 1.3 close to critical point and $Z = 0.477$ ($p_r = 0.875$, $T_r = 0.984$)

Figure 6.2 shows how α_{poly} is varying for pentane with compressibility factor. Three regions mark the fluid conditions $Z > 0.8$, $Z = 0.6 - 0.8$ and $Z < 0.6$. At $Z = 1$ pentane is behaving like a polytropic fluid as $\alpha_{\text{poly}} \approx 0$. Within the region of $Z > 0.8$, there is only a small variation in α_{poly}. For the other two regions of lower Z, there is a much bigger variation in α_{poly}, which means that k does not reflect the proper inviscid gas dynamics any more and thus cannot be used to design the nozzle of a vane at those inlet conditions.

In figure 6.3 contours of α_{poly} are shown on the T-s diagram. One can see that the non-polytropic region occurs close to the critical point and at very high pressures.

Based on the data shown in figure 6.2, fluids for low values of Z will very likely behave in a non-polytropic manner. Therefore, using the isentropic exponent k to ensure that the gas dynamics are matched between fluids will not be adequate, and some different non-dimensional parameters have to be chosen that are more universally applicable.

In the previous chapter, the isentropic exponent was used for the vane design, because, for the case of polytropic fluids, k can be used to compute the Prandtl-Meyer function ν which is needed to generate the nozzle shape with the MoC. In the case of $\alpha_{\text{poly}} \neq 0$ this link is not given any more. In this case, instead of using k to compute the Prandtl-Meyer

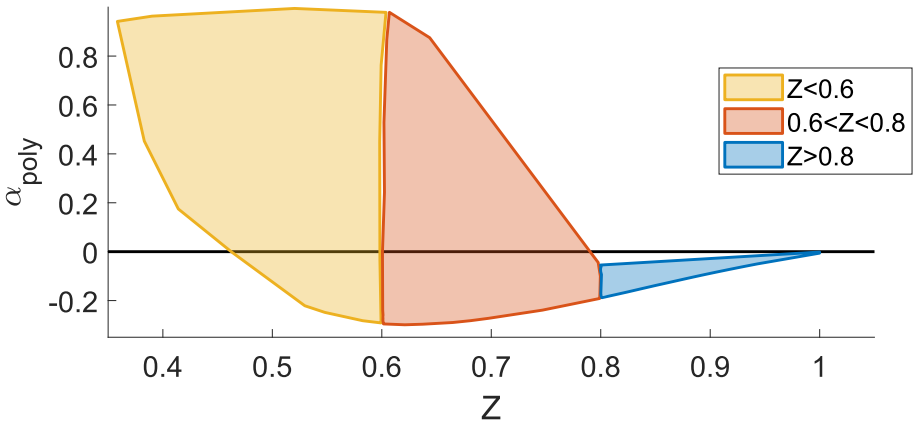

Fig. 6.2 Computed range of variation in α_{poly} with Z for pentane

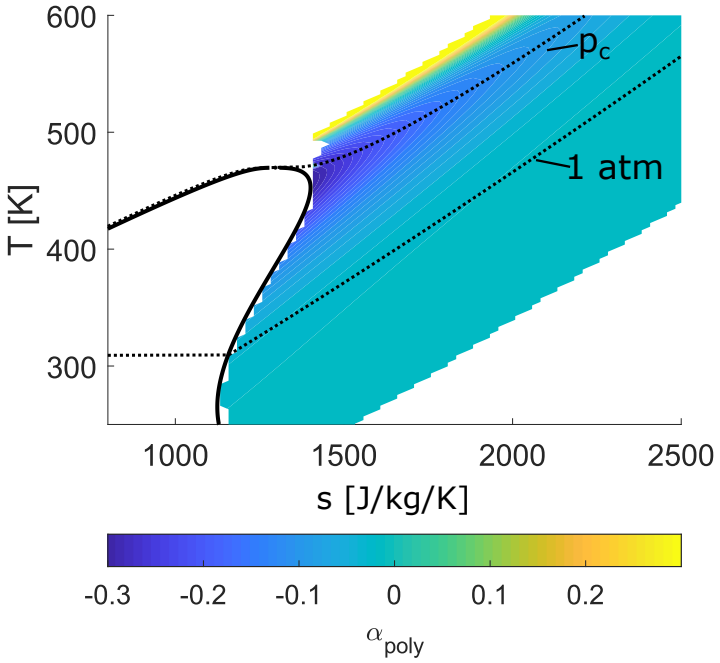

Fig. 6.3 Contours of α_{poly} for Pentane on T-s diagram

function, one can compute ν by numerically integrating equation 6.3. For this approach, the flow properties for an isentropic expansion are computed using the REFPROP routines.

$$d\nu = \sqrt{M^2 - 1}\frac{dV}{V} \tag{6.3}$$

To achieve the same gas dynamics between fluids, the Prandtl-Meyer function $\nu(M)$ should not only be matched at the desired design Mach number but over the same range of Mach numbers as they are occurring within the domain of the vane. For polytropic fluids, this is always the case, as $\nu(M)$ is a sole function of k. However, for non-polytropic fluids, this is not always the case. One way to match the Prandtl-Meyer function for such non-polytopic fluids is to match its derivative at the design Mach number (see figure 6.4).

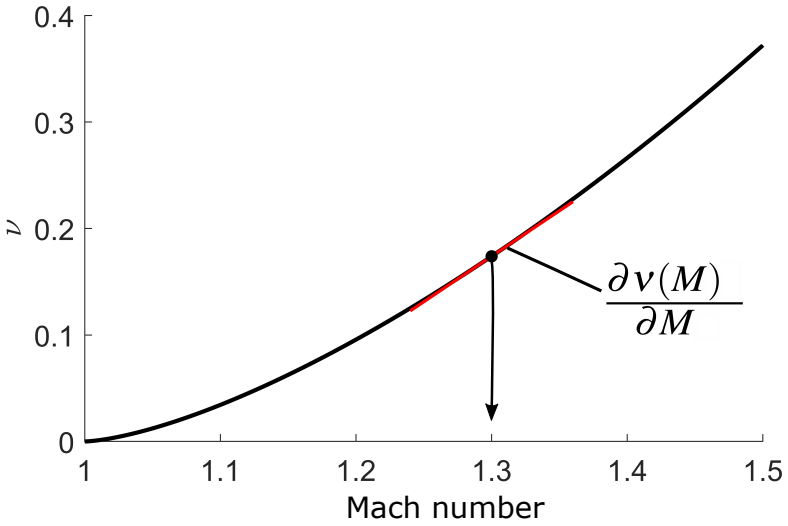

Fig. 6.4 Prandtl-Meyer function for pentane at Mach 1.30 and its derivative (marked in red)

This approach represents a first-order approximation, whereby $\frac{\partial \nu}{\partial M}$ can also be expressed as a function of the more commonly used fundamental derivative Γ. Thompson (1971) has derived the following relationship:

$$\mathrm{d}\nu = \frac{\sqrt{(M^2-1)}}{1+(\Gamma-1)M^2}\frac{\mathrm{d}M}{M} \tag{6.4}$$

For the analysis in this paper, the values of ν and Γ at the design Mach number are used to set similarity. This ensures similarity (to a leading-order) for both polytropic and non-polytropic fluids. In case of polytropic fluids these two parameters cannot be varied independently, but instead they can both be expressed by one parameter: the isentropic exponent k.

The two parameters (ν and Γ), which essentially set a universal inviscid design space across all fluids, were computed for all the fluids of the REFPROP library (see appendix A) on an evenly spaced grid on a T-s diagram. As before the data points are split up in the three regions of compressibility factor (see figure 6.5).

Additionally, there is a solid line which represents polytropic fluids where the isentropic exponent k is used to compute ν and Γ. Recalling figure 1.7, low values of ν represent high

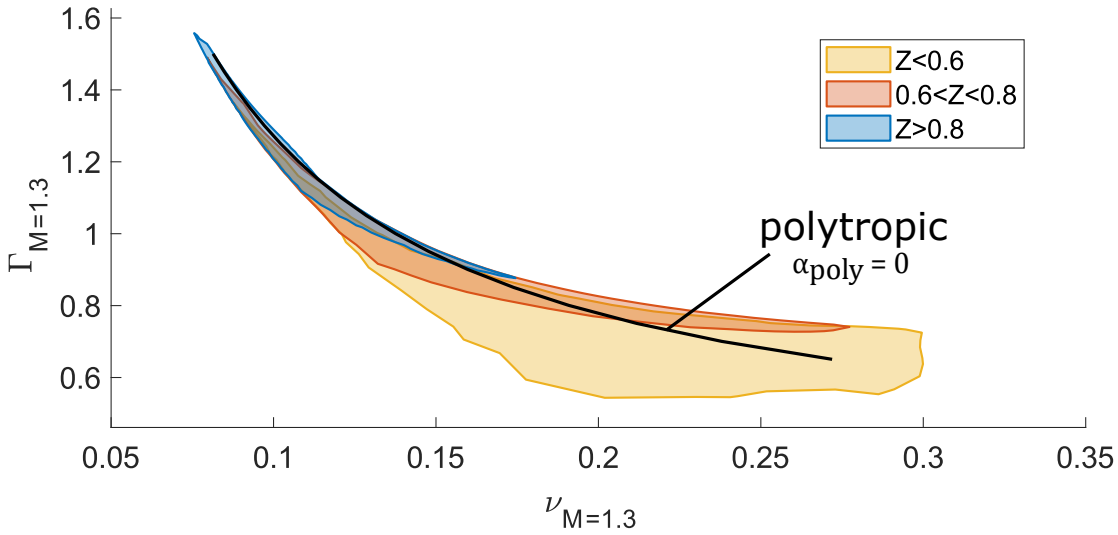

Fig. 6.5 Range of Prandtl-Meyer function and fundamental derivative at Mach 1.30 for different regions of Z (all fluids)

values of k and vice versa. The figure shows that for $Z > 0.8$, most fluids tend to behave polytropically or close to polytropically, while for low values of Z the fluids start to behave non-polytropically.

Looking at the regions of compressibility factor Z, it appears that there is a correlation between Z and ν, whereby high values of Z (>0.8) only exist for fluids with low Prandtl-Meyer function. At the same time, low values of Z only exist for high values of ν. The fundamental derivative is also dependent on Z; fluids operating with $Z > 0.8$ tend to exhibit high Γ while fluids operating at low Z tend to exhibit low Γ.

At any point in the design space of figure 6.5, there exist numerous fluid inlet conditions with a specific range in Z. Looking at such fluids will show the isolated effect that Z has on the performance of a supersonic vane. Furthermore, this shows that all three parameters ν, Γ and Z can be varied independently and are suited as non-dimensionals.

Thus the proposed non-dimensionals which are valid for non-polytropic fluids are:

$$\zeta = f\left(Re, M, \nu, \Gamma, Z\right) \tag{6.5}$$

In order to show that the Mach number can be varied independently as well, a plot similar to figure 6.5 was generated with a design Mach number of 1.3, 1.4, 1.5 and 1.6. Overlapping the extent of each design space at different Mach numbers (see figure 6.6) reveals that there are indeed fluid inlet conditions with the same ν, Γ and Z for different Mach numbers.

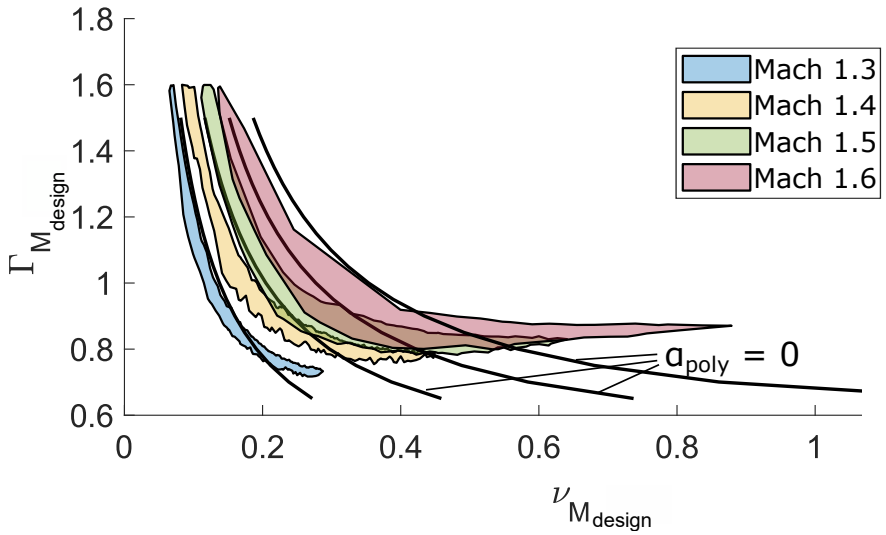

Fig. 6.6 Extent of fluid properties at fixed $Z = 0.6$ (all fluids)

6.2 Validation of matched gas dynamics

A series of CFD simulations were performed using the previously described matching. First of all, this should validate the approach that the gas dynamics at a specified Mach number are determined by ν and Γ and thus independent of Z. Secondly, based on these simulations, the influence of Z on the performance of a supersonic vane will be analysed.

Fluids and respective inlet conditions were chosen in such a way that ν and Γ were matched at the design Mach number of 1.30. At the same time, the set of matched fluids was chosen in such a way that there was a considerable variation of Z between the fluids. The different vanes were also scaled for each fluid such that the Reynolds number is constant across all cases ($1.7\text{x}10^6$) and thus, the boundary layer loss should be comparable. Based on equation 6.5, any changes in loss should be due to Z.

Table 6.1 Fluid properties for validation of gas dynamic matching ($M = 1.3$)

fluid	p_r	T_r	Z_average	α_poly	$\nu_{M=1.3}$	Γ
R14	2.27	1.31	0.72	0.338	0.118	1.099
SF_6	4.76	1.86	0.97	0.350	0.118	1.099
R22	1.05	1.12	0.75	-0.021	0.138	0.637
RC318	1.17	1.53	0.95	-0.008	0.138	0.637

In order to verify that the proposed approach of matching ν and Γ ensures correct matching of vane loading, simulations were performed of the fluids and conditions listed in Table 6.1.

Figure 6.7 shows Mach number contours for a vane designed to operate with R14. Within the nozzle, the flow is accelerated to design Mach number of 1.3. At the trailing edge of the blade, two oblique shocks are formed, whereby the pressure side shock is reflected off the suction side of the neighbouring blade.

Figures 6.8 and 6.9 shows the computed Mach number along the centre line extracted from the CFD for the fluids and conditions in Table 6.1. Cases for near polytropic ($\alpha_{poly} \approx 0$) and non-polytropic behaviour ($\alpha_{poly} \approx 0.34$) are shown. In each of these cases, the value of Z differs by around 25%. In each case, the Mach number distributions between the fluids are well matched despite the significant difference in compressibility factor. Even at the position of the oblique shock, shown in the detailed view, the dynamic similarity between the fluids of varying Z is given.

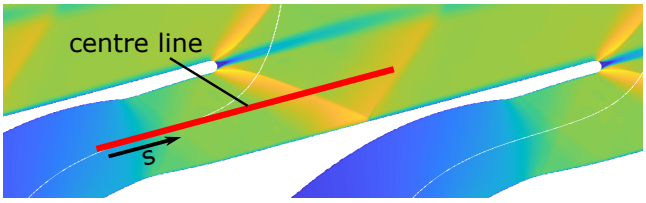

Fig. 6.7 Example Mach number contour with extent of centre-line indicated

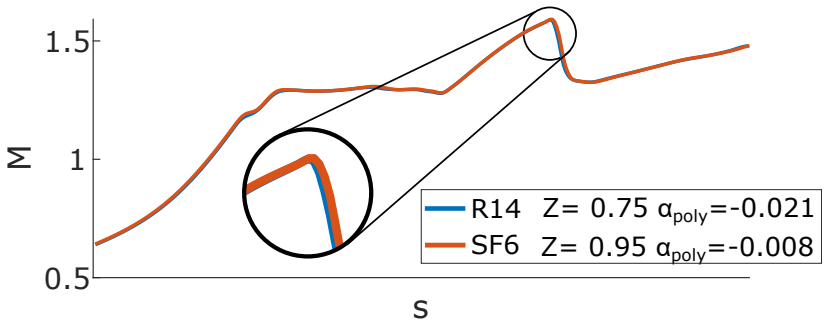

Fig. 6.8 Centre-line Mach number for $\alpha_{poly} \approx 0.34$

The results show that for both polytropic and non-polytropic fluid conditions, matching of exit Prandtl-Meyer function ν, Mach number M, and Fundamental Derivative Γ is sufficient to achieve similarity of the inviscid gas dynamics. Based on the matched Mach number between the fluids, the loading is therefore matched. This allows to isolate the effect of Z on loss alone.

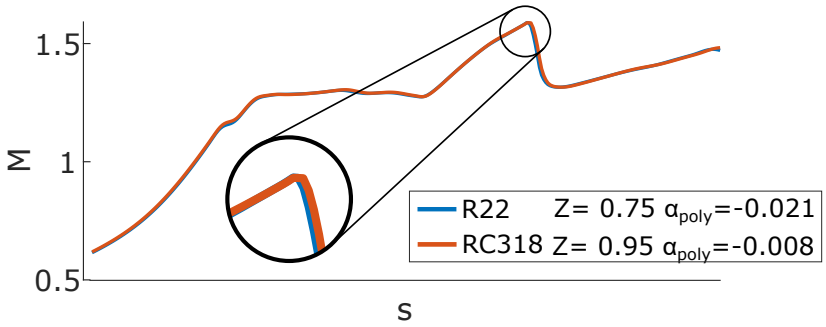

Fig. 6.9 Centre-line Mach number for $\alpha_{poly} \approx 0$

6.3 Loss analysis of CFD simulations

In order to determine the effect of Z on vane loss, CFD simulations were performed for vanes operating with the fluids and conditions described in Table 6.2. As discussed above, the conditions are set to ensure matching of loading, Mach number, Reynolds number and polytropic behaviour. Therefore, the effect of Z on loss is isolated.

Table 6.2 Fluid properties for CFD loss analysis

fluid	p_r	T_r	$Z_{average}$	α_{poly}
propane	1.4625	1.4450	0.8905	-0.0124
propylene	1.3628	1.3316	0.8488	-0.0171
R125	1.2807	1.3714	0.8925	-0.0121
R143a	1.3382	1.3472	0.8625	-0.0141
R22	1.0461	1.1185	0.7473	-0.0210
RC318	1.1717	1.5251	0.9502	-0.0081
SF_6	1.3164	1.3974	0.8957	0.0112

The computed mixed-out overall loss for these test-cases is shown in figure 6.10. The results indicate that the compressibility factor does have an impact on the performance of the vane, whereby low values of Z improve the performance. Even though the inviscid gas dynamics in the nozzle are matched between the fluids, the total loss is increasing by 8% between the lowest value of Z and the highest Z.

Using the same control volume as in the previous chapter (see figure 5.5), the total loss is split up in passage and trailing edge loss. The loss is interpolated to obtain a value at the design Mach number of 1.30.

First of all, figure 6.11 shows that both passage loss and trailing edge loss are affected by Z. For the given range of Z (0.75-0.95) the trailing edge loss rises by 8.45%. Similar to the previous chapter, the trailing edge loss is the largest share ($\approx 2/3$) of the overall loss.

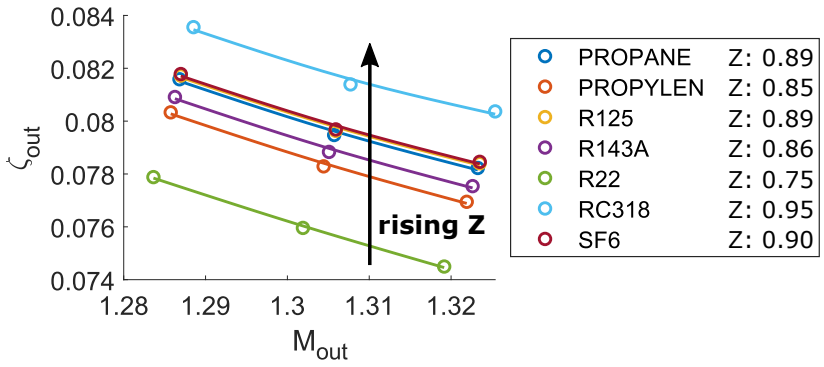

Fig. 6.10 Total loss for matched fluids ($\nu_{M=1.3} = 0.138$, $\Gamma = 0.637$)

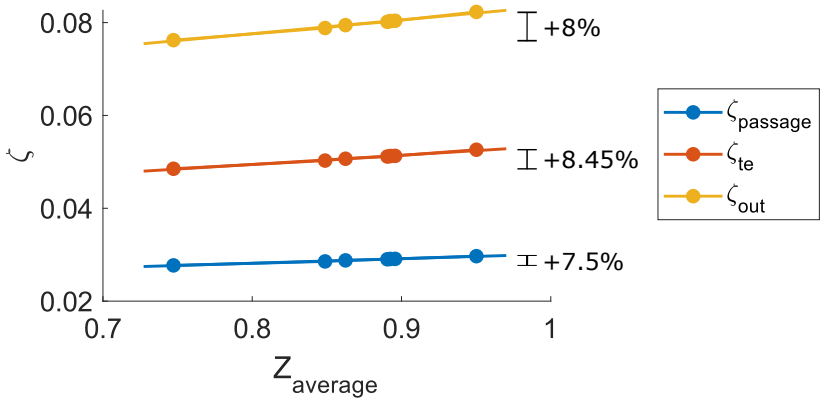

Fig. 6.11 Passage, trailing-edge and total loss for different Z

The passage loss increases by 7.15% between R22 ($Z = 0.75$) and RC318 ($Z = 0.95$). The observed difference in passage loss can have two sources: a difference in boundary layer loss and/or a difference in the shock loss.

To get an understanding of how the loss in both regions of the vane is affected by the compressibility factor, all of the three loss mechanisms (shock, boundary layer and mixing) are discussed next.

6.4 The effect of real gas behaviour on shock loss

The shock loss is explored first by looking at the analytical shock loss. To that end, REFPROP routines are used to compute the downstream subsonic properties of a normal shock while assuming conservation of mass, energy and momentum.

For the analytical loss calculation, an isentropic expansion to the design Mach number is assumed to obtain the upstream properties. In case of the shock loss, these are all the assumptions that are needed to compute a loss coefficient. As before the computed loss

coefficient is based on:

$$\zeta_{\text{shock}} = \frac{h_2 - h_{2,\text{s}}}{h_0 - h_{2,\text{s}}} \tag{6.6}$$

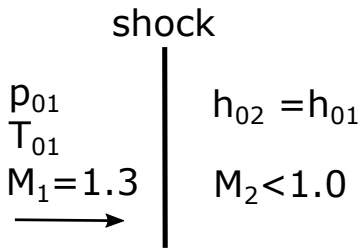

Fig. 6.12 Analytical shock loss calculation

For the entire T-s diagram, one cannot only map out the different non-dimensionals but also the analytical shock loss that would occur at the respective inlet conditions. For pentane, the shock loss has been computed for a pre-shock normal Mach number of $M_1 = 1.30$. The resulting contours of analytical shock loss can be seen in figure 6.13.

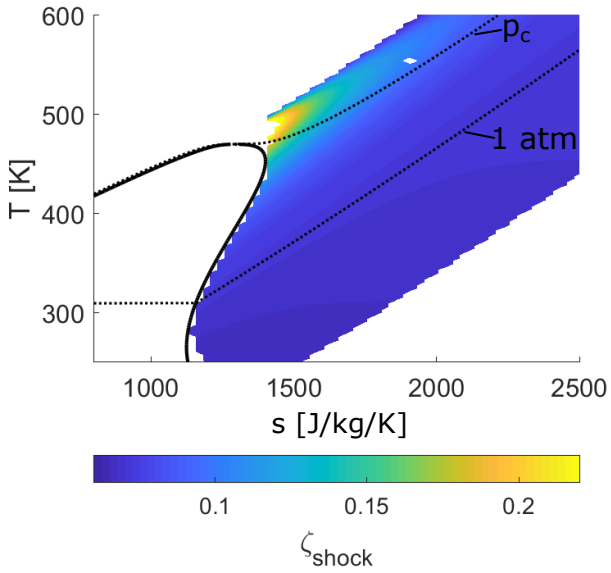

Fig. 6.13 Contours of analytical shock loss for pentane on T-s diagram. Iso-bars are drawn at p_c and 1 atm.

The contour plot reveals that the loss is particularly high close to the critical point. Compared to conditions at ambient pressure, the shock loss close to the critical point is increased by a 100%.

The previous chapter showed that the shock loss scales with the isentropic exponent. In order to see to what extent that approach applies to the entire design space, including

the non-polytropic inlet conditions, figure 6.14 shows the variation in shock loss with k for pentane for all feasible inlet conditions. The data is split up in different regions of Z. For the

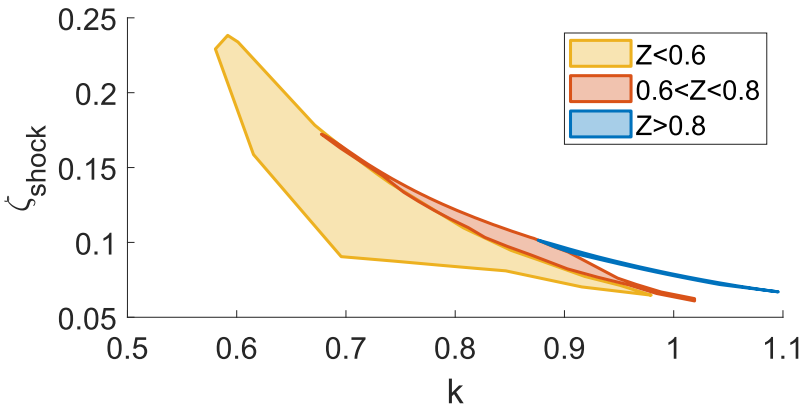

Fig. 6.14 Shock loss plotted against isentropic exponent for different regions of compressibility factor (pentane)

region of $Z > 0.8$, the analysis of the previous chapter holds up as all data points collapse on one line. Here, the shock-loss for a given upstream Mach number is purely a function of isentropic exponent k. In the red region where $Z = 0.6 - 0.8$ the fluid is subject to stronger real gas effects, and the data points start to scatter. This is the non-polytropic region where $\alpha_{\text{poly}} \neq 0$ and thus k is not sufficient any more to predict the occurring shock loss. The scatter in shock loss is even higher in the region of $Z < 0.6$.

The isentropic exponent collapses the shock loss for polytropic fluids as it is directly linked to the gas dynamics. Alternatively, one can directly compute the Prandtl-Meyer function ν based on the REFPROP routines for all grid points for the Mach number upstream of the shock ($M_1 = 1.3$). This 'true' representative of the upstream gas dynamics can be used as non-dimensional instead of k as seen in figure 6.15. This shows that $\nu_{M=1.3}$ appears to collapses the shock loss much better than the isentropic exponent before.

It was shown that for the case of pentane, the shock loss for a normal shock is proportional to the Prandtl-Meyer function at the Mach number just upstream of the shock. The same analytical shock loss can be computed for all the fluids available in the REFPROP library. The result can be seen in figure 6.16. As for the case of pentane, all data points are collapsing on one line suggesting that the Prandtl-Meyer angle is the underlying parameter determining the shock loss at a certain Mach number.

Figure 6.16 still indicates some variation in shock loss at a given ν, especially at $\nu_{M=1.3} > 0.15$. Slices of constant $\nu_{M=1.3}$ are extracted at four different positions (see figure 6.16) and are plotted against compressibility factor. Figure 6.17 shows that while for $\nu = 0.1$ there is

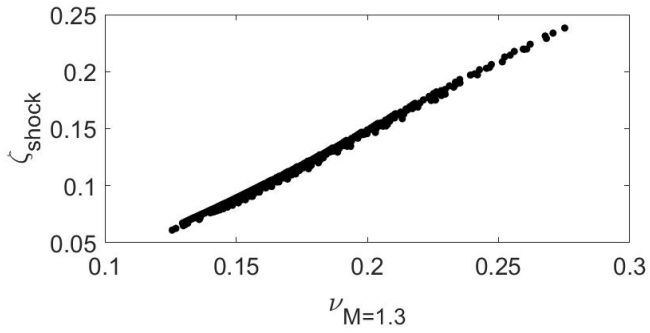

Fig. 6.15 Shock loss plotted against Prandtl-Meyer angle at shock Mach number (pentane)

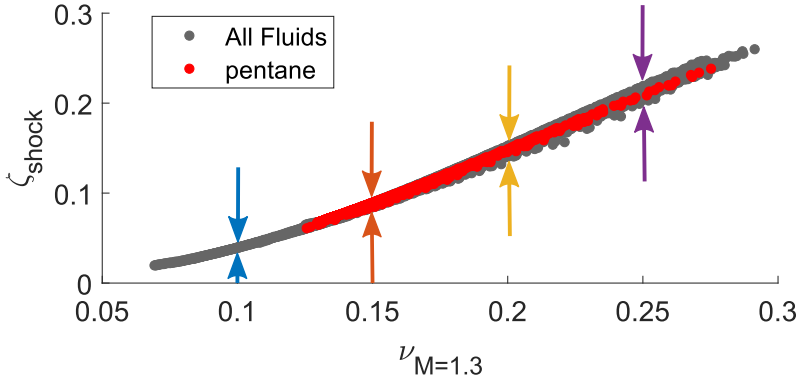

Fig. 6.16 Shock loss at grid points plotted against Prandtl-Meyer angle at shock Mach number (all fluids)

little variation of shock loss with Z, for greater values of ν the sensitivity to Z is increasing. Specifically, at a fixed value of $\nu_{M=1.3}$, the shock loss ζ_{shock} is decreasing for lower values of Z. This change in sensitivity can also be seen in figure 6.18, which shows the derivative of ζ_{shock} with respect to Z, plotted against $\nu_{M=1.3}$. Though there is sensitivity of ζ_{shock} to Z, the sensitivity to ν remains much higher. To give an example, at $\nu_{M=1.3} = 0.2$ and $Z = 0.7$ a 10% change in Z yield a 0.46% change in loss, while at the same time a 10% change in $\nu_{M=1.3}$ yields a 18% change in loss.

Considering the shock loss in a real vane, the Mach number normal to the shock just upstream of the shock front is varying along its front. An example of such a shock front is shown in figure 6.19, and it can be seen that there is a slightly higher Mach number in the proximity to the trailing edge (x) compared to the suction side of the neighbouring blade (y). It was shown before, that the shock loss coefficient is matched if the Prandtl-Meyer function at the same Mach number as the Mach number normal to the shock is matched. Knowing that there is shock loss occurring over a whole range of Mach numbers, one can say that ν

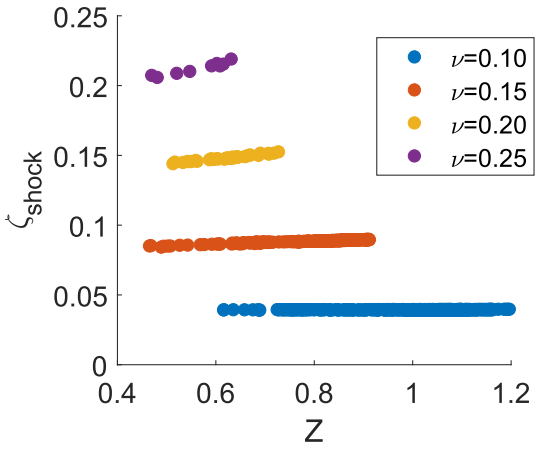

Fig. 6.17 Effect of Z on ζ_{shock} at different values of ν

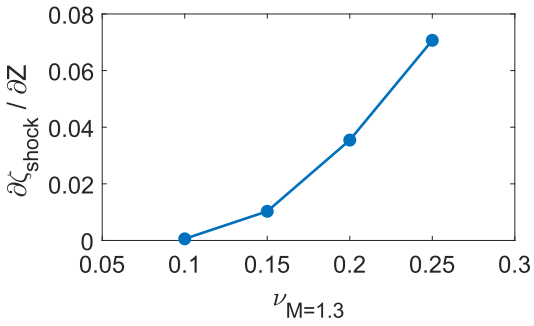

Fig. 6.18 Derivative of ζ_{shock} at different values of ν

should be matched across the same range of Mach numbers as there are shocks occurring in the flow field. Through fixing the fundamental derivative at the design Mach number, the derivative of ν is fixed as well. This first-order approximation should lead to constant ν over a range of Mach numbers close to the design Mach number.

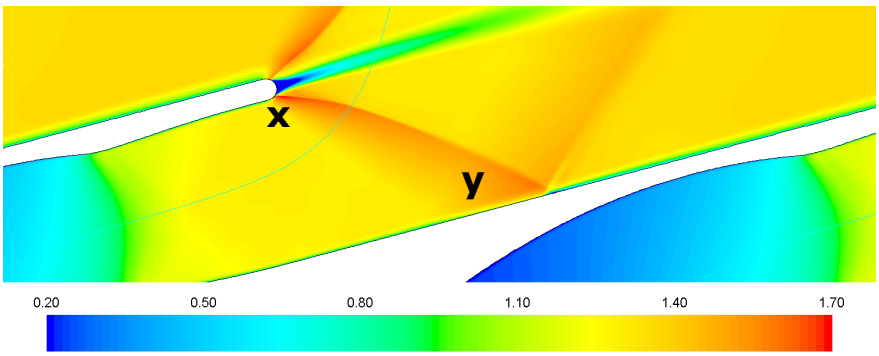

Fig. 6.19 Mach number contours of pentane showing oblique shock

In the case of the fluids and conditions tested here, the Prandtl-Meyer function ν was fixed at $\nu_{M=1.3} = 0.138$. For this given value the derivative $\frac{\partial \zeta_{\text{shock}}}{\partial Z}$ is 0.00696 (see figure 6.18). For a change in average Z from 0.75 to 0.95 one can expect a $\Delta\zeta_{\text{shock}}$ of $1.392\text{x}10^{-3}$, which translates to a 3.85% rise in passage loss.

While the analysis of shock loss has shown a certain dependency of loss on Z, whereby shock losses are reduced for lower values of Z, the observed change in ζ_{passage} is of a greater magnitude (7.15%). Therefore the difference in passage loss must also be due to the effect of Z on the boundary layer.

6.5 Impact of compressibility factor Z on boundary layer

The energy thickness is computed to assess how much loss is associated with each boundary layer. Figure 6.20 shows that the suction side is the more significant contributor to the vane boundary layer loss, as this boundary layer was also subject to the shock-boundary layer interaction. Interestingly though, the boundary layer thickness to either side of the trailing edge shows the same dependency on Z and the relative difference between the fluids in boundary layer thickness is the same. Specifically, the combined energy thickness is 17.1% greater for RC318 ($Z = 0.95$) than for R22 ($Z = 0.75$). This indicates that the shock-boundary layer interaction is not the key mechanism driving the difference in the passage loss, but instead, Z appears to impact the overall growth of the boundary layer.

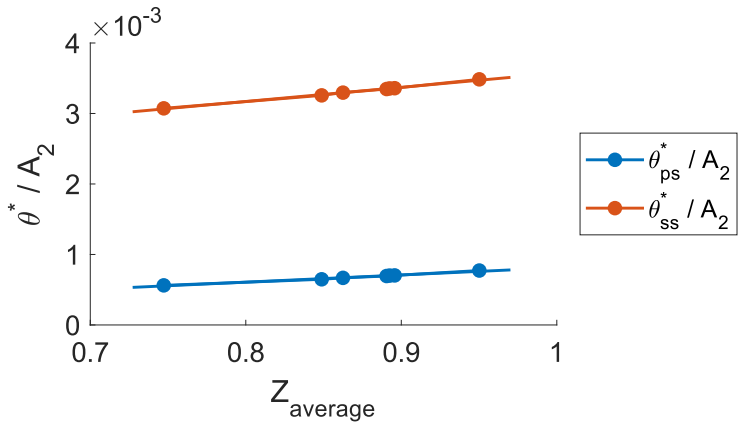

Fig. 6.20 Boundary layer thickness at suction side and pressure side upstream of the trailing edge

Simplified computations of a flow over a flat plate were performed to get a better understanding of how Z impacts the growth of a boundary layer. The simulations were performed for R22 and RC318, with matched Prandtl-Meyer function and fundamental derivative. However, the average Z differed between 0.75 and 0.95. To be sure that any effect Z might have on the boundary layer is not dependent on a specific turbulence model, the simulations were repeated for a range of different turbulence models and a laminar calculation. For all simulations, the wall was set to be adiabatic. As before the geometry was scaled to match the Reynolds number between the two fluids and to match the Reynolds number of the previous vane calculations.

The boundary layer thickness was computed along the wall, whereby the displacement thickness δ^*, momentum thickness θ and energy thickness θ^* were computed in their compressible form (Greitzer et al. (2007)).

$$\delta^* = \int_0^{y_E} \left(1 - \frac{\rho u_x}{\rho_E u_E}\right) \mathrm{d}y \tag{6.7}$$

$$\theta = \int_0^{y_E} \frac{\rho u_x}{\rho_E u_E} \left(1 - \frac{u_x}{u_E}\right) \mathrm{d}y \tag{6.8}$$

$$\theta^* = \int_0^{y_E} \frac{\rho u_x}{\rho_E u_E} \left(1 - \frac{u_x^2}{u_E^2}\right) \mathrm{d}y \tag{6.9}$$

The simulations with the different turbulence models and the laminar simulation all showed the same impact of Z on the boundary layer. Figure 6.21 shows the Mach number contours for R22 in the computational domain, with a laminar wall on the bottom. Additionally, velocity profiles are extracted at two axial positions. The different boundary layer thicknesses are computed along the axial direction to compare the growth rate between the two fluids (see figure 6.22). Fluctuations in the quantities occur due to weak shock reflections.

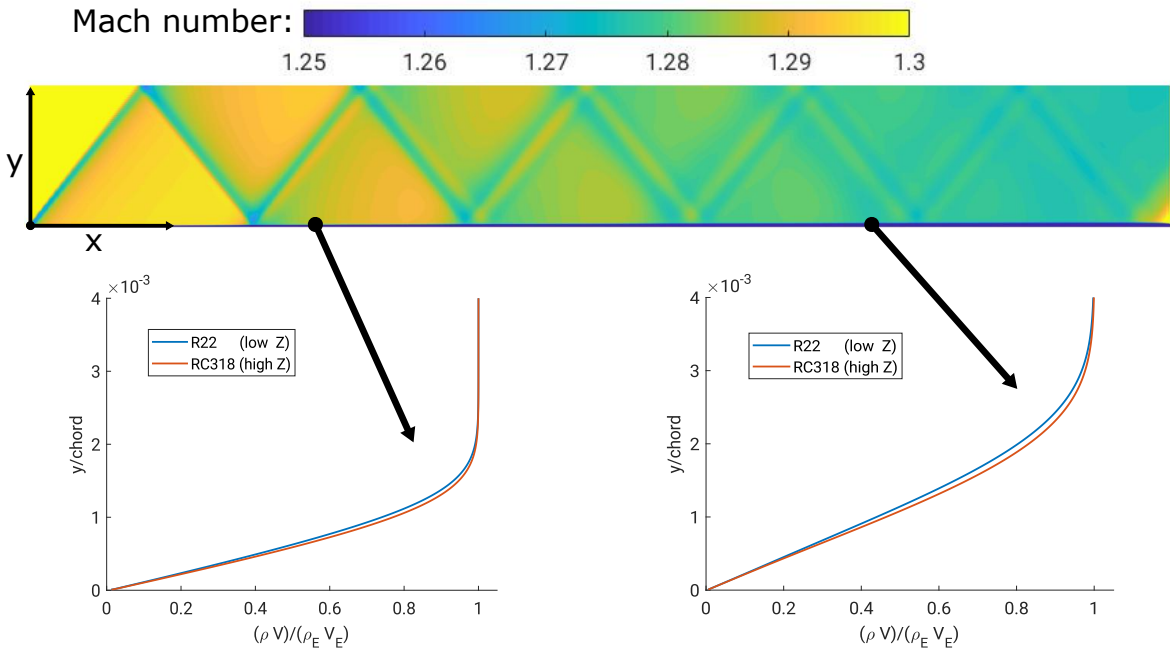

Fig. 6.21 Velocity profiles within the boundary layer at two axial positions for R22 and RC318

The two fluids do show a difference in the boundary layer growth, whereby the displacement thickness appears to behave oppositely as the momentum thickness and the energy thickness. While the displacement thickness is higher for a lower compressibility factor, the energy/momentum thickness is smaller for the fluid with lower Z. The effect this has on the

loss of the flow can be seen in figure 6.25, which shows that as for the vane, even on this simplified geometry without pressure gradient, a lower value of Z leads to a lower loss being generated in the boundary layer.

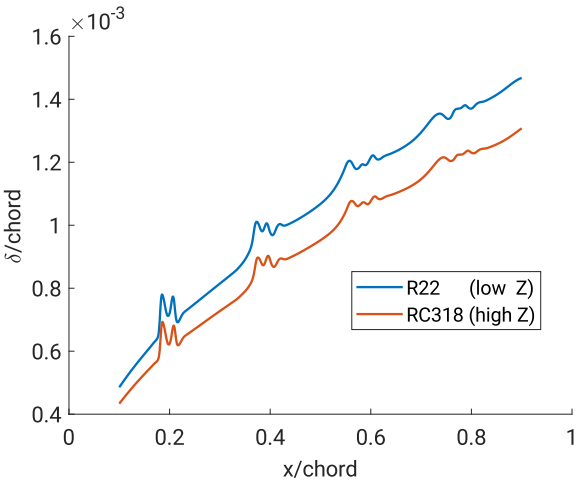

Fig. 6.22 Displacement thickness for laminar flow over flat plate for low and high Z

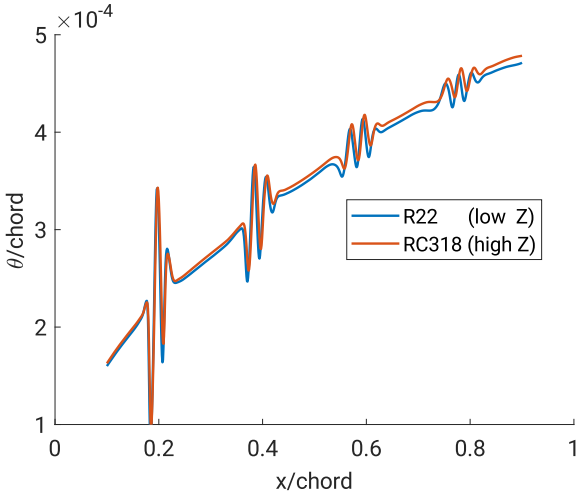

Fig. 6.23 Momentum thickness for laminar flow over flat plate for low and high Z

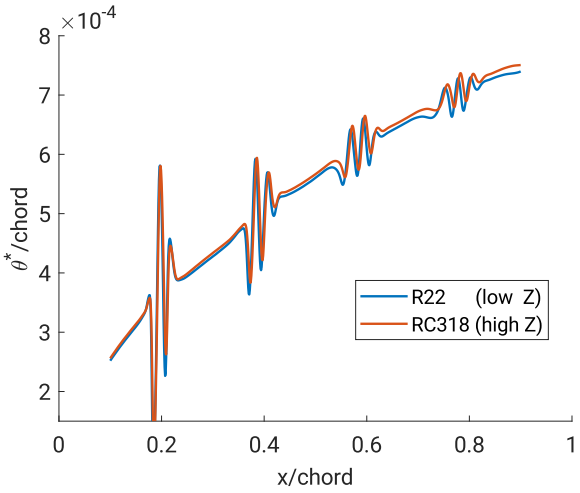

Fig. 6.24 Energy thickness for laminar flow over flat plate for low and high Z

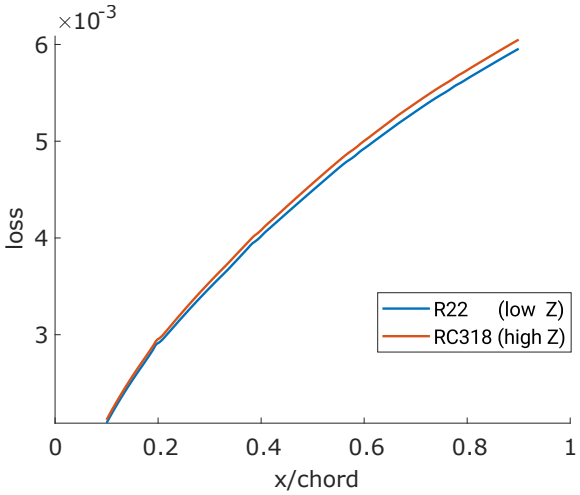

Fig. 6.25 Loss coefficient for laminar flow over flat plate for low and high Z

In addition to the integral boundary layer thicknesses, three parameters that are commonly used when analysing the state of a boundary layer are the shape factor H, the skin friction coefficient C_f and the dissipation coefficient C_d (Greitzer et al. (2007)). The two coefficient

are provided by the integral form of the boundary layer equations.

$$H = \frac{\delta^*}{\theta} \tag{6.10}$$

$$\frac{C_f}{2} = \frac{\mathrm{d}\theta}{\mathrm{d}x} + (H + 2 - M_\mathrm{E}^2)\frac{\theta}{u_\mathrm{E}}\frac{du_\mathrm{E}}{\mathrm{d}x} \tag{6.11}$$

$$2C_d = \frac{\mathrm{d}\theta^*}{\mathrm{d}x} + (3 - M_\mathrm{E}^2)\frac{\theta^*}{u_\mathrm{E}}\frac{\mathrm{d}u_\mathrm{E}}{\mathrm{d}x} \tag{6.12}$$

Computing the three parameters for the two fluids with varying Z shows,that while H is increasing by about 17% for the low Z fluid, both C_f and C_d are reduced by about 4% for the fluid of low Z (computed for SA turbulence model).

The relative rise in boundary layer loss between $Z = 0.75$ and $Z = 0.95$ for a range of different turbulence models can be seen in figure 6.26. Additionally, the simulation was repeated for subsonic inlet conditions ($M = 0.4$) using the Spalart-Allmaras turbulence model. While there is still the same trend of how the boundary layer loss is affected by Z, this is significantly less than for the supersonic flow. This suggests a strong dependence on Mach number.

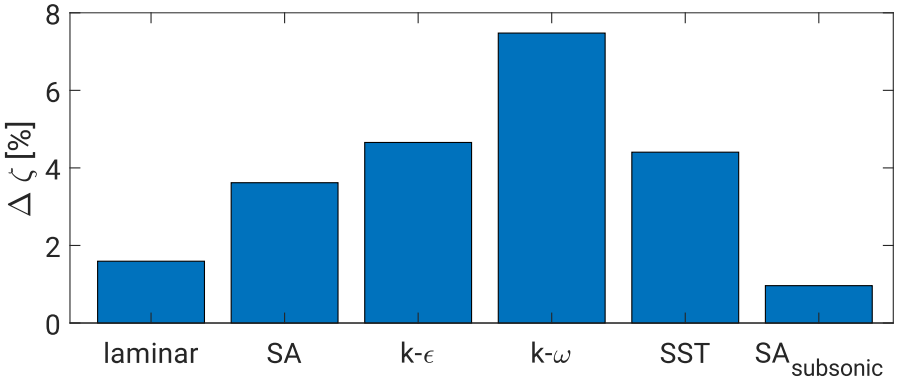

Fig. 6.26 Relative change in boundary layer loss between R22 ($Z = 0.75$) and RC318 ($Z = 0.95$) for multiple turbulence models

Although the sensitivity of boundary-layer loss to Z varies with each viscous model and Mach number, the underlying effect of Z on the boundary layer is observed for all cases, and is thus independent of the chosen turbulence model.

6.6 The effect of real gas behaviour on mixing loss

This next section will focus on the mixing loss by once again looking at an analytical loss coefficient. The analytical loss coefficient of the mixing process can be computed by using

the simplified trailing edge mixing box that assumes no tangential loading at the trailing edge as it has been used in the previous chapter (see figure 5.8).

For the case of the mixing loss, one needs to make some additional assumptions: effective trailing edge thickness and base pressure. For this analytical approach, the effective trailing edge thickness was assumed to be constant across all cases. In this case, a TE to pitch ratio of 3% was prescribed as it was the case in the previous vane designs. The more difficult parameter to set though is the base pressure. Assuming a constant base pressure would not be feasible as one wants to consider a whole range of different working fluids with a highly fluctuating isentropic exponent. The pressure ratio between fluid of different k to obtain the same design Mach number already differs significantly. Therefore, the decision was made to set the isentropic base Mach number to be constant across all vanes $M_{\mathrm{b}} = 1.65$. The isentropic base Mach number M_{b} is computed based on the trailing-edge base pressure. In the CFD the base Mach number M_{b} is varying between 1.62 and 1.64 for the fluids given in table 6.2. The assumption of constant base Mach number is an approximation in order to simplify the analysis at this point. The effect of base Mach number will be assessed later.

As for the analytical shock loss, the mixing-loss coefficient has been computed for pentane for all feasible inlet conditions. The resulting contours of analytical mixing loss can be seen in figure 6.27.

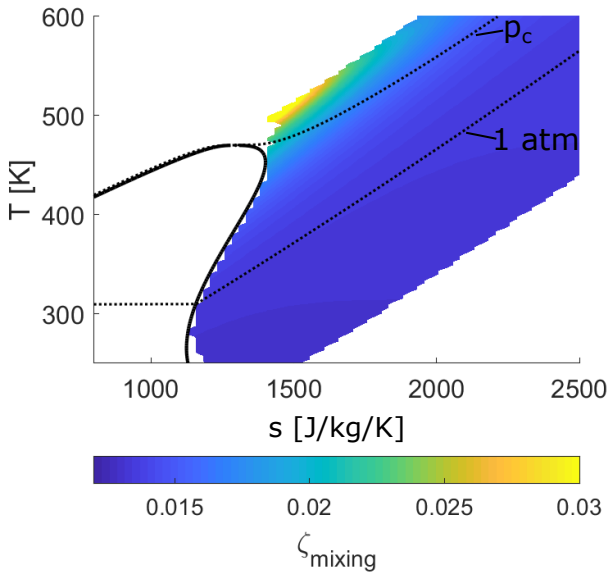

Fig. 6.27 Contours of analytical mixing loss for pentane on T-s diagram. Iso-bars are drawn at p_{c} and 1 atm.

Similar to shock loss, the loss seems to rise towards the critical point. There is a difference between the two losses though, where for the shock loss the maximum loss appears to be located right at the critical point, this is not the case for the mixing loss. Here, the loss appears to further increase for $p > p_c$.

It is worth mentioning that at this point the absolute value of the mixing loss is of no real interest, as this is highly dependent on the geometry of the trailing edge, e.g. the mixing loss is a linear function of the effective trailing edge thickness.

The previous chapter already discussed the trailing edge loss and the associated mixing loss, whereby the base pressure coefficient from Denton and Xu (1990) was introduced. While before the coefficient was transformed to a compressible version, using perfect gas relations, this time the coefficient is used as-is while using a reference density ρ_{ref} and reference velocity V_{ref} which were defined as the density/velocity upstream of the control volume.

$$C_{p_b} = \frac{p_b - p_{ref}}{\frac{1}{2}\rho_{ref} \cdot V_{ref}^2} \tag{6.13}$$

$$C_{p_b,eff} = -C_{p_b} \cdot \frac{A_{te}}{A_2} \tag{6.14}$$

All the properties are computed, assuming isentropic expansion and using the REFPROP routines. Figure 6.28 shows quite remarkably that again the analytical mixing loss collapses nicely with this effective base pressure coefficient. The results suggest that as long as $C_{p_b,eff}$ is matched through the gas dynamics, there is no dependence on Z.

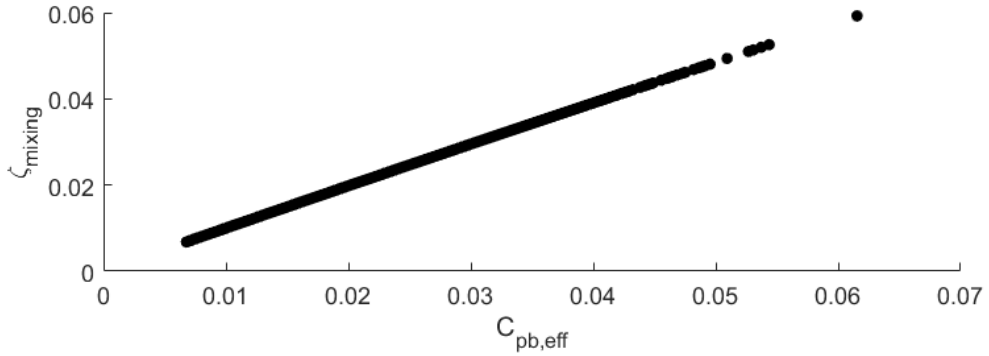

Fig. 6.28 Mixing loss at grid points plotted against effective base pressure coefficient (all fluids)

Coming back to the set of fluids, that were analysed before, computing the base pressure coefficient with a constant base Mach number yields a 0.92% change in C_{p_b} for the given

range of fluids (see figure 6.29). This difference in base pressure coefficient can be explained by the fact that the gas dynamics were matched at the nozzle exit Mach number. At sonic conditions, the Prandtl-Meyer function is always 0 for all fluids, which is why $\nu(M)$ is well matched in the region of Mach 1.0-1.3. Right at the trailing edge though, the flow is locally accelerated to much higher Mach numbers. At those Mach numbers, the gas dynamics start to divert between the fluids. This difference then yields the different C_{p_b}.

Extracting the real base pressure from the CFD though reveals that the isentropic base Mach number is changing slightly from 1.62 to 1.64 for the given fluids. Computing the C_{p_b} for these extracted base pressures gives a rise in C_{p_b} of 6.64%.

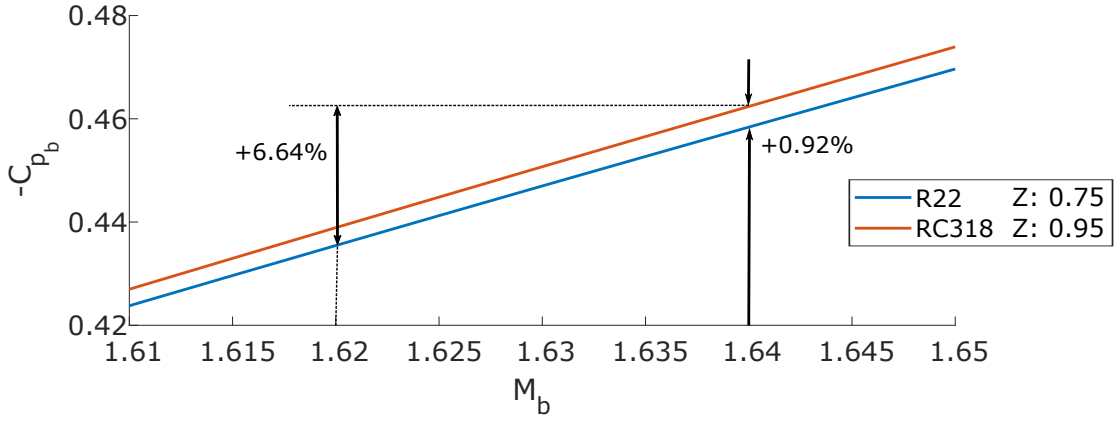

Fig. 6.29 C_{p_b} as function of isentropic base Mach number

The trailing edge loss coefficient can be approximated by $\zeta_{te} = -C_{p_b} \cdot \frac{A_{te}}{A_2}$, whereby A_{te} reflects the effective trailing edge thickness. The previous section has revealed that Z affects the boundary layer in such a way, that for lower values of Z, the displacement thickness is increased and the momentum and energy thickness are reduced.

In order to quantify how much of the change in trailing edge loss can be accounted to this change in Z and how much can be accounted to the small difference in base Mach number, one can apply the product rule.

$$\Delta\zeta_{te} = (-\Delta C_{p_b}) \cdot \left(\frac{A_{te,eff}}{A_2}\right) + (-C_{p_b}) \cdot \Delta\left(\frac{A_{te,eff}}{A_2}\right) \tag{6.15}$$

$$\Delta\zeta_{te} = 0.0032488 + 0.0008503 \tag{6.16}$$

The equation yields that the difference in trailing edge loss is primarily driven by the difference in base Mach number, accounting for 79% of $\Delta\zeta_{te}$. The compressibility factor, which impacts the boundary layer, only accounts for roughly 21% of the rise in trailing edge loss for higher values of Z.

6.7 Summary

In this chapter, it was shown that achieving similarity in Mach number distributions between fluids operating at low compressibility factor ($Z < 0.8$) can be achieved when the Prandtl-Meyer function ν and fundamental derivative Γ are matched at turbines design Mach number. This enables the effects of compressibility factor Z to be isolated for a turbine stator vane.

The total loss is affected by the compressibility factor in two main ways. First, through a change in boundary layer loss. Secondly, through a change in shock loss. For two vanes operating with varying Z from 0.75 to 0.95, the passage loss will be affected by both loss mechanisms in approximately equal parts, which leads to a rise in ζ_{passage} of 7.5%. The change in boundary layer thickness also affects the mixing loss that occurs at the trailing edge. Overall the trailing edge loss is reduced by 8.45% for the given reduction of Z. The resulting total loss of the vane is decreased by 8% for the same range in the compressibility factor (0.95 to 0.75).

For a given vane with a design Mach number of 1.3, it has been shown in the previous chapter that a 10% change in k (1.4 to 1.26) would yield a 6.7% rise in total loss. The results in this chapter show that a 10% change in Z (0.8 to 0.72) would only lead to a 3.1% reduction in total loss for the same vane of Mach 1.3. Thus, in comparison to the effect of the isentropic exponent, the dependency of the total loss on Z is significantly lower.

Chapter 7

Real gas effects in high-pressure turbine stage

In this chapter, the effects of isentropic exponent k and compressibility factor Z on a radial turbine stage are investigated. The chapter consists of two parts. First, the implication for the design of a radial turbine operating with real fluids will be discussed. Second, unsteady CFD simulations will be used to isolate the effects of k and Z.

7.1 Design of radial turbine with real fluids

In the initial design of a turbine stage, meanline calculations are performed to set the overall shape and run conditions of the turbine. At this stage, a group of non-dimensional parameters are chosen that will define the shape of the stage and its performance later on.

In the case of an ideal gas, classic non-dimensional parameters are suited to predict the performance of a turbine. For geometrically similar machines the independent parameters typically are the non-dimensional mass flow Θ, the non-dimensional speed M_{u}, the Reynolds number Re and the ratio of specific heats γ. Though the ratio of specific heats is usually neglected if one is only interested in a single working fluid. Moreover, the Reynolds number effects are usually neglected as well for radial turbines which then leaves two parameters, which are commonly used to draw the performance maps of a turbine (Whitfield and Baines (1990)).

$$[PR, \eta] = f(\Theta, M_{\mathrm{u}}, Re, \gamma) \tag{7.1}$$

$$[PR, \eta] \approx f(\Theta, M_{\mathrm{u}}) \tag{7.2}$$

whereby the parameters are defined as follows:

$$\Theta = \frac{\dot{m}}{\rho a \pi d_{\text{rotor}}^2/4} \tag{7.3}$$

$$M_{\text{u}} = \frac{U}{a_{0,\text{in}}} \tag{7.4}$$

$$Re = \frac{\rho V d_{\text{rotor}}}{\mu} \tag{7.5}$$

Some alternative non-dimensional performance parameters as discussed by Denton (2008) and Whitfield and Baines (1990) are the flow coefficient ϕ and head or loading coefficient ψ which can both be derived from the non-dimensional groups of equation 7.2. The loading coefficient is defined as $\psi = \frac{\Delta h_0}{U^2}$ and the flow coefficient is defined as $\phi = \frac{V_{\text{m}}}{U}$.

Two more parameters that are commonly used for the design of radial inflow turbines are the specific speed N_{s} and the speed ratio λ (referred to as ν in most literature). While the specific speed is rather a measure of a turbine's shape than its speed (Denton (2008)), the speed ratio is proportional to the impeller speed. Changing the impeller speed for a fixed geometry and fixed pressure ratio effectively changes the incidence on the rotor tip. Figure 7.1 shows the relationship between the speed ratio and the efficiency of a turbine. Often the speed ratio is chosen instead of the pressure ratio to draw a performance map of a turbine, as the dependency of the efficiency on the speed M_{u} is minimal in this plot.

For the design process of a radial turbine, Rohlik (1968) has come up with an optimal speed ratio for a given specific speed to achieve the peak efficiency for the given geometry (see figure 7.2).

$$N_{\text{s}} = \frac{\phi^{1/2}}{\psi^{3/4}}, \qquad \lambda = \frac{U}{\sqrt{2\Delta h_{\text{s}}}} \tag{7.6}$$

For real gases, one cannot use the ratio of specific heats as a non-dimensional parameter as it is not constant throughout the domain, but one uses the appropriate equations of state. Substitute parameters that were introduced in the previous chapters to set the gas dynamics were the isentropic exponent for the case of polytropic fluids ($\alpha_{\text{poly}} = 0$) or the Prandtl-Meyer function and fundamental derivative for the case of non-polytropic fluids ($\alpha_{\text{poly}} \neq 0$). Moreover, the previous analysis of the vanes has shown that the exit Mach number of the vane is crucial to the level of loss that is to be observed and sensitivity to real gas effects. For geometrically similar turbines, the vane exit Mach number will be fixed in the design. This

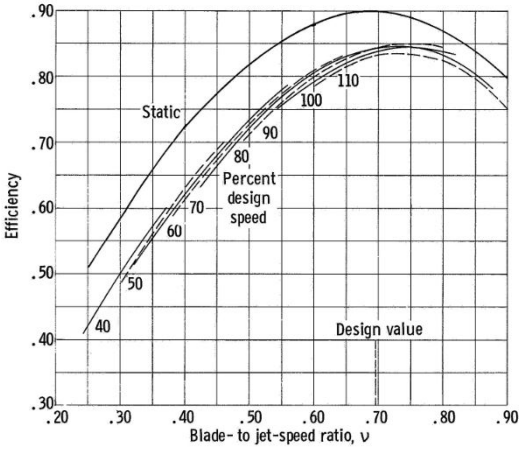

Fig. 7.1 Variation in efficiency with speed ratio (λ) (Whitfield and Baines (1990))

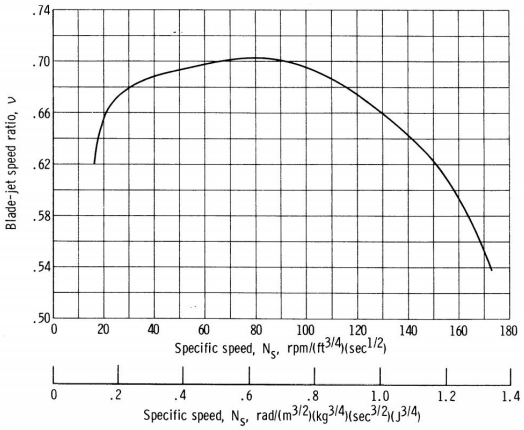

Fig. 7.2 Variation in speed ratio corresponding to maximum static efficiency with specific speed (Rohlik (1968))

yields the following proposed groups of non-dimensional parameters for radial turbine stages operating with real fluids:

$$[PR, \eta] = f(\lambda, \Theta, Re, k) \qquad \text{for: } \alpha_{\text{poly}} = 0 \tag{7.7}$$

$$[PR, \eta] = f(\lambda, \Theta, Re, \nu, \Gamma, Z) \qquad \text{for: } \alpha_{\text{poly}} \neq 0 \tag{7.8}$$

Within this chapter, the design and performance of stages for both regions will be discussed, to first show the effect of k on turbine performance and then subsequently look at the impact of Z.

7.1.1 Stage design parameters

As the baseline design, a vane exit Mach number of 1.30 was chosen in order to operate within a region where differences in the aerodynamics and loss mechanisms were to be expected. The speed ratio was not prescribed directly in the stage design tool (see Chapter 3). Instead, the velocity angles were kept fixed across all designs. This was useful as the incorporated vane design by Wheeler and Ong (2013) uses the vane exit angle and Mach number as its input. In order to achieve a specific Mach number, while maintaining specific velocity triangles, the rotational speed of the rotor was adjusted accordingly.

The two remaining non-dimensionals that were directly prescribed were the non-dimensional mass flow and Reynolds number. The Reynolds number was based on the vane exit condi-

tions, as it was the case in the previous chapters. Also, the entire stage was scaled accordingly to keep the Reynolds number constant.

The coordinates for the mid-span curve and the meridional velocity distribution were based on a previous stage design by Wheeler and Ong (2014). The velocity angles can be seen in table 7.1, whereby the rotor inlet angle was chosen in such a way that it would yield a speed ratio of ≈ 0.70. The number of blades for the vane and rotor was set to 19.

Table 7.1 Input design parameters for the stage meanline design

Design Parameters (input)		Achieved (CFD)	
		CO_2	R134a
Vane rel. inlet flow angle	0^o		
Vane rel. exit flow angle	82.5^o		
Rotor rel. inlet flow angle	-20^o		
Rotor rel. exit flow angle	-37^o		
Mach number	1.30	1.36	1.34
Mass flow (Θ)	$2.5\text{x}10^{-3}$	$2.5\text{x}10^{-3}$	$2.5\text{x}10^{-3}$
Reynolds number	$1\text{x}10^{8}$	$7.4\text{x}10^{7}$	$7.7\text{x}10^{8}$
Stage loading (Ψ)		0.9097	0.9017
Flow coefficient (Φ)		0.1334	0.1315
Non-dimensional speed (N_s)		0.3921	0.3919
Speed ratio (λ)		0.6981	0.6981
Pressure ratio		16.15	10.74

While the speed ratio is slightly higher than the one suggested by Rohlik (1968) at an equivalent non-dimensional speed, preliminary unsteady stage calculations with non-ideal fluids have shown that there appears to be a shift in the point of optimal efficiency for dense fluids. This point will be discussed in more detail at a later point of this chapter. At this point, it is also worth pointing out that this chapter aims to determine, if and how the performance is changing between the fluids for comparable stage designs. Thus, the designs represent an appropriate baseline design for this investigation.

7.1.2 Endwall design

The endwall design is part of the Meangen design program that was used to design the stages. As the coordinates of the mid-span curve are one of the inputs to Meangen, as well as the meridional velocity distribution along this curve, the passage height and thus the shape of the endwalls solely depends on the density along the mid-span curve. Specifically, the area ratio is inverse proportional to the density ratio of the stage ($\frac{A_{\text{in}}}{A_{\text{out}}} \propto \frac{\rho_{\text{out}}}{\rho_{\text{in}}}$).

In the case of designing different stages for fluids of varying k, the overall pressure ratio across the stages is changing, whereby larger values of k will lead to higher pressure ratios (see table 7.2). At the same time, the density ratio is increasing, which then defines the endwall shape.

Table 7.2 Inlet conditions for stages with varying k

fluid	p_0 [MPa]	T_0 [K]	Z	k	PR	AR
air	5	800	1.02	1.39	32.25	0.4916
CO_2	5	750	1.00	1.22	16.15	0.6523
R134a	0.5	400	0.97	1.07	10.74	0.7479

Considering the four previously used fluids (argon, air, CO_2 and R134a), the density ratio for argon (highest k) is too large to achieve a feasible endwall design. The exemplary stage designs for air, CO_2 and R134a can be seen in figure 7.3, which shows the increased passage height for the fluids of high k. The figure shows the shape of the endwalls non-dimensionalised by the radius at the rotor leading edge, though the overall size changes between fluids in order to match the Reynolds number.

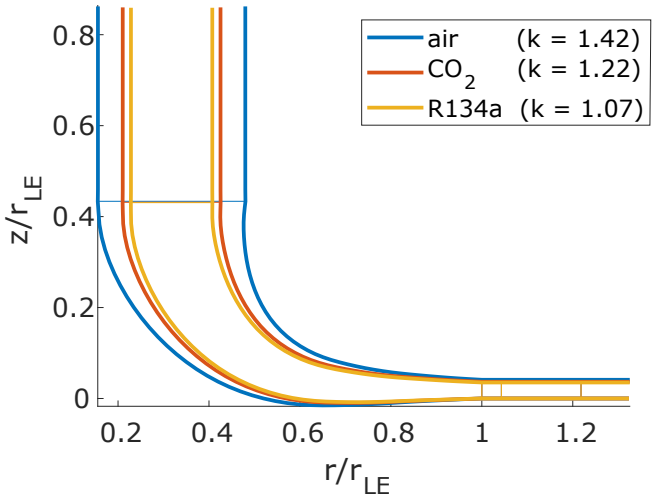

Fig. 7.3 Variation of endwalls for different isentropic exponents

Secondly, the effect of Z on the endwalls is analysed. To that end, two turbine stages are designed for R22 and RC318. These fluids that were used before with inlet conditions such that a constant Prandtl-Meyer function and fundamental derivative at the vane exit Mach number was achieved, while at the same time the average compressibility factor is varying

between 0.75 and 0.95. For these fluids, the gas dynamics are matched for the expansion occurring within the nozzle. Thus, the density ratio in this part of the stage is well matched as well. For the expansion that is happening within the rotor, the gas dynamics are not matched any more, similar to the local expansion right at the trailing edge. Hence, even though the compressibility factor itself does not affect the passage height of the rotor, the different gas dynamics within the rotor lead to slightly different endwall shapes in the rotor and thus a somewhat different area ratio of the stage (see table 7.3).

Table 7.3 Inlet conditions for stages with varying Z

fluid	p_0 [MPa]	T_0 [K]	Z	k	PR	AR
R22	5.2	413	0.75	1.04	10.97	0.7346
RC318	3.2	592	0.95	1.01	9.02	0.7892

7.2 Effect of isentropic exponent k on stage loss

In order to compare the loss that is occurring in a radial stage for different values of k, fully unsteady CFD calculations were performed for stages operating with CO_2 and with R134a. The inlet conditions for both stages are summarized in table 7.2. The isentropic exponent, computed for the expansion within the vane, is 1.22 for CO_2 and 1.07 for R134a, while the compressibility factor for both fluids is close to one.

To assess the performance of a single stage radial turbine, one usually uses the total-to-static efficiency, as the kinetic energy at the outlet is usually not recovered. The efficiencies are defined as follows:

$$\eta_{\mathrm{tt}} = \frac{h_{0,\mathrm{in}} - h_{0,\mathrm{out}}}{h_{0,\mathrm{in}} - h_{0\mathrm{s},\mathrm{out}}} \tag{7.9}$$

$$\eta_{\mathrm{ts}} = \frac{h_{0\mathrm{in}} - h_{0,\mathrm{out}}}{h_{0,\mathrm{in}} - h_{\mathrm{s},\mathrm{out}}} \tag{7.10}$$

For both fluids, the stage calculations were repeated with increased and decreased rotational speeds, to assess the sensitivity of both stages with respect to λ. Figures 7.4 and 7.5 show the computed efficiencies for the two stages operating at different rotational speeds and thus, different speed ratios. Two different features can be observed. First, the stage operating with CO_2 achieves higher efficiencies than the stage operating with R134a. Specifically, at a speed ratio of 0.70, η_{ts} is reduced from 84.7% to 83.8% for a change in k

from 1.22 to 1.07. Secondly, between the two fluids, there appears to be a shift in the optimal operating point. While for the stage operating with R134a, the optimum λ based on η_{ts} is around 0.72, the stage operating with CO_2 appears to have its optimal speed at $\lambda \approx 0.75$. Comparing the interpolated efficiency at the optimal λ, the difference in η_{ts} is even bigger, being reduced from 85.4% to 84.0% for the given change in k. These optimal values for λ are significantly higher than the proposed value by Rohlik (1968). In a multistage environment, total-to-total efficiency η_{tt} is of interest. Here, for both fluids, the optimal speed is slightly higher than for η_{ts}.

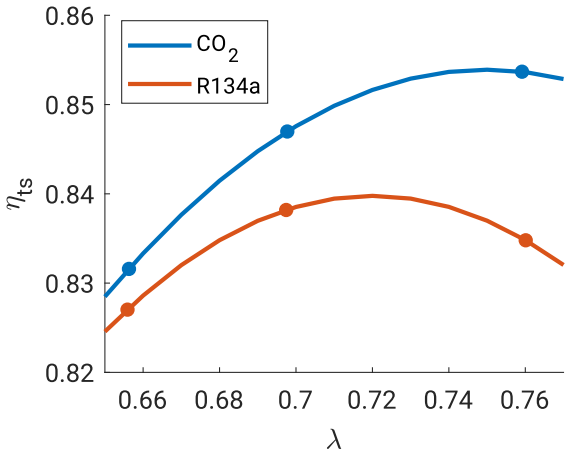

Fig. 7.4 Variation of η_{ts} with λ for CO_2 ($k = 1.22$) and R134a ($k = 1.07$)

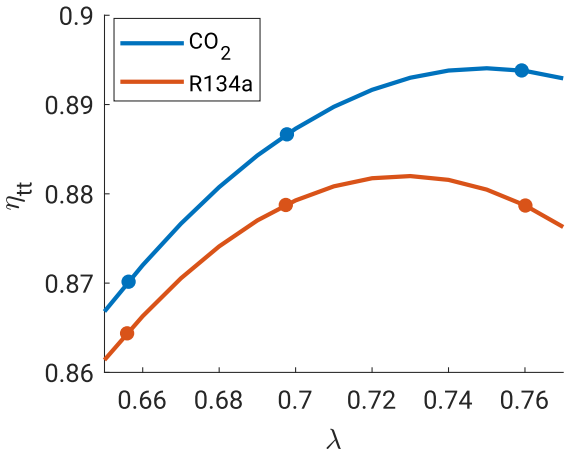

Fig. 7.5 Variation of η_{tt} with λ for CO_2 ($k = 1.22$) and R134a ($k = 1.07$)

To get an idea of the unsteadiness in the loss generation, one can look at a local loss coefficient throughout the stage. Therefore, a loss coefficient was computed on a series of meridional planes which uses the mass flow averaged properties. In this case, the loss coefficient was computed based on the local change in entropy and the temperature at the exit of the stage. Thus, this loss coefficients is defined as the amount by which it reduces the total-to-total efficiency ($\varepsilon = -\Delta\eta_{tt}$).

$$\varepsilon = \frac{T_3 \Delta s}{h_{01} - h_{03,ss}} \tag{7.11}$$

Figure 7.6 shows for the case of R134a and CO_2, at a speed ratio of 0.7, the instantaneous local loss for 26 snapshots during one rotor passage. The thick line represents the time average, and the shaded area represents the extent of the unsteady loss. Additionally, the time average mixed-out states at the vane and rotor exit are shown.

One can see that the single biggest contributor is the vane loss. This has been shown before by Wheeler and Ong (2014) that for a typical radial turbine stage, as to be found in an

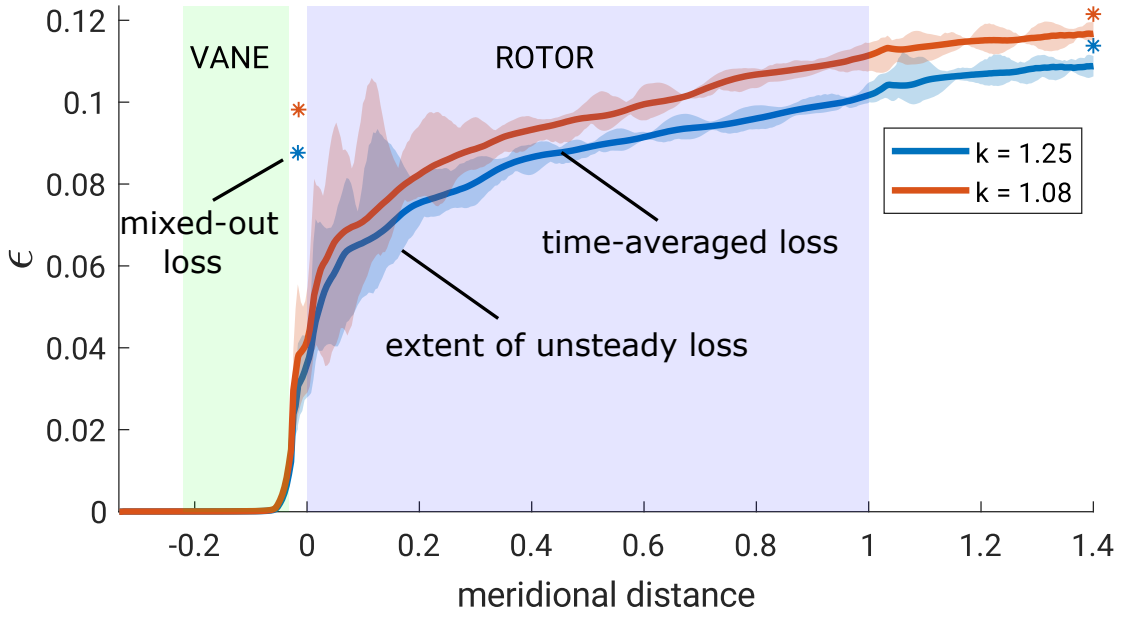

Fig. 7.6 Local loss coefficient through the stage for CO_2 ($k = 1.22$) and R134a ($k = 1.07$)

ORC turbine, the most significant fraction of the loss is generated within the vane. The most significant fluctuations in local loss are to be observed just downstream of the rotor leading edge. This is the result of vane trailing edge shock interaction with the rotor leading edge at every blade passing. The shock triggers a swing in incidence and causes flow separation. At $\lambda = 0.7$, the rotor loss coefficient of R134a is actually lower than the one of CO_2, as the difference in loss between the two fluids is reduced towards the outlet of the stage. This suggests that the interaction of the rotor with the shock might cause fewer losses for R134a.

To get a better understanding of where the differences in performance have their origin, a separate loss coefficient is computed for the vane and the rotor. Looking at the expansion process of CO_2 on an enthalpy-entropy plot shows that the largest share of the rise in entropy is within the vane (see figure 7.7). To compute the vane loss coefficient, a mixed-out state is computed at the interface between the rotor and vane. For the rotor loss coefficient, a mixed-out state is computed at the stage outlet.

$$\varepsilon_{\text{vane}} = \frac{h_{03,\text{s}} - h_{03,\text{ss}}}{h_{01} - h_{03,\text{ss}}} \tag{7.12}$$

$$\varepsilon_{\text{rotor}} = \frac{h_{03} - h_{03,\text{s}}}{h_{01} - h_{03,\text{ss}}} \tag{7.13}$$

$$\varepsilon_{\text{ke}} = \eta_{\text{tt}} - \eta_{\text{ts}} \tag{7.14}$$

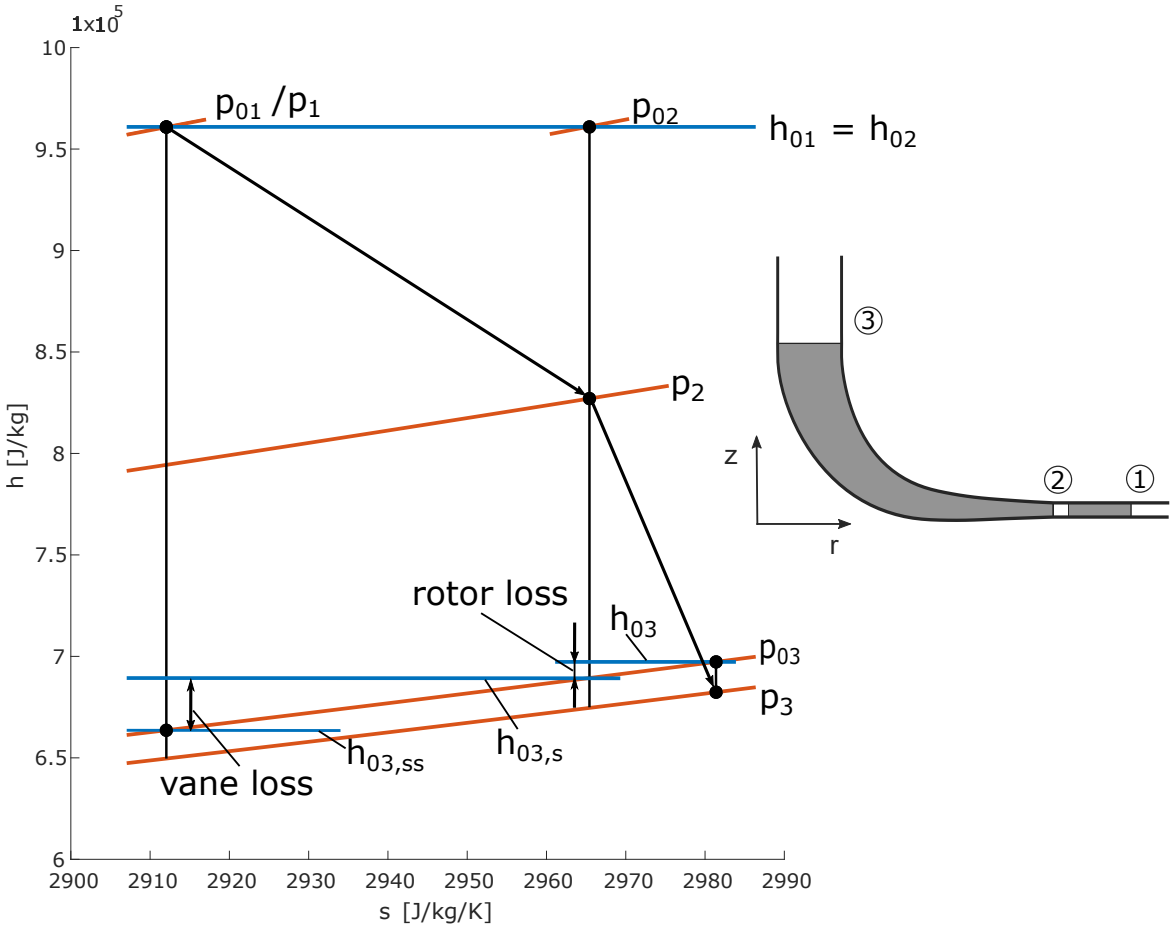

Fig. 7.7 Expansion process of CO_2 on enthalpy-entropy plot showing the vane and rotor loss

By using the mixed-out states to compute the vane loss coefficient, all the flow downstream of the vane trailing edge, which will gradually be mixed-out during the rotor passage, is accounted for in $\varepsilon_{\text{vane}}$. The unsteady loss due to the stator-rotor interaction, which occurs downstream of the interface will be considered for in $\varepsilon_{\text{rotor}}$. One additional source of loss for the radial turbine stage is the kinetic energy loss ε_{ke}. These losses occur as the kinetic energy at the exit of the stage is usually not recovered and is defined as the differences between η_{tt} and η_{ts}. The different loss coefficients for both fluids were computed for all three rotational speeds (see figure 7.8). Between all plots, the scale of the y-axis is matched. This allows to compare the sensitivity of the different loss coefficients to the speed ratio.

First, looking at the vane loss coefficient, one can see a decreased loss for a rise in speed ratio. This downward slope of the vane loss has already been discussed in Chapter 5, as changing the rotational speed effectively changes the pressure ratio that is achieved across the vane. Between the two fluids, CO_2 appears to be more sensitive to changes in the

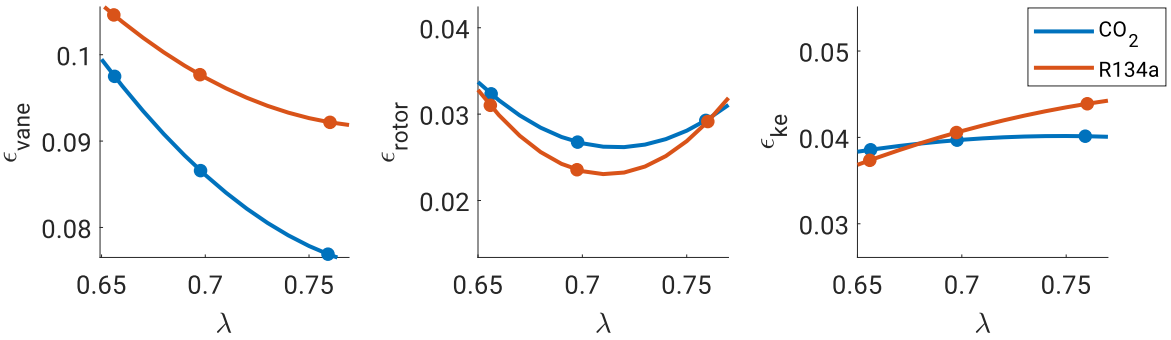

Fig. 7.8 Loss coefficients of the stage operating with CO_2 ($k = 1.22$) and R134a ($k = 1.07$)

rotational speed than R134a. Secondly, looking at the rotor loss coefficient, the parabolic shape can be explained by flow separations to either side of the rotor leading edge for large positive/negative incidence angles. Here the refrigerant appears to be more sensitive to changes in the speed ratio. Lastly, the kinetic energy losses appear to increase for greater λ for both fluids. Again, R134a seems more sensitive than CO_2.

The shift of the optimal operating point for different k becomes evident by comparing the sensitivities of the loss coefficients of CO_2 and R134a. For the case of CO_2 the vane loss, even though being smaller than the one of R134a, is more sensitive to λ. At the same time, the rotor loss and kinetic energy loss appear to be less sensitive for CO_2. This means the vane loss can be reduced more by operating at a higher rotational speed, while not increasing the two other losses as much, which then leads to an overall lower loss.

At this point it worth comparing the observed difference in vane loss to the difference that one would expect based on the previously derived correlation (5.12). At the design point of the stage ($\lambda \approx 0.7$) an average vane exit Mach number of 1.35 is achieved between CO_2 and R1343a (see table 7.1).

$$\frac{\zeta_{out}^{CO_2}}{\zeta_{out}^{air}} = a(1.22) \cdot (1.35 + 0.25) + 1.0$$
$$\frac{\zeta_{out}^{R134a}}{\zeta_{out}^{air}} = a(1.07) \cdot (1.35 + 0.25) + 1.0$$

which yields:

$$\frac{\zeta_{out}^{R134a}}{\zeta_{out}^{CO_2}} = \frac{1.17368}{1.0903} = +7.64\%$$

The predicted rise in vane loss due to k from the correlation (7.64%) is lower than the observed change in vane loss of the stage (12.74%). The reason for this discrepancy might

lay in the unsteadiness of the flow within the stage. To illustrate the highly unsteady nature of the flow, figures 7.9 and 7.10 show Mach number contours for two instantaneous snapshots taken from the simulations with CO_2 and R134a.

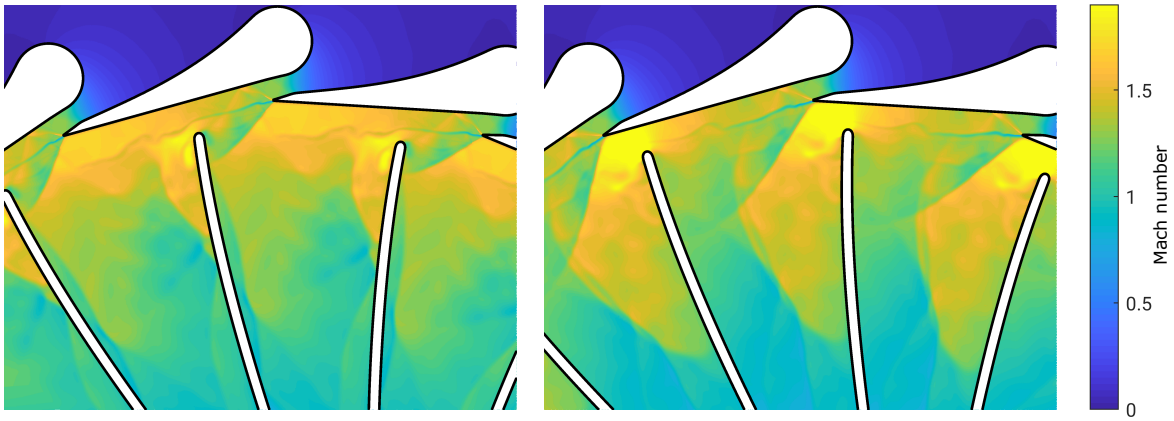

Fig. 7.9 Mach number contours for CO_2 at instantaneous snapshots

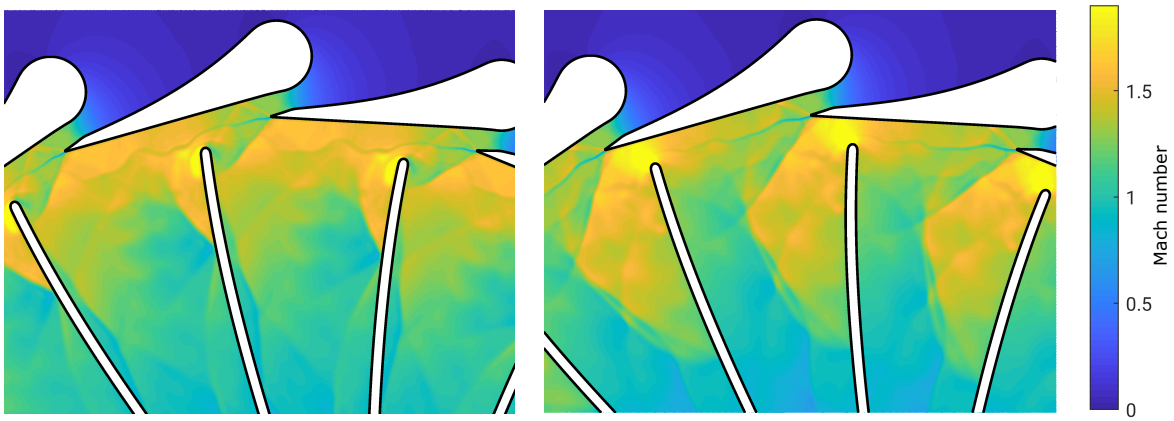

Fig. 7.10 Mach number contours for R134a at instantaneous snapshots

Every passing of the rotor leading edge has an upstream impact on the unguided expansion occurring within the vane. One can see that the flow is accelerated beyond its design Mach number along the suction side of the vane with Mach numbers peaking at around 1.7. Furthermore, there is considerable interaction between the vane and the rotor. Specifically, the shock coming off the trailing edge of the vane impinges on the leading edge of the rotor at every passage. This leads to a swing in incidence at the rotor leading edge and pressure waves that are reflected within the rotor passage. This leads to a highly unsteady loading of the rotor blade. At the same time, the vane exit Mach number, which is a key driver for the vane loss is fluctuating periodically. For both fluids, at a speed ratio of 0.7, the vane exit Mach number has been extracted for one rotor passage (see figure 7.11).

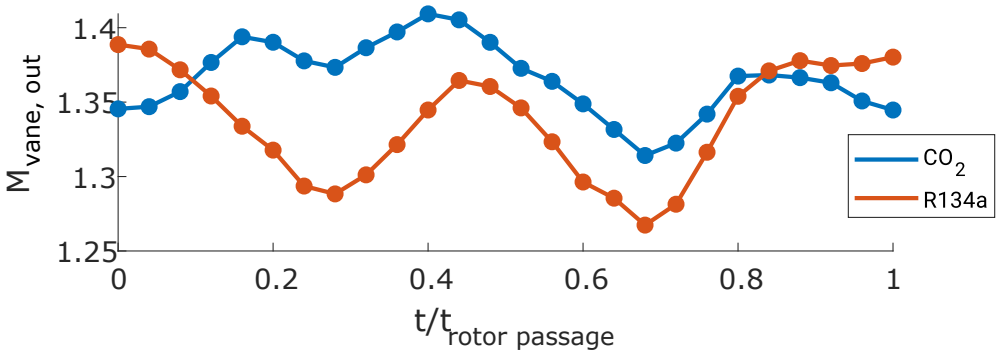

Fig. 7.11 Unsteady vane exit Mach number during one rotor passage for CO_2 and R134a

While for both fluids, there are substantial fluctuations during each rotor passage, at the design speed ratio the stage operating with CO_2 appears to have a higher vane exit Mach number. The mass flow averaged vane exit Mach numbers for all three rotational speeds are shown in table 7.4. It shows that changing the rotational speed of the rotor has a significant impact on the vane aerodynamics. Across all three operating points, the vane exit Mach number is around 2% higher for CO_2 than R134a.

Table 7.4 Mass flow averaged vane exit Mach numbers at different operating points

	$M_{\text{vane,out}}$	
λ	CO_2	R134a
0.66	1.42	1.39
0.70	1.36	1.34
0.76	1.26	1.23

To assess how the unsteady flow within the stage is affecting the vane loss, a steady CFD simulation of the isolated vane geometry was performed at the equivalent mixed-out Mach number at the vane exit. The steady flow can be compared to the time-averaged flow of the unsteady stage simulation. Contours of Mach number and entropy for CO_2 at mid-span are shown in figure 7.12, for both the steady and time-averaged simulations. It shows that unsteadiness plays a big role, as due to the unsteady interaction between the rotor and vane, the strength of the shock coming of the trailing edge is weakened.

The findings in Chapter 5 have shown, that shock losses are a strong function of the isentropic exponent and are driving to a large part the difference in vane loss due to k. Before, when the vane loss within the stage was compared between the two fluids, $\varepsilon_{\text{vane}}$ was used, which is the loss in the context of the entire stage. Though, computing the vane loss coefficient ζ_{vane} as used in the previous chapters gives a different picture. In this case, the

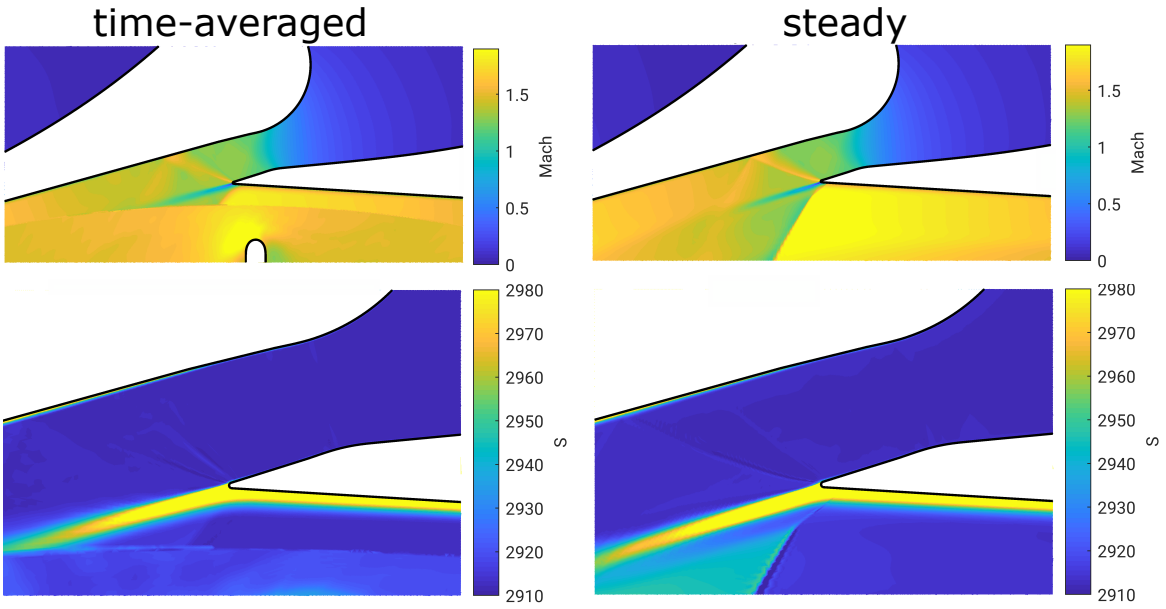

Fig. 7.12 Mach number and entropy contour for steady vane and time-averaged unsteady vane with CO_2

difference in loss between the two fluids is reduced significantly. The loss is only increased by 0.6% going from R134a ($\zeta_{\text{vane}} = 0.1966$) to CO_2 ($\zeta_{\text{vane}} = 0.1978$). This is most probably the result of the weakening of the shock loss due to the unsteadiness. At this point, it has to be noted that all unsteady interaction is highly dependent on turbine design, such as Mach number, blade count, size of the gap between vane and rotor. Thus, these findings are very specific to the underlying design.

In order to understand this significant difference between ζ_{vane} and $\varepsilon_{\text{vane}}$, one can look at figure 7.7. Both loss coefficients are based on the same change in entropy, but the gradient of the iso-bars of P_2 (ζ_{vane}) and P_{03} ($\varepsilon_{\text{vane}}$) is changing. The gradient of the iso-bars is dependent on the thermodynamic properties of the fluid, specifically on the temperature ratio (T_2/T_{03}) within the stage. This is also reflected in the relationship between $\varepsilon_{\text{vane}}$ and ζ_{vane}.

$$\varepsilon_{vane} \approx \frac{T_{03}}{T_2} \cdot \zeta_{\text{vane}} \cdot \left(\frac{V_{2s}}{U} \cdot \lambda \right)^2 \tag{7.15}$$

In this case, the stage operating with CO_2 shows a greater temperature ratio (1.2478) than the stage operating with R134a (1.0955). This leads to a flatter iso-bar of the outlet pressure for CO_2 (higher k) compared to R134a (lower k), which then, in turn, results in a lower $\varepsilon_{\text{vane}}$.

Based on the equation 7.15, one can make out what the different contributions to the change in vane loss $\varepsilon_{\text{vane}}$ are.

$$\frac{\varepsilon_{\text{vane,R134a}}}{\varepsilon_{\text{vane,CO}_2}} = \frac{\text{TR}_{\text{R134a}}}{\text{TR}_{\text{CO}_2}} \cdot \frac{\zeta_{\text{vane,R134a}}}{\zeta_{\text{vane,CO}_2}} \cdot \frac{\Pi_{\text{R134a}}}{\Pi_{\text{CO}_2}}$$

where:

$$\Pi = \left(\frac{V_{2s}}{U} \cdot \lambda \right)^2$$

This shows that the given $\Delta\varepsilon$ of +12.9% is the result of $\Delta\zeta$ = +0.6%, ΔTR = +12.9% and $\Delta\Pi$ = -1.5%. Therefore, the sensitivity of the loss of the vane to the overall performance of the turbine is a strong function of the temperature ratio, which will be lower for lower values of k. The difference in Π, between the two fluids, is the results of the two turbines not operating right at the design point.

Now looking at the rotor loss coefficient (see figure 7.8), one can see that at the design speed ratio of 0.7, the rotor loss $\varepsilon_{\text{rotor}}$ is actually lower for the refrigerant. This suggests that the interaction of the rotor with the shock might cause fewer losses for R134a. In order to see if this is reflected in the secondary flows of the rotor, a local loss coefficient is computed on the outlet plane of the rotor. Figure 7.13 shows contours of the time-averaged loss in the relative frame of the rotor.

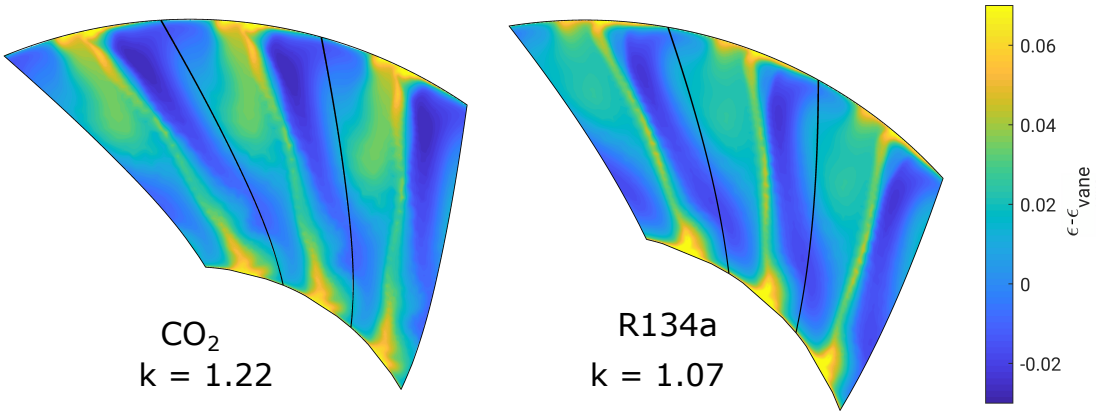

Fig. 7.13 Contours of loss at the rotor exit plane at $\lambda = 0.7$ for CO_2 and R134a

For radial turbines, it has been demonstrated before by Zangeneh-Kazemi et al. (1988), that the low momentum fluid is driven towards the shroud by the secondary flows that develop due to the streamwise curvature. This can be observed for both fluids. While the contours

of loss generally appear to be quite similar, there are differences in the loss cores close to the hub and casing, which ought to be the driver for the observed variation in rotor loss. The detailed impact of k on the three-dimensional flow within the rotor that leads to this difference represents possible future work.

A side-by-side comparison of the loss coefficient at a fixed speed ratio of 0.7 for both fluids is shown in figure 7.14. It can be said, that similar to the case of a vane, the performance of a stage operating with a fluid of lower isentropic exponent k will be reduced.

This is primarily driven by vane loss which accounts for roughly 58% of the overall loss. Three factors drive the difference in vane loss itself. First, the steady loss mechanisms which are affected by k as discussed in Chapter 5. Secondly, the unsteadiness of the flow is affecting the loss is to a large extent. Lastly, the thermodynamic properties (temperature ratio) will affect how the entropy generation in the vane affects the overall performance of the stage. This is why changes made to the vane loss are driving the overall performance of the stage. Thus, the actual reduction of rotor loss (-12%) for reducing k from 1.22 to 1.07, does not alter the overall trend as the rotor only accounts for about 16% of the total loss. Furthermore, the kinetic energy loss is again behaving the opposite way, whereby ε_{ke} is increased (+2%) for decreasing k.

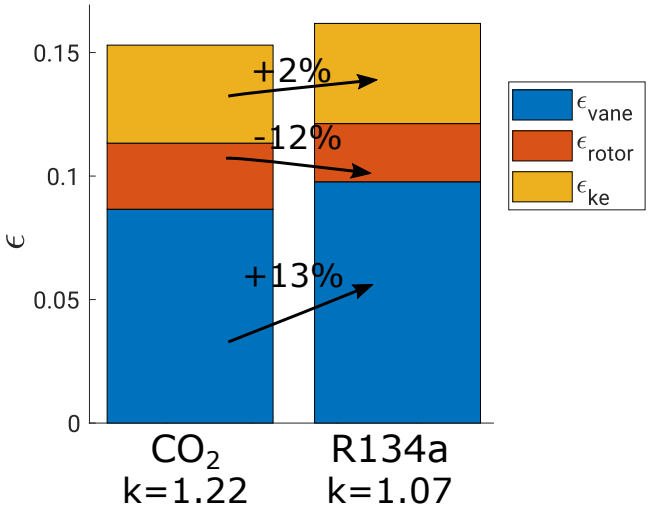

Fig. 7.14 Change in loss coefficients at $\lambda = 0.7$ for CO_2 and R134a

Interestingly, the difference in kinetic energy loss due to k would be even bigger if both stages were to operate at the same efficiency. The kinetic energy loss can easily be computed with the meanline design tool by supplying the correct total-to-total efficiency. Figure 7.15 shows that if the stages were to operate at a fixed efficiency, the kinetic energy losses would be roughly twice as high as with operating at the actual efficiencies.

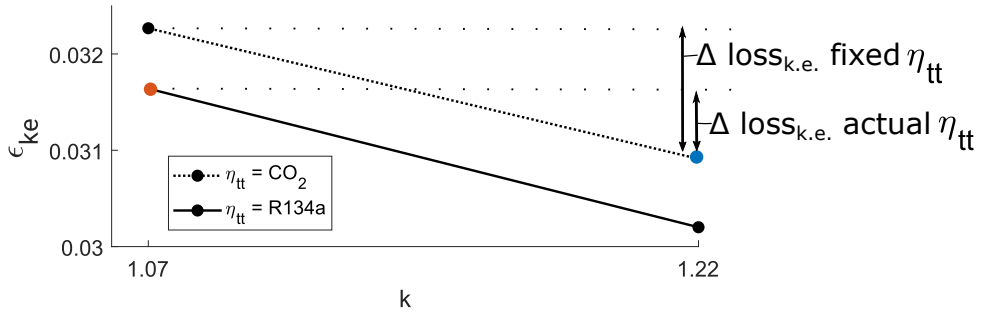

Fig. 7.15 Change in kinetic energy loss at $\lambda = 0.7$ for CO_2 and R134a

7.3 Effect of compressibility factor Z on stage loss

This section will look at two stages operating with R22 and RC318, where the average Z across the expansion of the vane varies between 0.75 and 0.95 (see table 7.3). The inlet conditions were chosen in such a way that the gas dynamics are matched for the expansion within the nozzle. Based on the vane calculations with the same fluids in the previous chapter, one can expect a certain discrepancy in the vane loss due to the reported effect of Z on the viscous losses and the difficulty of simultaneously matching the gas dynamics in the nozzle and for the greater local expansions at the trailing edge. While the pressure ratio in the vane is matched between the fluids, the pressure ratio across the stage is varying between 9.02 and 10.97. This is another indicator that the flow in the rotor passage will show a certain discrepancy.

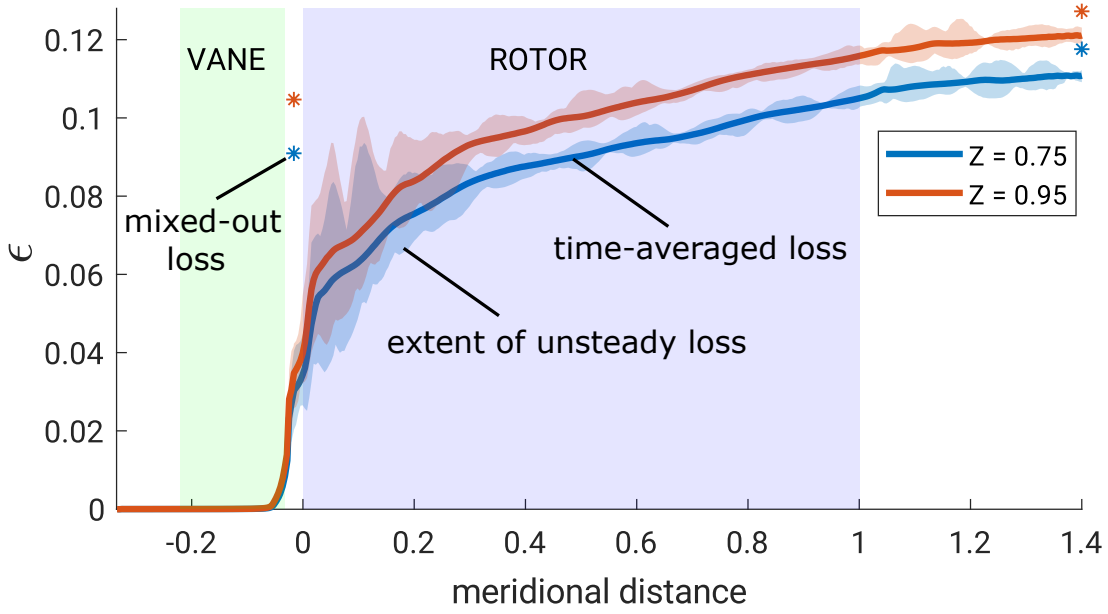

Fig. 7.16 Local loss coefficient through the stage for R22 ($Z = 0.75$) and RC318 ($Z = 0.95$)

In this case, unsteady calculations were only performed at one rotational speed, at a speed ratio of 0.7. The local loss computed along the meridional coordinate is shown for both fluids in figure 7.16. As to be expected, the loss that occurs in the vane is higher for the stage operating with RC318 with the higher Z. The reason for this difference was the subject of the previous chapter. Looking at the mixed-out loss at the outlet of the stage reveals that the differences in loss between the two fluids appear to be reduced in the rotor passage.

The detailed loss analysis for both fluids is shown in figure 7.17. As before the vane loss is the most significant contributor to the overall loss with 56%-61% for the two fluids. Hence, as for the case of k, the differences that are present in the vane drive the overall performance of the stage. Here, the vane loss $\varepsilon_{\text{vane}}$ is reduced by -14.9%, for the given reduction in Z. In the rotor passages, the loss is actually increasing for R22 with a lower value of Z by -16.5%. The change in the kinetic energy loss is rather insignificant with +1% going from low to high Z. All in all, the stage loss is dropping by 5.6% between RC318 ($Z = 0.95$) and R22 ($Z = 0.75$), which yields a shift in total-to-static efficiency from 82.96% to 83.91%.

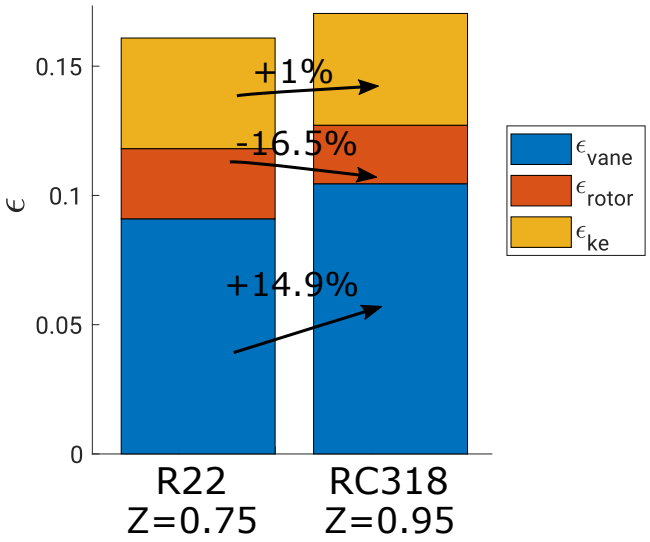

Fig. 7.17 Change in loss coefficients at $\lambda = 0.7$ for R22 and RC318

The observed reduction in vane loss is significantly bigger than the previously observed effect of Z in the vane-alone calculations. In the vane-alone calculations, the performance of the vane was analysed at the design Mach number of the vane ($M_{\text{design}} = 1.30$). For the case of the stage calculations, the time-averaged Mach number at the outlet of the vane is around 1.33 for R22 and 1.28 for RC318. At these varying Mach numbers, the difference in loss ζ_{vane} is expected to be greater between the two fluids. Looking at the CFD results of the 2D vane of the same two fluids, one can extrapolate the data to the corresponding Mach numbers (see figure 7.18).

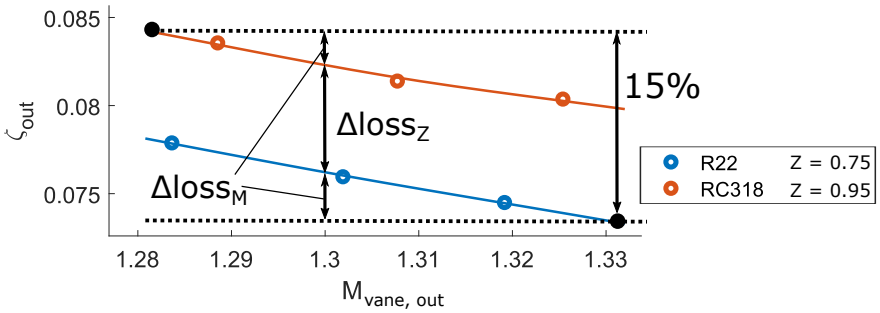

Fig. 7.18 Extrapolated 2D vane loss at corresponding Mach numbers

The figure shows that when the change in Mach number is accounted for a $\Delta\zeta_{vane}$ of 15% is to be expected based on the simplified 2D steady vane simulation. Computing ζ_{vane} for the vanes in the unsteady stage gives a $\Delta\zeta_{vane}$ of +2.3%. This shows, as for the two stages with varying k, the unsteadiness appears to have a significant impact on the steady loss mechanism that were found in Chapter 6. Again, there is a considerable difference in temperature ratio (T_2/T_{03}) between the two fluids (TR_{R22}=1.1794, TR_{RC318}=1.0378). Hence, we can work out that the given $\Delta\varepsilon$ of +14.9% is the result of $\Delta\zeta$ = +2.3%, ΔTR = +13.6% and $\Delta\Pi$ = -1.1%.

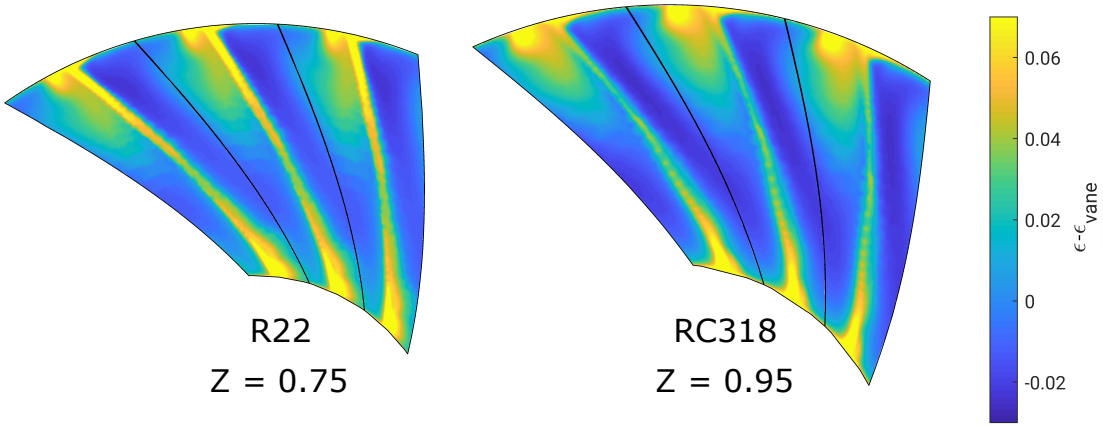

Fig. 7.19 Contours of loss at the rotor exit plane at $\lambda = 0.7$ for R22 and RC318

Again contours of the local loss coefficient at the rotor exit plane are computed (see figure 7.19). The loss within the wake appears to be much more prominent for the case of R22 than for RC318, which probably drives the difference in rotor loss. At the same time, there is also a considerable difference in the loss cores close to the shroud between the two fluids. It is difficult to say how much of the change in the rotor is either due to Z or due to diversion of the gas dynamics in this part of the stage. Once one is operating with inlet conditions where $Z \ll 1$, it is very challenging to fully decouple Z from the underlying gas dynamics in the

entire turbine stage. As before a detailed investigation of the impact of Z on the 3D flow within the rotor passage remains within the scope of possible future work.

7.4 Summary

Unsteady stage calculations with working fluids at different values of isentropic exponent and compressibility factor have shown that for such highly loaded radial turbines, the total-to-static efficiency will be affected.

For a change in isentropic exponent form 1.21 to 1.07, the total-to-static efficiency drops by about one percentage point if all other non-dimensional parameters are accounted for. This is primarily driven by the rise in loss in the vane due to the reduction in k. Comparing the given rise in vane loss to the previous findings in Chapter 5 based on steady two-dimensional vane calculations revealed, that unsteadiness is an essential factor that affects the vane loss. Specifically, the unsteadiness appears to reduce the trailing edge loss. Though, the effect of unsteadiness will be unique to every turbine design. Furthermore, the importance of vane loss on overall stage efficiency is significantly affected by the temperature ratio in the rotor, which tends to be lower for low k. A low temperature ratio leads to entropy generation in the vane having more importance to overall stage efficiency.

Similarly, a given change in Z from 0.75 to 0.95, leads to a change in total-to-static efficiency of one percentage point, primarily due to the impact Z has on the vane loss as discussed in the previous chapter. Furthermore, the comparison to the steady vane calculations indicates that the impact of unsteadiness is again very significant for the turbine design that was analysed in this chapter.

Thus it can be said that the sensitivities of unsteady loss mechanisms are also very sensitive to the selected working fluid.

Chapter 8

Conclusions

A new experimental test rig has been designed and manufactured, which allows the testing of transonic turbine stator vanes with a variety of working fluids and all desirable inlet conditions. Detailed static pressure measurements have been taken at the wall for a vane with a design Mach number of 1.45. The isentropic exponent of the tested fluids ranged from 1.08 to 1.67 and the compressibility factor was in the range of 1.0 to 0.88. Additionally, a wedge probe has been designed to be able to measure the wake downstream of the vane in the supersonic flow field. These detailed measurements are the first of their kind in the open-source literature.

The experimental results have been used to validate the computational approach that has been used for further analysis of this thesis. As such the research questions formulated at the beginning of the thesis could be answered.

How do gas properties affect turbine aerodynamics?

For the case of supersonic flow, it has been shown that both k and Z have a noticeable impact on turbine aerodynamics. First, the aerodynamics are influenced by k through the nozzle shape, that needs to be adapted to generate the same Mach number and through the flow around the trailing edge. Specifically, the fluid of lower k or Γ will lead to a greater turning around the trailing edge due to a change in the Prandtl-Meyer function of such fluids. Overall the impact of the isentropic exponent k on aerodynamics is of inviscid nature. The compressibility factor Z on the other hand only has an impact on the aerodynamics in the viscous region. The CFD has shown, that a low value of Z affects the growth of the boundary layer thickness if all other non-dimensionals (ν and Γ) are kept constant. For two fluids of at matched conditions, a reduction in Z results in a rise in displacement thickness while

simultaneously the momentum and energy thickness are being reduced. This trend has been observed across a multitude of different turbulence model and hence independent of such choice.

What is the impact on loss?

The first computational study was aimed at exploring the effect of the isentropic exponent k on turbine performance. The analysis has shown that the loss that arises within the vane is a strong function of the isentropic exponent when operating at exit Mach numbers higher than 0.9. Over the range of conditions tested in this study, the vane loss varied as much as 20-35%. The sensitivity of loss to k constitutes to increase as vane exit Mach numbers rise.

Furthermore, the effect of the compressibility factor Z on turbine performance has been tested. While it is usually almost impossible to single out the impact of Z by itself, it was shown that low values of Z lead to lower losses. For the conditions tested in this thesis, a reduction of about 8% was observed. Simulations of a flat have indicated that the effect of Z on loss is strong function of Mach number as well. Specifically, the beneficial effect of low Z is reduced for low Mach numbers.

Which loss mechanisms are most affected by these gas properties?

The changes in loss due to the isentropic exponent are driven by a combination of a change in shock loss within the blade passage and a change in mixing loss downstream of the blade trailing edge. Such mechanisms are an inherent effect of the isentropic exponent on fundamental principles of conservation and are thus inviscid in nature.

Regarding the effect of the compressibility factor on loss, there are two aerodynamic mechanisms which drive this reduction of loss. First, there is a reduction in shock losses and secondly a reduction in the boundary layer loss.

How can this be accounted for in future turbine design?

It has been shown that the loss mechanisms affected by the isentropic exponent are of an inviscid nature. As such, these effects will be essential to consider for future high-work turbines and turbines operating at conditions where isentropic exponents may be reduced (due to real-gas and/or high-temperature effects). To that end, a correlation was obtained to be able to account for these changes in loss relative to air across all Mach numbers (see equation 5.12).

The compressibility factor has shown to reduce loss for low for low values of Z. It will be challenging to make use of these beneficial effects of Z in actual turbine applications, as generally, low compressibility factors are to be found in regions of low isentropic exponent. In certain flow conditions, this might counteract the adverse effects of k to some degree. Though, the overall sensitivity of loss towards k remains higher than the sensitivity to Z. If a turbine designer changes the working fluid from CO_2 to a refrigerant, this means that the isentropic exponent is reduced by 15% from 1.27 to 1.08. Such a reduction in k would yield a 9.5% rise in loss at an operating Mach number of 1.30. A change in compressibility factor of similar degree (1.0 to 0.85) would be equivalent to a change in pressure from 0.1 MPa to 8.25 MPa for the case of CO_2 at $T = 400$ K. Say all other non-dimensionals are accounted for, changing Z from 1.0 to 0.85 would yield a 5.3% reduction in loss.

Additionally, fully unsteady stage calculations have been performed, which have highlighted that for high-pressure radial turbines, the single biggest contributor to the overall loss of the stage is the vane. At the same time, the vane is the region of the stage, which will be most affected by k and Z due to the high relative Mach numbers. Comparing the unsteady vane loss to the previous steady vane calculations have shown, that unsteadiness has a high impact on vane loss. Thus, unsteadiness plays a big role in the sensitivity of choice in working fluid. Furthermore, this has highlighted the need for unsteady CFD to correctly predict the efficiency of a turbine. In the context of the entire turbine, the changes in the vane loss only lead to a one percentage point change in total-to-static efficiency for the conditions tested here. A one percentage point change in efficiency for rather significant changes in k and Z means that changes in k and Z are almost of second-order compared to the traditional non-dimensional turbine parameters. The turbine designer who wants to change the working fluid while maintaining efficiency has to make sure to match the right non-dimensional parameters. The really difficult challenge is to ensure the matching of the 'classic' non-dimensionals. To ensure dynamic similarity, the turbine designer has to match the behaviour of the Prandtl-Meyer function across the range of Mach numbers that are occurring within the turbine.

8.1 Future work

The effect of Z on the boundary layer

The isolated analysis of the effect of Z on the boundary layer (see figure 6.26) suggested that the loss is a strong function of Mach number. Thus, it would be worth extending the study

of Z to a broader range of vane exit Mach numbers to determine how the loss sensitivity is changing with Mach number. Furthermore, one could look at a greater variety of Z to determine if loss scales linearly with Z.

The analysis has also revealed that Z has an impact on the growth of the boundary layer. While this effect has shown to exist across all turbulence models, it would be well worth to repeat the analysis with high-fidelity CFD (LES, DNS) to get an understanding of the physics of the mechanisms driving these differences. At the same time, one could explore the shock-boundary layer interaction using high-fidelity simulations.

Real gas effects in 3D aerodynamics

The unsteady stage calculations have shown that there are differences in the rotor loss between fluids of varying k and Z. These occur in the wake and secondary flows. Exploring the impact of real gas effects on 3D flows would be an important area for future work.

Real gas effects in unsteady loss mechanism

The unsteady stage calculations have also revealed that unsteadiness is affecting the loss in the vane significantly. In the studied case, the trailing edge loss was reduced compared to some comparable steady simulations. It would be of high interest, to explore these mechanisms in detail and to see how their sensitivity is changing with turbine design (Mach number, gap size, etc.).

Application to supercritical fluids

Supercritical CO_2 cycles are becoming more popular in recent years. Looking at contours of k and Z for CO_2 (figure 8.1) reveals that the isentropic exponent can be increased by operating at supercritical inlet conditions.

The figure shows k can vary from 1.2 to 1.8, and Z varies from 0.7 to 1.5. This work would suggest these variations in k and Z significantly alter both the stage design and performance. Future work on the effects of k and Z at supercritical conditions will be important for sCO_2 and supercritical ORC systems.

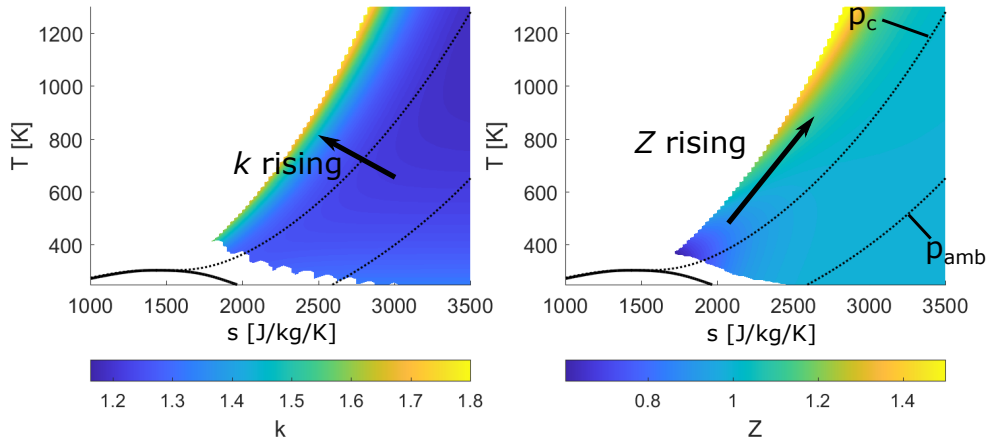

Fig. 8.1 Contours of k and Z on T-s diagram for CO_2 ($M = 1.3$)

References

Ainsworth, R., Miller, R., Moss, R., and Thorpe, S. (2000). Unsteady pressure measurement. *Measurement Science and Technology*, 11(7):1055.

Arts, T., de Rouvriot, M. L., and Rutherford, A. W. (1990). Aero-thermal investigation of a highly loaded transonic linear turbine guide vane cascade: A test case for inviscid and viscous flow computations. Technical report, Von Karman Institute Technical Note 174.

Colonna, P., Casati, E., Trapp, C., Mathijssen, T., Larjola, J., Turunen-Saaresti, T., and Uusitalo, A. (2015). Organic rankine cycle power systems: from the concept to current technology, applications, and an outlook to the future. *Journal of Engineering for Gas Turbines and Power*, 137(10):100801.

Cramer, M. S. and Crickenberger, A. B. (1992). Prandtl-meyer function for dense gases. *AIAA Journal*, 30:561–564.

Denton, J. (1993). The 1993 igti scholar lecture: Loss mechanisms in turbomachines. *Journal of Turbomachinery*, 115(4):621–656.

Denton, J. D. (2008). *Lecture Notes Turbomachinery Cambridge. Introductory Review of Basic Principles*, volume Volume 1.

Denton, J. D. (2017). Multall: An open source, cfd based, turbomachinery design system. In *ASME Turbo Expo 2017: Turbomachinery Technical Conference and Exposition*. American Society of Mechanical Engineers Digital Collection.

Denton, J. D. and Xu, L. (1990). The trailing edge loss of transonic turbine blades. *Journal of Turbomachinery*, 112:277–285.

Dostal, V., Hejzlar, P., and Driscoll, M. J. (2006). High-performance supercritical carbon dioxide cycle for next-generation nuclear reactors. *Nuclear Technology*, 154 (3):265 – 282.

Durá Galiana, F. J., Wheeler, A., Ong, J., and de M. Ventura, C. A. (2017). The effect of dense gas dynamics on loss in orc transonic turbines. *Journal of Physics: Conf. Series*, 821.

Fluent, A. (2016). 17.0 user's guide. *Ansys Inc*.

Galiana, F. J. D., Wheeler, A. P., and Ong, J. (2016). A study of trailing-edge losses in organic rankine cycle turbines. *Journal of Turbomachinery*, 138(12):121003.

Greitzer, E. M., Tan, C. S., and Graf, M. B. (2007). *Internal flow: concepts and applications*, volume 3. Cambridge University Press.

Hall, I. (1962). Transonic flow in two-dimensional and axially-symmetric nozzles. *The Quarterly Journal of Mechanics and Applied Mathematics*, 15(4):487–508.

Kouremenos, D. A. and Kakatsios, X. K. (1985). The three isentropic exponents of dry steam. *Forschung im Ingenieurwesen A*, 51(5):117–122.

Kyprianidis, K. G., Sethi, V., Ogaji, S. O. T., Pilidis, P., Singh, R., and Kalfas, A. I. (2011). Uncertainty in gas turbine therm-fluid modelling and its impact on performance calculations and emissions predictions at aircraft system level. *Proceedings of the Instituion of Mechanical Engineers, Part G: Journal of Aerospace Engineering*, 226 (2).

Lazzaretto, A. and Manente, G. (2014). A new criterion to optimize orc design performance using efficiency correlations for axial and radial turbines. *International Journal of Thermodynamics*, 17(3):192–200.

Lemmon, E. W., Huber, M. L., and McLinden, M. O. (2010). *NIST Standard Reference Database 23: Reference Fluid Thermodynamic and Transport Properties-REFPROP, Version 9.0,*. National Institute of Standards and Technology,Standard Reference Data Program, Gaithersburg, 2010.

Lemmon, E. W. and Span, R. (2006). Short fundamental equations of state for 20 industrial fluids. *Journal of Chemical Engineering Data*, 51:785–850.

Macchi, E. and Astolfi, M. (2016). *Organic Rankine Cycle (ORC) Power Systems: Technologies and Applications*. Woodhead Publishing.

Macchi, E. and Perdichizzi, A. (1981). Efficiency prediction for axial-flow turbines operating with nonconventional fluids. *Journal of engineering for power*, 103(4):718–724.

Manente, G. and Lazzaretto, A. (2012). Compressibility factor as evaluation parameter of expansion processes in organic rankine cycles. In *ECOS2012-the 25 th International Conference on Efficiency, Cost, Optimization and Simulation of Energy Conversion Systems and Processes*.

Moran, M. J. and Shapiro, H. (2014). Fundamentals of engineering thermodynamics.

No, H. C., Kim, J. H., and Kim, H. M. (2007). A review of helium gas turbine technology for high-temperature gas-cooled reactors. *Nuclear Engineering and Technology*, 39 (1).

Paradissiadis, I. (1987). The three isentropic exponents of wet steam. *Forschung im Ingenieurwesen A*, 53(5):159–161.

Perdichizzi, A. and Lozza, G. (1987). Design criteria and efficiency prediction for radial inflow turbines. *ASME Paper*, (87-6T):231.

Rinaldi, E., Pecnik, R., and Colonna, P. (2016). Unsteady operation of a highly supersonic organic rankine cycle turbine. *Journal of turbomachinery*, 138(12).

Rogers, G. F. C. and Mayhew, Y. R. (1992). *Engineering Thermodynamics: Work and Heat Transfer*. Pearson.

Rohlik, H. E. (1968). Analytical determination of radial inflow turbine design geometry for maximum efficiency. Technical report, NASA Technical Note TN D-4384.

Saravanamutto, H. I. H., Rogers, G. F. C., Cohen, H., and Straznicky, P. V. (2009). *Gas Turbine Theory*. Pearson Education.

Sciacovelli, L. and Cinnella, P. (2014). Numerical study of multistage transcritical organic rankine cycle axial turbines. *Journal of engineering for gas turbines and power*, 136(8).

Sieverding, C., Arts, T., Dénos, R., and Brouckaert, J.-F. (2000). Measurement techniques for unsteady flows in turbomachines. *Experiments in fluids*, 28(4):285–321.

Span, R. and Wagner, W. (2003). Equations of state for technical applications. ii. results for nonpolar fluids. *International Journal of Thermophysics*, 24(1):41–109.

Staff, A. R. (1953). Equations, tables, and charts for compressible flow. *NACA Report*, 1135.

Stijepovic, M. Z., Linke, P., Papadopoulos, A. I., and Grujic, A. S. (2012). On the role of working fluid properties in organic rankine cycle performance. *Applied Thermal Engineering*, 36:406–413.

Thompson, P. A. (1971). A fundamental derivative in gas dynamics. *Physics of Fluids*, 14(9):1843–1849.

Tillner-Roth, R. and Baehr, H. D. (1994). An international standard formulation for the thermodynamic properties of 1,1,1,2 tetrafluoroethane (hfc-134a) for temperatures from 170 k to 455 k and pressures up to 70 mpa. *Journal of Physical and Chemical Reference Data*, 23(5):657 – 729.

v17.0, A. F. (2015). Ansys fluent v17.0 [software]. Technical report, Canonsburg,PA.

Wheeler, A. and Ong, J. (2013). The role of dense gas dynamics on orc turbine performance. *Journal of Engineering for Gas Turbines and Power*, 135.

Wheeler, A. P. and Ong, J. (2014). A study of the three-dimensional unsteady real-gas flows within a transonic orc turbine. *ASME Paper No. GT2014-25475*.

Whitfield, A. and Baines, N. C. (1990). Design of radial turbomachines.

Zangeneh-Kazemi, M., Dawes, W., and Hawthorne, W. (1988). Three dimensional flow in radial-inflow turbines. In *Turbo Expo: Power for Land, Sea, and Air*, volume 79184, page V001T01A046. American Society of Mechanical Engineers.

Zhang, L., Zhang, W. Z. Y., and Chen, T. (2017). Similarity theory based radial turbine performance and loss mechanism comparision between r245fa and air for heavy-duty diesel engine organic rankine cycles. *Entropy*, 19 (1).

Appendix A

List of REFPROP fluids

The following list includes all fluids that have been used in the analysis of chapter 6.

Table A.1 List of fluids in REFPROP by Lemmon et al. (2010)

Name	Synonym	Chemical Formula
1,3-Butadiene	Vinylethylene	C4H6
Butene	1-Butylene	C4H8
1-Butyne	Ethylacetylene	C4H6
1-Pentene	Propylethylene	C5H10
2,2-Dimethylbutane	Neohexane	C6H14
2,3-Dimethylbutane	Butane, 2,3-dimethyl-	C6H14
3-Methylpentane	Pentane, 3-methyl-	C6H14
Acetone	Dimethyl ketone	C3H6O
Acetylene	Narcylen, vinylene	C2H2
Ammonia	R-717	NH3
Argon	R-740	Ar
Benzene	Benzene	C6H6
Butane	R-600	C4H10
Undecane	n-Undecane	C11H24
Dodecane	n-Dodecane	C12H26
Hexadecane	n-Hexadecane	C16H34
Methylcyclohexane	Cyclohexylmethane	C7H14
Docosane	n-Docosane	C22H46
cis-Butene	(Z)-2-Butene	C4H8
Propylcyclohexane	Propylcyclohexane	C9H18
Perfluorobutane	Perfluorobutane	C4F10
Perfluoropentane	Perfluoropentane	C5F12
Perfluorohexane	Perfluorohexane	C6F14

Table A.2 List of fluids in REFPROP by Lemmon et al. (2010)

Name	Synonym	Chemical Formula
R13I1	HFC-13I1	CF3I
Chlorine	Chlorine	Cl2
Chlorobenzene	Phenyl chloride	C6H5Cl
Carbon monoxide	Carbon oxide	CO
Carbon dioxide	R-744	CO2
Carbonyl sulfide	Carbon oxysulfide	COS
Cyclobutene	Cyclobutan-1,2-diyl	C4H6
Cyclohexane	Cyclohexane	C6H12
Cyclopentane	C5H10	C5H10
Cyclopropane	Trimethylene	C3H6
Deuterium	Deuterium	D2
Heavy water	Deuterium oxide	D2O
D4	D4	C8H24O4Si4
D5	D5	C10H30O5Si5
D6	D6	C12H36Si6O6
Diethanolamine	bis(2-hydroxyethyl)Amine	C4H11NO2
Decane	n-Decane	C10H22
Diethyl ether	Ethyl ether	C4H10O
Dimethyl carbonate	DMC	C3H6O3
Dimethyl ether	RE-170	C2H6O
Ethylbenzene	Benzene, ethyl-	C8H10
Ethylene glycol	Glycol alcohol	C2H6O2
Ethane	R-170	C2H6
Ethanol	Methyl carbinol	C2H6O
Ethylene	R-1150	C2H4
Ethylene oxide	Oxirane	C2H4O
Fluorine	Fluorine	F2
Hydrogen sulfide	Dihydrogen monosulfide	H2S
Hydrogen chloride	Hydrogen chloride	HCl
Helium	R-704	He
Heptane	n-Heptane	C7H16
Hexane	n-Hexane	C6H14
Hydrogen (normal)	R-702	H2
Isobutene	Methylpropene	C4H8
Isohexane	Methylpentane	C6H14
Isooctane	Isobutyltrimethylmethane	C8H18
Isopentane	R-601a	C5H12
Isobutane	R-600a	C4H10
Krypton	R-784	Kr
MD2M	MD2M	C10H30Si4O3
MD3M	MD3M	C12H36Si5O4
MD4M	MD4M	C14H42O5Si6
MDM	MDM	C8H24O2Si3

Table A.3 List of fluids in REFPROP by Lemmon et al. (2010)

Name	Synonym	Chemical Formula
Monoethanolamine	2-Aminoethanol	C2H7NO
Methane	R-50	CH4
Methanol	Methyl alcohol	CH4O
Methyl linoleate	Methyl ester(Z,Z)-9,12-octadecadienoic acid	C19H34O2
Methyl linolenate	Methyl ester linolenic acid	C19H32O2
MM	MM	C6H18OSi2
Methyl oleate	Methyl ester oleic acid	C19H36O2
Methyl palmitate	Methyl ester palmitic acid	C17H34O2
Methyl stearate	Methyl ester stearic acid	C19H38O2
m-Xylene	m-Xylene	C8H10
Nitrous oxide	R-744A	N2O
Neon	R-720	Ne
Neopentane	Tetramethylmethane	C5H12
Nitrogen trifluoride	Trifluoroamine	F3N
Nitrogen	R-728	N2
Nonane	n-Nonane	C9H20
Novec 649, 1230	Dodecafluoro-2-methylpentan-3-one	C6F12O
Octane	n-Octane	C8H18
Orthohydrogen	R-702	H2
Oxygen	R-732	O2
o-Xylene	o-Xylene	C8H10
Parahydrogen	R-702p	H2
Pentane	R-601	C5H12
Propadiene	Allene	C3H4
Propane	R-290	C3H8
Propylene	R-1270	C3H6
Propylene oxide	Methyloxirane	C3H6O
Propyne	Methyl acetylene	C3H4
p-Xylene	p-Xylene	C8H10
R11	CFC-11	CCl3F
R1123	HFO-1123	C2HF3
R113	CFC-113	C2Cl3F3
R114	CFC-114	C2Cl2F4
R115	CFC-115	C2ClF5
R116	FC-116	C2F6
R12	CFC-12	CCl2F2
R1216	Hexafluoropropylene	C3F6
R1224yd(Z)	HCFO-1224yd(Z)	C3HClF4
R123	HCFC-123	C2HCl2F3
R1233zd(E)	HFO-1233zd(E)	C3H2ClF3
R1234yf	R-1234yf	C3F4H2
R1234ze(E)	HFO-1234ze(E)	C3F4H2
R1234ze(Z)	R-1234ze(Z)	C3F4H2

Table A.4 List of fluids in REFPROP by Lemmon et al. (2010)

Name	Synonym	Chemical Formula
R124	HCFC-124	C2HClF4
R1243zf	HFO-1243zf	C3H3F3
R125	HFC-125	C2HF5
R13	CFC-13	CClF3
R1336mzz(Z)	HFO-1336mzz(Z)	C4H2F6
R134a	HFC-134a	C2H2F4
R14	FC-14	CF4
R141b	HCFC-141b	C2H3Cl2F
R142b	HCFC-142b	C2H3ClF2
R143a	HFC-143a	C2H3F3
Dichloroethane	R-150	C2H4Cl2
R152a	HFC-152a	C2H4F2
R161	Ethyl fluoride	C2H5F
R21	HCFC-21	CHCl2F
R218	Perfluoropropane	C3F8
R22	HCFC-22	CHClF2
R227ea	HFC-227ea	C3HF7
R23	HFC-23	CHF3
R236ea	HFC-236ea	C3H2F6
R236fa	HFC-236fa	C3H2F6
R245ca	HFC-245ca	C3H3F5
R245fa	HFC-245fa	C3H3F5
R32	HFC-32	CH2F2
R365mfc	HFC-365mfc	C4H5F5
R40	Methyl chloride	CH3Cl
R41	HFC-41	CH3F
RC318	FC-C318	C4F8
RE143a	HFE-143a	C2H3F3O
RE245cb2	HFE-245cb2	C3H3F5O
RE245fa2	HFE-245fa2	C3H3F5O
RE347mcc (HFE-7000)	HFE-7000	C4H3F7O
Sulfur hexafluoride	Sulfur fluoride	SF6
Sulfur dioxide	R-764	O2S
trans-Butene	(E)-2-Butene	C4H8
Toluene	Toluene	C7H8
Vinyl chloride	R-1140	C2H3Cl
Water	R-718	H2O
Xenon	Xenon	Xe